

## 1 Induction of transposable element expression is central to innate sensing

2

3 Derek C. Rookhuizen<sup>1#</sup>, Pierre-Emmanuel Bonte<sup>1</sup>, Mengliang Ye<sup>1</sup>, Thomas Hoyler<sup>1</sup>, Matteo  
4 Gentili<sup>1</sup>, Nina Burgdorf<sup>1</sup>, Sylvère Durand<sup>2,3</sup>, Fanny Aprahamian<sup>2,3</sup>, Guido Kroemer<sup>4-6</sup>, Nicolas  
5 Manel<sup>1</sup>, Joshua J Waterfall<sup>7,8</sup>, Richard Milne<sup>9</sup>, Christel Goudot<sup>1</sup>, Greg J. Towers<sup>9</sup>, and Sebastian  
6 Amigorena<sup>1#</sup>

7

8 1 Institut Curie, PSL Research University, INSERM U932, Equipes Labellisées Ligue contre le  
9 Cancer, Paris, France, F-75005

10 2 Metabolomics and Cell Biology Platforms, Institut Gustave Roussy, Villejuif, France

11 3 Centre de Recherche des Cordeliers, Equipe labellisée par la Ligue contre le cancer, Université de  
12 Paris, Sorbonne Université, Inserm U1138, Institut Universitaire de France, Paris, France

13 4 Metabolomics and Cell Biology Platforms, Institut Gustave Roussy, Villejuif, France

14 5 Centre de Recherche des Cordeliers, Equipe labellisée par la Ligue contre le cancer, Université de  
15 Paris, Sorbonne Université, Inserm U1138, Institut Universitaire de France, Paris, France

16 6 Pôle de Biologie, Hôpital Européen Georges Pompidou, AP-HP, Paris, France

17 7 INSERM U830, Integrative Functional Genomics of Cancer Lab, PSL Research University, Institut Curie  
18 Research Center; Paris, France.

19 8 Department of Translational Research, PSL Research University, Institut Curie Research Center; Paris,  
20 France.

21 9 Division of Infection and Immunity, University College London; London, United Kingdom.

22

23

## 24 SUMMARY

25 Evidence indicates that transposable elements (TEs) stimulate innate sensing pathways in  
26 various pathologies but it is not clear whether they are sensed during normal physiological  
27 responses. Here we show that, during activation with an exogenous pathogen associated  
28 molecular pattern (PAMP), dendritic cells (DCs) epigenetically remodel heterochromatin at TEs  
29 by depleting the methyltransferase *Suv39h1* and reducing histone-3 lysine-9 trimethylation  
30 (H3K9me3). TLR4 signaling activates TE expression to enhance innate responses through the  
31 DNA sensor cGAS. Cytosolic cGAS-bound DNA comprised LINE1 TEs as the predominant  
32 endogenous ligands. Concordantly, LINE1 inhibition attenuated the type-I IFN response to LPS  
33 and rescued influenza virus infection. We propose that in healthy cells, exogenous PAMPs  
34 epigenetically activate self-derived PAMPs (LINE1) that engage cGAS to enhance responses.  
35 These data explain why pathogens employ redundant and broad innate immune  
36 countermeasures, to suppress activation of host PAMPs and illustrate a hitherto unappreciated  
37 role for host genome-derived PAMPs in response to pathogens.

38

## 39 INTRODUCTION

40 The ability to distinguish self from non-self is a central principle of immunity. Invading pathogens  
41 must be recognized as non-self to trigger an adequate response while self-antigens must be

42 tolerated to avoid autoimmunity. Innate detection of pathogens depends on the recognition of  
43 pathogen associated molecular patterns (PAMP) by pattern recognition receptors (PRR). PRRs  
44 include the Toll-like receptors (TLR) that sample extracellular and endosomal spaces for  
45 PAMPs (1) and various sensors that detect RNA and DNA (2). Upon PAMP detection, PRRs  
46 trigger signaling cascades that induce transcription factors to activate defensive gene  
47 expression. A key set of early defense genes include the type 1 interferons (IFN-I) that bind the  
48 ubiquitously expressed interferon receptor (IFNAR1/2) to activate JAK/STAT signaling and  
49 downstream transcription factors. The subsequent expression of up to 2000 interferon  
50 stimulated genes (ISGs) induces a defensive state in infected and neighboring uninfected cells  
51 through complex and incompletely understood mechanisms (3).

52  
53 Recognition of foreign nucleic acid is a key step in sensing of pathogens, particularly viruses.  
54 Host nucleic acid sensors recognise nucleic acid in a non-sequence-specific way. Chemical  
55 differences in RNA structure such as phosphorylated 5' ends, rather than the 5' cap found in  
56 mammalian mRNA, or long double-stranded (ds) RNAs, distinguish pathogen RNAs that are  
57 detected by the PRRs RIG-I or MDA5, respectively (4, 5). Upon ligand binding, RIGI and MDA5  
58 converge on the adaptor MAVS that activates TBK1 to phosphorylate IRF3 (Hornung et al.,  
59 2006; Li et al., 2009). In contrast, DNA sensing depends on DNA localization, rather than  
60 chemistry. DNA is not expected in the cytoplasm, and cytoplasmic DNA is sensed by the DNA  
61 sensor cyclic GMP-AMP synthase (cGAS) to activate IFN production (6). Upon binding to DNA,  
62 cGAS produces the cyclic dinucleotide 2'3'cGAMP (di-cyclic GMP-AMP monophosphate) that  
63 binds the adaptor protein STING and induces conformational changes leading to IRF3  
64 activation(7, 8). Therefore, both RNA and DNA sensing culminate in IRF3-driven transcription of  
65 type-I IFN.

66  
67 The fact that nucleic acid sensing is not sequence specific blurs the fundamental distinction  
68 between self and non-self. Indeed, an expanding and complex literature describes dysregulation  
69 of various types of host-derived retrotransposons leading to activation of either RNA or DNA  
70 sensors, production of type-I IFN and/or inflammation (9-13). Retrotransposons are  
71 transposable elements (TEs) that are broadly characterized by the presence (in endogenous  
72 retroviruses, ERVs) or absence (in LINE and SINE) of long terminal repeats (LTRs). TE  
73 expression can lead to the generation of dsRNA (14) and TEs encoding intact reverse  
74 transcriptase can produce dsDNA copies from their RNA genome for *de novo* integration into  
75 host genomes (14-16). Alternatively, RT-defective TEs, such as SINE and ETn, coopt the

76 reverse transcriptase of other TEs to generate dsDNA(17, 18). Therefore, expression of TEs  
77 can generate nucleic acids that act as endogenous PAMPs and possibly drive deleterious  
78 immune responses. Given this potential to cause disease, it is striking that nucleic acid sensors  
79 have not evolved to avoid undesirable triggering by TE. Rather, it is assumed that in normal  
80 tissues TEs should be transcriptionally silenced and epigenetic histone modifications, including  
81 H3K9me3, are known to repress TE expression (19).

82

83 However, comparison of TE silencing between closely related apes revealed highly evolved  
84 control mechanisms suggesting that regulation of TE expression rather than complete silencing  
85 may be important in normal physiology (20). In this paper, we hypothesize that regulated  
86 expression of TEs is, in fact, part of a normal innate immune response. We tested this  
87 hypothesis in the context of the prototypic innate immune response to Gram negative bacterial  
88 lipopolysaccharide (LPS) and the response to infection with the single-stranded negative sense  
89 RNA virus influenza A (IAV). We show that stimulation of the anti-bacterial (1) and anti-viral  
90 receptor (21) TLR4 by LPS rapidly depletes H3K9me3 at LINE1 and SINEB1 loci by reducing  
91 expression of the histone methyltransferase *Suv39h1* and concomitantly inducing TE  
92 transcription through MYD88 and TRIF signaling. We find that the consequent LINE1  
93 expression boosts the type-I IFN response to LPS in dendritic cells (DCs) by providing nucleic  
94 acid ligands for the cGAS/STING DNA sensing pathway.

95

96 Interrogation of cGAS-bound DNA in LPS stimulated cells, by immunoprecipitation and high-  
97 throughput sequencing (HTS), identified LINE1 as a principal cytosolic cGAS ligand.  
98 Furthermore, targeted genome-wide silencing of LINE1 elements using a CRISPR-dCas9-KRAB  
99 system confirmed that LINE1 act as endogenous PAMPs to activate cGAS and contribute to the  
100 consequences of LPS sensing. Crucially, single cell RNA sequencing (scRNA-seq) revealed  
101 that several distinct TLR pathways can activate the same set of TEs, suggesting a common  
102 mechanism among diverse innate stimuli. Indeed, inhibition of LINE1 expression, SUV39H1  
103 overexpression, and treatment with reverse transcriptase inhibitors all rescued IAV infection of  
104 DCs, demonstrating the impact of derepressed TE expression on the host response to a  
105 pathogen encounter.

106

107 We propose that stimulation of cGAS via expression of reverse transcribing TEs contributes to  
108 the normal physiological response to pathogen-derived PAMPs, exemplified here by LPS and  
109 IAV infection. Our work establishes a new model in which TE expression is a central

110 component of inflammatory innate immune responses. This is important because it suggests  
111 that pathogens must suppress recognition not just of their own PAMPs, but also that of TE  
112 nucleic acids derived from the host, perhaps explaining why so many pathogens encode  
113 apparently redundant innate immune countermeasures. Further, it defines a novel approach for  
114 investigation of diverse inflammatory and autoimmune pathologies and provides a new impetus  
115 for therapeutic innovation.

116

## 117 **RESULTS**

### 118 **LPS induces *Suv39h1* regulated TE expression**

119 In order to understand the role of TE expression during normal innate immune responses, we  
120 treated WT bone marrow-derived dendritic cells (BMDC) with the prototypical TLR4 ligand LPS  
121 and performed high throughput mRNA sequencing (mRNAseq). LPS triggered robust TE  
122 expression that manifested as waves of transcription—for example, cluster one at two to four  
123 hours, and cluster two at six to 18hrs (Figure 1A). TEs from the three retrotransposon  
124 superfamilies were all differentially expressed (DE) at the individual element level upon LPS  
125 treatment (Figure 1J). We hypothesized that distinct TE families might be uniquely targeted for  
126 expression by LPS stimulation. Thus, we compared the proportion of elements in different  
127 families before and after treatment using the hypergeometric test that revealed specific  
128 enrichment of LINE1 and different ERV families whereas SINE families did not significantly  
129 enrich (Figure S1A). Therefore, LPS selectively induces transcription of distinct TE families.

130

131 Transcriptional control of TEs remains incompletely understood, particularly during normal  
132 physiology. TLR4 activates the canonical transcription factors *Nfkb* (*Rela* and *Relb*) and *Irf3* via  
133 the MYD88 and TRIF signaling pathways, respectively (22-24). The simplest hypothesis for  
134 LPS-induction of TE expression is that *Nfkb* and *Irf3* directly induce TE transcription. To test  
135 this, we performed differential expression analysis of LPS-induced TE transcripts in cells  
136 deficient for either *Myd88* or *Trif* (Figure 1B) and distinguished four groups of LPS-induced TE  
137 as follows—*Myd88* (*Myd88*-dependent), *Trif* (*Trif*-dependent), *Myd88*- and *Trif*-dependent  
138 (*Myd88/Trif*-dependent), *Myd88*- and *Trif*-independent (independent) (Figure 1C, D, S1B). The  
139 *Myd88*-, *Myd88/Trif*-, and *Trif*-dependent groups contained the majority of LPS-induced, DE  
140 total LINE1 whereas the *Myd88*-, and *Myd88/Trif*-dependent groups selectively induced a  
141 majority of DE intact LINE1 (Figure 1D, see Materials and Methods for definition of intactness).  
142 Similar numbers of DE LTR elements were detected in the *Myd88*, *Myd88/Trif*, and *Trif* groups,  
143 and the *Trif* pathway selectively induced relatively more SINE elements (Figure S1B),



144 distinguishing different modes of transcriptional regulation across the three retrotransposon  
145 classes. These observations reveal a previously unappreciated role for *Myd88/Nfkb* and *Trif/Irf3*  
146 in driving TE expression in addition to gene induction.

147  
148 Our results indicate that autonomous TE expression is part of the normal transcriptional  
149 landscape downstream of classical LPS/TLR4 signaling. Concordantly, using LINE1 as an  
150 exemplar of TE, we found that RELA, RELB, and IRF3 binding motifs were enriched in the 5'  
151 promoter region of intact elements (Figure 1E). As a positive control for our observations, YY1,  
152 a known LINE1 transcription factor in human (25) and mouse (26) also mapped to the LINE1  
153 promoter region (Figure 1E). Altogether, our observations suggest that LPS directly regulates  
154 TE expression via canonical TLR4-induced transcription factors.

155  
156 Although the *Myd88*-dependent group contained the most LINE1 elements (Figure 1C, D), it  
157 contributed a relatively intermediate amount to the total DE LINE1 mRNA, assessed by  
158 distribution of total LINE1 expression from mRNA-seq data (21-31%, Figure 1F). Meanwhile, the  
159 *Myd88/Trif*-dependent group contributed the largest proportion of total DE LINE1 mRNA (55-  
160 65%), whereas elements dependent on *Trif* alone contributed the least (12-20%, Figure 1F).  
161 Therefore, co-regulation by *Myd88* and *Trif* induced greater TE RNA expression, compared to  
162 either pathway alone. We conclude that both pathways contribute to induction of TE expression  
163 downstream of LPS detection by TLR4.

164  
165 TEs are transcriptionally silenced by epigenetic modifications (19) such as H3K9me3 which is  
166 catalyzed by histone-lysine N-methyltransferases SUV39H1/2 and SETDB1, the latter  
167 cooperating with TRIM28. Previous work showed that SUV39H1 selectively trimethylated H3K9  
168 at intact LTR and LINE1 loci in a mouse embryonic fibroblast cell line (27). Two studies have  
169 subsequently shown that, in cell lines, the HUSH complex also targets evolutionarily young TEs  
170 in collaboration with SETDB1 and TRIM28 (28, 29). Intriguingly, we found that LPS stimulation  
171 of BMDC rapidly and selectively depleted *Suv39h1* and *Setdb1* mRNA (Figure 1G, S1C).  
172 *Trim28*, and HUSH complex members (*Morc2a*, *Mphosph8*) were also transiently decreased at  
173 the mRNA level. *Fam208a* (HUSH) and *Suv39h2* transcript levels were relatively stable in the  
174 early phase of the response but increased at later time points (Figure S1C). LPS treatment also  
175 induced several histone lysine demethylases belonging to the KDM family that target H3K9me3  
176 (Figure S1C). Strikingly, *Suv39h1* was also lost at the protein level on LPS stimulation of BMDC  
177 whereas *Setdb1* and *Mpp8* were not (Figure 1H), indicating that additional mechanisms such as

178 proteosomal targeting may impact *Suv39h1* expression. These results suggest that LPS  
179 stimulation rapidly remodels H3K9me3 heterochromatin with a key role for *Suv39h1*.

180

181 We therefore directly interrogated the effect of *Suv39h1* depletion on TE expression. In fact,  
182 mRNAseq revealed that knockout of *Suv39h1* in BMDCs (Figure 1G) significantly induced TE  
183 expression, even in the absence of LPS, as compared to WT cells (Figure 1I). Consistent with  
184 the notion that *Suv39h1* is a negative regulator of TE expression, LPS treatment of *Suv39h1*KO  
185 cells further enhanced expression of the same TEs induced by LPS in WT cells, with similar  
186 kinetics (Figure 1A, J). For example, LPS induced 2603 differentially expressed LINE1 elements  
187 in *Suv39h1*KO compared to 1435 elements in WT (Figure 1J). We conclude that *Suv39h1* is a  
188 critical regulator of the magnitude of TE expression downstream of LPS stimulation.

189

190 Because evolutionarily younger (intact) elements have been implicated as PAMPs in diverse  
191 settings (13, 30, 31), we focused on the direct impact of *Suv39h1* expression on these elements  
192 specifically. Analyzing only intact elements reiterated that *Suv39h1* regulated expression of  
193 LINE1, LTR and SINE (Figure 1K). Specifically, *Suv39h1* KO had the greatest effect on DE of  
194 individual TE copies belonging to young LINE1 families (L1Md\_F, L1Md\_T, L1Md), to SINEB1,  
195 and to ERV1 and ERVK (Figure S1D-F), consistent with a previous study that used a mouse  
196 embryonic cell line (27). *Suv39h1* knock-out increased the number of DE intact LINE1 by 3 fold,  
197 upon LPS stimulation, compared with WT cells, whereas expression of truncated LINE1  
198 elements was less impacted, approximately 2-fold (Figure 1K). Importantly, the expression of  
199 intact elements supports the model that the transcripts we are measuring represent autonomous  
200 TE transcription rather than transcriptional read-through of, for instance, intronic TEs or  
201 lncRNAs (32, 33).

202

203 Critically, the three groups of *Myd88/Trif*-regulated TE were represented in DE LINE1 elements  
204 in *Suv39h1*KO when compared to WT cells (Figure 1F), consistent with *Suv39h1* being a  
205 negative regulator of these elements. We hypothesize that LPS drives specific TE expression  
206 through simultaneous activation of *Myd88/Trif* to provide transcriptional activation via NF $\kappa$ B and  
207 IRF3 while concomitant loss of the negative regulator *Suv39h1* enhances TE transcriptional  
208 permissiveness. Thus, transcription factor specificity, and loss of H3K9me3 at TE loci due to  
209 SUV39H1 depletion, drive TE induction and determine the magnitude of expression.

210

211 We next used publicly available RNAseq data from ENCODE to ask whether LPS induces TE  
212 expression in human cells. Data from primary human monocyte-derived DCs demonstrated that,  
213 as for mouse BMDCs, untreated human cells expressed low levels of LINE, SINE, and LTR  
214 elements (Figure S1G, H) that were strongly increased by LPS treatment (Figure S1H). In  
215 particular, the largest effects were observed on LINE and SINE that peaked at two hours (Figure  
216 S1H). We saw that low levels of the relatively young, full length LINE1 L1PA elements and SINE  
217 transcripts were expressed at steady state but that LPS greatly boosted their transcription along  
218 with one copy of ERVK (LTR) (Figure S1I-K). Therefore, our observations of TE expression  
219 during inflammatory responses in mouse cells translate directly to humans with the difference  
220 that LTR expression may be relatively more restricted in humans.

221  
222 Based on our analysis of transcriptional control of TEs by LPS, we hypothesized that additional  
223 innate sensors would induce TEs. Using differential expression of TEs in our bulk mRNA-seq  
224 datasets, we established a TE signature score, and used it to follow TE induction in a publicly  
225 available single-cell RNA-seq data set from BMDCs (34). This analysis revealed induction of the  
226 same TEs at single cell resolution as in bulk mRNAseq data following LPS treatment (Figure  
227 1L). Stimulation of BMDCs with either a TLR2 (PAM<sub>3</sub>CSK<sub>4</sub>) or a TLR3 ligand (non-transfected  
228 dsRNA mimetic poly(I:C), PIC) that stimulate the *Myd88*- and *Trif*- pathways, respectively,  
229 induced robust TE expression (Figure 2J). Strikingly, these disparate PAMPs mimicking diverse  
230 pathogen stimuli, activated expression of the same TEs as defined by our LPS-based signature  
231 score, but with different magnitudes and kinetics of activation. Therefore, these data expand our  
232 observations with different protocols, and support our hypothesis that induction of TE  
233 expression is central to innate immune sensing. Altogether, these data suggest that  
234 physiological depletion of *Suv39h1* following LPS detection, selectively permits expression of  
235 TEs.

### 236 237 **Innate activation regulates TE heterochromatin dynamics**

238 Given that *Suv39h1* was uniquely depleted at both the mRNA and protein levels we sought to  
239 establish the overlap between enhanced TE expression and *Suv39h1*-dependent, LPS-  
240 sensitive, H3K9me3 peaks. H3K9me3 chromatin immunoprecipitation followed by high  
241 throughput sequencing (ChIP-seq) of WT and *Suv39h1*KO BMDCs allowed us to establish  
242 *Suv39h1*-dependent H3K9me3 patterns. Our analysis identified H3K9me3-bound regions, with  
243 approximately 80% overlap of H3K9me3 peaks among biological replicates of the same time  
244 point and background (Figure S2A). Consistent with the demonstrated role for *Suv39h1* in

245 establishing H3K9me3 marks on TEs (27), we observed 126,000 H3K9me3 peaks at TE loci in  
246 *Suv39h1*WT reduced to 92,000 in *Suv39h1*KO BMDCs (Figure S2B). We reasoned that by  
247 filtering the WT BMDC H3K9me3 peaks for corresponding peaks in *Suv39h1*KO BMDC, then  
248 the remaining set of H3K9me3 peaks should represent those that are specifically regulated by  
249 *Suv39h1*. This analysis identified 75,000 peaks that we termed *Suv39h1*-dependent peaks  
250 (Figure S2B). Importantly, more peaks were identified as *Suv39h1*-dependent than were  
251 apparently lost in *Suv39h1*KO cells (Figure S2B, see methods) because our analysis included  
252 some peaks which were found in proximal but distinct positions in *Suv39h1*KO cells. We  
253 attribute these peaks to compensatory methylation by *Setdb1*, which normally targets a set of  
254 TEs that is broader but overlaps with *Suv39h1* targets (19). Altogether, our analyses suggested  
255 that *Suv39h1* maintained 58% of the H3K9me3 peaks in untreated WT cells (Figure 2A, S2B).  
256 Strikingly, when compared to *Suv39h1*-independent peaks, *Suv39h1* H3K9me3 peaks were  
257 significantly enriched in LINE1 (60%), whereas LTR (26%), and SINE (7%) were relatively  
258 depleted (Figure 2A). Of note, and consistent with the impact of *Suv39h1* knockout on TE  
259 expression (Figure S1D-F), *Suv39h1*-dependent peaks at LINE1 were primarily enriched on  
260 evolutionarily younger elements (L1Md\_F, L1Md\_T, L1Md\_A) (Figure S2C). Peak inspection  
261 revealed robust and selective enrichment of H3K9me3 at the 5' end and to a much lesser extent  
262 at the 3' end of intact LINE1 elements (Figure 2B). Deletion of *Suv39h1* abolished H3K9me3 at  
263 the flanking regions as well as within the bodies of LINE1 elements (Figure 2B, S2C). Although  
264 *Suv39h1*-dependent H3K9me3 was not especially enriched on SINE elements relative to  
265 *Suv39h1*-independent peaks (Figure 2A), a subset of peaks on SINEB1 were *Suv39h1*-  
266 dependent (Figure S2D). In contrast, the impact of *Suv39h1* deletion was minimal at other TEs  
267 such as SINEB2, ERV1, ERVL, and ERVK (Figure S2F), consistent with reduced enrichment of  
268 *Suv39h1*-dependent H3K9me3 peaks at these elements (Figure 2A). Again, we hypothesize  
269 that the reduced effect of *Suv39h1*KO on H3K9me3 at these elements may reflect  
270 compensatory methylation by *Setdb1* (19, 35).

271  
272 Next, we treated WT BMDCs with LPS to compare *Suv39h1*-dependent and LPS-sensitive  
273 H3K9me3 peaks by CHIP-seq. Consistent with LPS-driven loss of *Suv39h1* expression, LPS  
274 stimulation of WT BMDCs readily extinguished H3K9me3 at specific loci, totaling 35% of  
275 *Suv39h1*-dependent H3K9me3 peaks (Figure 2D). Concordantly, these peaks were lost at  
276 LINE1 and SINEB1 (Figure 2E, S2F). Among LINE1 elements that lost *Suv39h1*-dependent  
277 H3K9me3 during LPS challenge (Figure 2E), the L1Md\_F2 subfamily was disproportionately  
278 enriched (47%) compared to other LINE1 subfamilies (Figure 2F), indicating direct impact of

279 *Suv39h1* loss on these elements during LPS treatment. In contrast, although LPS stimulated  
280 LTR element expression (Figure 1), it did not extinguish H3K9me3 peaks at ERV1 and ERVK  
281 elements as readily as at LINE1 and SINEB1 (Figure S2G), consistent with the reduced effect of  
282 *Suv39h1* knock-out on steady-state H3K9me3 at these loci (Figure S2E). We propose *Suv39h1*-  
283 independent regulation of these elements downstream of LPS. Our data support a model in  
284 which LPS-induced depletion of SUV39H1 (Figure 1G, H) facilitates heterochromatin loss to  
285 directly regulate de-repression of specific LINE1 and SINEB1 elements. This model is  
286 consistent with observations that disruption of epigenetic pathways that silence LINE1 causes  
287 their expression and activation of innate immunity (13, 30, 31). We hypothesize that specific  
288 TEs are regulated as part of normal innate immune physiology and might naturally contribute  
289 PAMPs to enhance, amplify, or broaden a physiological innate immune response.

290

### 291 **TE expression and inflammation**

292 We next sought evidence for TE contributing endogenous PAMP that might be detected and  
293 therefore contribute to LPS-driven inflammatory responses. We first examined the effect of  
294 overexpressing *Suv39h1* on LPS treatment of RAW264.7 macrophages (Figure 3A). *Suv39h1*-  
295 overexpression (SUV39H1oe) significantly dampened the LPS-mediated induction of a  
296 luciferase construct controlled by the ISG54 promoter construct measured as a surrogate for  
297 IFN-I production and ISG induction (ISG54-luciferase). LPS induction of the endogenous ISG  
298 VIPERIN was also repressed by SUV39H1oe (Figure 3B). This effect was confirmed at the level  
299 of signal transduction with reduced levels of phosphor-TBK1 and -IRF3 but unaffected levels of  
300 total TBK1/IRF3 protein (Figure 3D), consistent with *Suv39h1*oe reducing PAMP levels and thus  
301 downstream PRR signaling. Importantly, SUV39H1oe did not impact ISG54-luciferase  
302 production after stimulation with a STING ligand, 2'3'cGAMP (Figure 3C), demonstrating that  
303 cells overexpressing *Suv39h1* were capable of producing WT levels of ISG activation  
304 downstream of DNA sensing activation.

305

306 Conversely, complete ablation of *Suv39h1* had opposite effects. LPS-stimulated *Suv39h1*KO  
307 cells produced significantly higher levels of IFN-I (IFN) mRNA and protein than their WT  
308 counterparts (Figure S3A, B), exhibiting enhanced phosphor-TBK1, -p65, and IRF3 signal-  
309 transduction (Figure S3C). Concordantly, *Suv39h1*KO cells exhibited a more vigorous and  
310 sustained anti-viral response to LPS than WT cells, evidenced by the upregulation of ISGs  
311 (Figure 3E, S3D). We conclude that *Suv39h1* levels, up or down, determine the magnitude of  
312 the IFN-I/ISG response following LPS stimulation.

313

314 In parallel experiments, we found that *SUV39H1* depletion with shRNA in primary human  
315 monocyte-derived DCs also significantly enhanced LPS induced ISG SIGLEC-1 expression  
316 whereas it had less pronounced effects on expression of the NFkB-regulated activation marker  
317 CD86 (Figure S3E,F). Our data are therefore consistent with SUV39H1 regulation of LPS  
318 responses being conserved in human cells.

319

320 We hypothesized that enhanced steady-state expression of TEs in *Suv39h1*KO cells should  
321 also amplify baseline ISG expression. In fact, gene set enrichment analysis (GSEA) of RNAseq  
322 data revealed that *Suv39h1*KO BMDCs exhibited a significantly augmented type-I IFN/anti-viral  
323 gene signature at baseline compared to WT cells ( $P < 10^{-10}$ ) (Figure 3F, blue). Further, ablation  
324 of the type-I IFN receptor (*Ifnar*) in WT and *Suv39h1*KO BMDCs, abolished baseline differences  
325 in ISG expression ( $P > 0.05$ ) (Figure 3F, gold), confirming that these ISG steady-state  
326 differences resulted from enhanced type-I IFN signaling. In a second cell type, in RAW264.7  
327 macrophages, depletion of *Suv39h1* with shRNA (Figure S3G, H) also enhanced the baseline  
328 ISG expression as measured by ISG54-luciferase production (Figure S3I). These data suggest  
329 that *Suv39h1*KO is not directly impacting ISG expression because increased ISG expression  
330 levels in *Suv39h1*KO cells is IFN dependent.

331

332 To further probe whether ISG and cytokine loci are directly regulated by *Suv39h1* and  
333 H3K9me3, we analyzed H3K9me3 peaks in ISG loci and compared them directly with  
334 mRNAseq data from the same samples. H3K9me3 assessment by ChIPseq revealed that  
335 ISGs, and *Ifnb* itself, are not associated with *Suv39h1*-sensitive H3K9me3 marks (Figure S3J).  
336 Furthermore, both WT and KO cells broadly maintained H3K9me3 peaks in the same set of  
337 ISGs, and in fact, *Suv39h1*KO cells maintained slightly more peaks (Figure S3J). In addition, the  
338 presence or absence of H3K9me3 peaks did not correlate with ISG mRNA expression at  
339 baseline (Figure S3J). Therefore, direct regulation of ISGs by *Suv39h1* and H3K9me3 does not  
340 explain the enhanced ISG response in *Suv39h1*KO cells. Rather, our data suggest that  
341 *Suv39h1* loss, either downstream of LPS signaling, or due to *Suv39h1*KO, drives TE expression  
342 which activates innate immune sensing and IFN production.

343

#### 344 **cGAS is required for *Suv39h1*-mediated effects on IFN-I**

345 We hypothesized that LPS-induced TE expression is detected by innate sensors thereby  
346 contributing endogenous PAMP to LPS responses. Nucleic acid sensors are thought to detect



347 TE-derived PAMPs when TE are expressed in various experimental systems: knock out of  
348 epigenetic regulators (13), models of senescence/aging (30, 31), cancer (9, 36). Furthermore, in  
349 the autoinflammatory condition, Aicardes Goutierres syndrome (AGS), individuals defective for  
350 the nuclease TREX1, which ordinarily degrades cytoplasmic DNA, experience cGAS-dependent  
351 (37) IFN-I-driven, inflammation resulting from either chromatin leakage into the cytosol or from  
352 TE-derived DNA (38, 39) with the contribution of each still debated. It is unclear whether TEs  
353 contribute PAMP to natural, physiological innate immune sensing.

354

355 We therefore explored the contribution of *Suv39h1*-regulated TE expression to LPS responses.  
356 We first assessed activation of the DNA-sensing cGAS pathway by measuring STING  
357 phosphorylation (Konno et al., 2013) in LPS activated WT BMDCs by immunoblot. In this  
358 experiment, we increased the number of cells loaded into gel wells ( $8.5 \times 10^5$ ) and transfected a  
359 low dose of 2'3'cGAMP to allow comparison of phosphor-STING as a control. Strikingly, LPS  
360 induced STING phosphorylation and this was lost in *Cgas*<sup>-/-</sup> cells, consistent with endogenous  
361 PAMP detection by cGAS (Figure 4A). LPS-activation of IRF3 detected by WB was only  
362 modestly reduced by cGAS knock out, consistent with cGAS-independent LPS-induced  
363 canonical TRIF and MYD88 activation of IRF3 (Figure 4A). IRF3 activation by phosphorylation is  
364 a complex process, and one possibility is that cGAS impacts IRF3 phosphorylation at sites that  
365 are important for activation but that are not detected here (Robitaille et al., 2016). As expected,  
366 transfection of BMDCs with 2'3'cGAMP (250-500ng/ml) induced STING and IRF3  
367 phosphorylation independently of cGAS (Figure 4A). Concordantly, LPS stimulation of *Cgas*<sup>-/-</sup>  
368 BMDCs induced significantly less IFNB (type I IFN) protein as compared to WT cells (Figure  
369 S4A). As a control, *Cgas* ablation blocked HT-DNA-induced IFNB whereas 2'3'cGAMP  
370 transfection induced similar IFNB levels in both WT and *Cgas*<sup>-/-</sup> cells as expected since  
371 2'3'cGAMP activates STING directly (Figure S4B). Similar results were obtained using freshly  
372 isolated splenic DCs where LPS treatment of *Cgas*<sup>-/-</sup> cells also triggered reduced expression of  
373 the ISGs VIPERIN and CCL5 relative to WT cells (Figure S4B). Again, transfected 2'3'cGAMP  
374 induced normal ISG responses in both WT and *Cgas*<sup>-/-</sup> cells as expected. Importantly, surface  
375 expression of CD86, a NFkB-regulated gene, was not impacted by *Cgas*KO (Figure S4B). These  
376 data indicate a contribution of cGAS/STING DNA sensing in LPS-induced activation of the IFN-  
377 I/anti-viral pathway.

378

379 Interpretation of these experiments with *Cgas*<sup>-/-</sup> cells is somewhat complicated by previous  
380 observations of reduced baseline expression of ISGs in *Cgas*<sup>-/-</sup> cells (40). We reasoned that

381 cGAS may constantly detect host/TE DNA, leading to low levels of IFN production, which prime  
382 innate immune responses in general, and that this effect is lost in *Cgas* knockouts. If this is the  
383 case, then ablation of tonic IFN-I signaling by *Ifnar* KO should eliminate the cGAS contribution  
384 to LPS responses. To investigate this possibility, we generated *Ifnar*<sup>-/-</sup> and *Cgas*<sup>-/-</sup>*Ifnar*<sup>-/-</sup>  
385 RAW264.7 macrophages with CRISPR-Cas9. Critically, LPS induction of IFNB was significantly  
386 compromised in *Cgas*<sup>-/-</sup>*Ifnar*<sup>-/-</sup> cells, as compared to *Ifnar*<sup>-/-</sup> cells (Figure S4G),  
387 demonstrating cGAS dependence in *Ifnar*<sup>-/-</sup> cells. We therefore conclude that the reduction of  
388 LPS-induced IFN-I production by *Cgas*<sup>-/-</sup> cells did not depend on the steady-state differences  
389 in baseline IFN signaling in *Cgas*<sup>-/-</sup> cells because we identified dependence on cGAS in *Ifnar*<sup>-/-</sup>  
390 <sup>-/-</sup> cells. As controls, both WT and *Cgas*<sup>-/-</sup> RAW264.7 macrophages responded similarly to  
391 stimulation with IFNB by producing comparable levels of ISG54-luciferase (Figure S4H),  
392 demonstrating intact *Ifnar/Stat1* signaling that was effectively abrogated upon *Ifnar* deletion  
393 (Figure S4H). Further, LPS stimulation of *Ifnar*<sup>-/-</sup> RAW264.7 macrophages induced IFNB  
394 production (Figure S4G) but did not induce the ISG, VIPERIN (Figure S4I), as expected. We  
395 conclude that cGAS dependence of LPS-induced type-I IFN production is not due to reduced  
396 tonic IFN signaling in *Cgas*<sup>-/-</sup> cells.

397

398 To further probe the role of the cGAS pathway during LPS responses, we used a small  
399 molecule STING inhibitor (STINGi, H151) (41). Acute inhibition of STING permits assessment  
400 of the role of the cGAS/STING pathway in the absence of baseline effects. Strikingly, STING  
401 blockade significantly attenuated LPS-induced expression of specific ISGs (Figure 4B). As  
402 controls, *Myd88*KO in BMDCs dampened LPS-induced ISG responses while *Trif* ablation  
403 completely abolished them (Figure 4B), and H151 prevented activation of ISG expression after  
404 transfection with the cGAS ligand HT-DNA (Figure 4B), as expected. Similarly, LPS induction of  
405 the ISG, MDA5, measured by western blot was strongly reduced in *Cgas*<sup>-/-</sup> cells (Figure 4A).  
406 Unexpectedly, *Mavs* deletion had no effect on ISG induction by LPS (Figure 4B) whereas the  
407 responses to transfected PIC, or influenza A virus/Puerto Rico 8/1934/H1N1 (IAV/PR8)  
408 infection, were attenuated (Figure S4C,D). These results suggest that *Mavs*-dependent sensing  
409 of TE-derived RNA does not contribute to LPS responses.

410

411 We next sought to confirm these observations in RAW264.7 macrophages using CRISPR-Cas9  
412 genetic ablation of *Mavs*, in WT or *Cgas*<sup>-/-</sup> cells (Figure S4E). LPS induction of ISG54-  
413 luciferase expression was dependent on *Myd88*, *Trif*, and *Cgas* because individual knock outs  
414 showed significant impairment of IFN-I activation, recapitulating our results in BMDCs (Figure

415 4C,D). Once again, inhibition of RNA sensing by deletion of *Mavs* in a WT or *Cgas*<sup>-/-</sup>  
416 background, did not affect the LPS-induced ISG response (Figure 4D). As a control, ablation of  
417 *Cgas* and *Mavs* effectively blocked induction of IFN-I following transfection with HT-DNA or PIC  
418 (polyI:C), respectively (Figure S4F). Collectively, these data verify that cGAS-dependent  
419 sensing contributes to LPS responses, but that MAVS-dependent RNA sensing does not.

420

421 Our data suggest a mechanism in which *Trif* and *Myd88*-dependent genes, LPS induces *Trif*  
422 and/or *Myd88*-dependent TE expression (Figure 1B-D, S1B, D-F) that can be detected by  
423 cGAS. Importantly, while deletion of *Trif* or *Myd88* significantly blocked TE induction, inhibition  
424 of STING with H151 left TE induction intact (Figure 4E). Thus TE induction is downstream of  
425 LPS, and cGAS/STING activation is downstream of TE expression. Together, these data are  
426 consistent with a model in which the defect in LPS-triggered ISG responses in *Cgas*<sup>-/-</sup> cells  
427 stems from an inability to sense TE-derived DNA. Based on this model, we hypothesized that  
428 the enhancement of IFN production by *Suv39h1* depletion required *Cgas*. Indeed, *Cgas* deletion  
429 in RAW264.7 macrophages blocked enhancement of LPS-induced IFN-I production by *Suv39h1*  
430 shRNA (Figure 4G). Notably, enhancement of the LPS-induced IFN-I response in *Suv39h1*-  
431 depleted cells was independent of *lfnar*, confirming our observations in BMDCs, and dependent  
432 on *Cgas* (Figure S4I). Therefore, depletion of *Suv39h1* augments LPS-induced IFN in a *Cgas*-  
433 dependent manner and is independent of tonic IFN signaling.

434

435 Consistent with *Suv39h1*-knockdown experiments, SUV39H1oe did not suppress LPS-induced  
436 IFN-I when *Cgas* was ablated (Figure 4F, compare to Figure 3B, note the difference in scale).  
437 Importantly, SUV39H1oe did not impact cGAS protein levels (Figure 3D) ruling out a direct  
438 effect on cGAS expression. Furthermore, SUV39H1oe did not restrict induction of IFN when  
439 cGAS was bypassed by direct activation of STING with its ligand, 2'3'cGAMP (Figure 3C),  
440 consistent with a role for *Suv39h1* in suppressing expression of endogenous cGAS ligands.  
441 Thus, *Cgas* is required for *Suv39h1* regulation of the type-I IFN response to LPS. These data  
442 are consistent with a model in which cGAS detects *Myd88/Trif*-driven TE expression following  
443 the physiological depletion of *Suv39h1* by LPS detection.

444

#### 445 **cGAS binds LINE1 elements in LPS stimulated cells**

446 The impact of *Cgas/Sting* blockade on the LPS-dependent IFN-I response suggested that LPS  
447 induces expression of TE that are reverse transcribed into DNA and detected by cGAS. We  
448 therefore sought evidence for LPS-induced cytosolic DNA. We isolated cytosolic fractions by

449 digitonin extraction (42) and retained nuclei for standardized quantification. Real time-qPCR  
450 analysis of RNase-treated cytosolic fractions from BMDCs revealed that LPS significantly  
451 boosted cytoplasmic levels of LINE1 and ERVK DNA (Figure 5A). Furthermore, pretreatment  
452 with a reverse transcriptase inhibitor cocktail (emtricitabine, tenofovir, and nevirapine) effectively  
453 ablated the increased cytosolic DNA levels (Figure 5A) and restricted expression of the ISG  
454 VIPERIN (Figure S5A). Therefore, reverse-transcribed TE DNA is induced by LPS, and reverse  
455 transcriptase inhibition reduces LPS-induced ISG expression.

456  
457 We next sought to understand the nature of the DNA activating cGAS during an LPS response  
458 using cross-linked immunoprecipitation of a tagged endogenous cGAS allele (eGFP-cGAS)  
459 from BMDCs (Gentili et al., 2019), followed by high through-put sequencing (HTS). We first  
460 biochemically fractionated BMDCs and confirmed efficient separation of the cytosol and nucleus  
461 by western blot and qPCR (Figure S5B,C). Western blots revealed cytosolic as well and nuclear  
462 cGAS protein (Figure S5B), as previously observed (43-45). Nuclear cGAS is not expected to  
463 sense chromatin (45-50), but it may sense de novo nuclear TE DNA, for instance. We therefore  
464 isolated endogenous cGAS-bound DNA from the cytosolic and nuclear compartments  
465 separately, after LPS stimulation, and subjected them to HTS. Because cGAS produces  
466 2'3'cGAMP when bound to dsDNA, single-stranded DNA and RNA-DNA hybrids (51-54) we  
467 used an approach that would preserve all DNA species in the sequencing libraries (see  
468 materials and methods) to capture a global view of cGAS-bound nucleic acid. To avoid aberrant  
469 post-lysis binding between DNA and cGAS (55), we cross-linked the cells before lysis, ensuring  
470 exclusive detection of cytosolic DNA species bound to cGAS *in vivo*. Furthermore, after pull-  
471 down, the immunoprecipitates were stringently washed with detergent and high salt buffer,  
472 precluding a significant contribution for residual post-lysis binding events; cGAS-DNA  
473 interactions are expected to occur with weak affinity ( $K_d=10\mu\text{M}$ ) (56, 57).

474  
475 Inspection of all possible DNA species in the cGAS-bound fraction revealed striking differences  
476 relative to the cytosolic input (Figure 5B). Most notably, LINE1 DNA was profoundly enriched  
477 on cytosolic cGAS compared to input (5.1-fold, 40% versus 8%) (Figure 5B, C) whereas LTR  
478 families accumulated at much lower densities (Figure 5B, C). Conversely, cytosolic cGAS was  
479 depleted of satellite, SINE, and simple repeat DNA relative to input (Figure 5B,C). A similar  
480 trend was observed for the nuclear pool of cGAS although it did not approach the same  
481 magnitude of fold enrichment or statistical significance (Figure 5B,C). For example, LINE1  
482 enriched weakly (1.68-fold, 30% versus 18%) on nuclear cGAS (Figure 5B), agreeing with a

483 recent report (Gentili et al., 2019). Importantly, Figure 5C illustrates that significant enrichment  
484 of LINE1 on cytosolic cGAS cannot be explained by genomic frequency of LINE1 copies  
485 because the enrichment of LINE1 in the cytosolic input fraction (8%) is significantly below the  
486 expected genomic frequency (18%), and this is further supported by the statistical test used to  
487 compare cGAS-IP versus input (hypergeometric test) that takes into account genomic  
488 frequency.

489  
490 To broaden our observations to a different cell type, we transduced RAW264.7 macrophages  
491 with lentivirus carrying eGFP-tagged cGAS and performed cross-linked IP from the cytosol  
492 followed by qPCR after LPS treatment (Figure S5D). Again, IP of cGAS from these cells  
493 revealed clear enrichment of LINE1 compared with non-TE DNA (Figure S5D) after LPS  
494 treatment. Although mitochondrial DNA has previously been shown to stimulate the  
495 cGAS/STING pathway (58), we did not detect appreciably enriched mitochondrial DNA on cGAS  
496 in either LPS treated BMDCs or RAW264.7 macrophages (Figure S5D,E), suggesting that  
497 mitochondria are not an important source of DNA PAMP downstream of LPS detection  
498 (mitochondria are not expected to be damaged by LPS exposure). We conclude that LINE1 is  
499 the primary endogenous ligand of cytosolic cGAS downstream of LPS stimulation. This is  
500 consistent with LPS-induced epigenetic derepression of LINE1 following depletion of the LPS-  
501 sensitive H3K9 methyltransferase, *Suv39h1*.

502  
503 To better understand the contribution of the different cGAS fractions to the LPS response, we  
504 compared fold changes in binding densities of TE subfamilies for LPS-treated versus untreated  
505 cells in each fraction. The largest changes corresponded to strong increases in LINE1 and LTR  
506 binding densities on cGAS whereas we detected only modest changes associated with nuclear  
507 cGAS binding (Figure S5F), consistent with overall enrichment (Figure 5B, C). Enumeration of  
508 unique TE copies contributing to the largest fold-changes in the different fractions identified the  
509 LINE1 subfamilies L1Md\_F2 and L1\_Mus3 as the most highly enriched (Figure 5D), reflecting  
510 the specific regulation of these elements by *Suv39h1* (Figure 2F, S2E). Of note, these elements  
511 were among the youngest (Figure 5D, least diverged) and most highly expressed LINE1  
512 elements in terms of mRNA (Figure S1C, Figure 5D), linking their availability for cGAS binding  
513 to transcriptional activation by LPS.

514  
515 To confirm whether cGAS-dependent LPS-induced IFN-I requires direct cGAS-DNA binding and  
516 enzymatic activity, we reconstituted *Cgas*<sup>-/-</sup> RAW macrophages with WT cGAS (cGAS-FL), a



517 cGAS DNA-binding mutant that lacks the DNA-binding N-terminal 160aa and harbors mutations  
518 in its zinc-thumb domain that prevent bound DNA from activating cGAS enzymatically (cGAS-  
519 DBM) (59), or a catalytically-dead cGAS mutant (cGAS-CD, E225A/D227A) that cannot produce  
520 2'3'cGAMP (Kranzusch et al., 2013). Reconstitution levels of the WT and cGAS-mutants are  
521 shown in Figure S5G. Because cGAS-FL elevated IFN-I in untreated cells (Figure S5H), we  
522 subtracted baseline values from stimulation induced IFN-I following treatment with HT-DNA,  
523 2'3'cGAMP, or LPS (Figure S5I). Critically, LPS-induced ISG54-luciferase expression was  
524 selectively restored by cGAS-FL, but not by either cGAS mutant (Figure S5I). Accordingly, HT-  
525 DNA transfection selectively activated cGAS signaling when cGAS-FL but not when cGAS-DBM  
526 or cGAS-CD were used (Figure S5I). In contrast, 2'3'cGAMP stimulated ISG54-luciferase in all  
527 settings, confirming that downstream signaling functioned normally (Figure S5I). These data  
528 reveal: 1) a specific requirement for cGAS during LPS stimulation and 2) that DNA-induced  
529 cGAS enzymatic activity is necessary for cGAS enhancement of LPS-triggered ISG responses.

530

531 Because *Suv39h1* regulates the magnitude and kinetics of LINE1 expression during LPS  
532 challenge, we predicted that *Suv39h1* deletion would enhance LINE1 DNA binding by cGAS.  
533 Indeed, LINE1 was detectable on cGAS at low levels in untreated WT cells, but LPS treatment  
534 significantly increased LINE1 density (Figure 5E). Furthermore, in *Suv39h1*KO BMDCs, steady-  
535 state LINE1 densities reached magnitudes similar to that found on cGAS in LPS-treated WT  
536 cells. As expected these were further enriched upon LPS stimulation (Figure 5E). In contrast, as  
537 a control, SINE DNA revealed disparate trends with no statistically supported differences  
538 (Figure 5F). As a control for our HTS data, cGAS-IP, followed by qPCR, detected LPS-induced  
539 enrichment of LINE1 and LTR (ERV) DNA on cytosolic cGAS whereas genic DNA such as  
540 *Gapdh* was not detected (Figure 5G). Comparison of the densities of DNA elements bound to  
541 cGAS exhibited significant and selective enrichment of LINE1 in *Suv39h1*KO relative to WT  
542 cells (Figure S5J,K). Examination of LINE1 elements precipitating with cGAS revealed that  
543 *Suv39h1* KO boosted the same LINE1 subfamilies that bound cGAS with high frequency in WT  
544 cells after LPS stimulation (Figure 5F, S5L). Thus, *Suv39h1*-regulated LINE1 elements bind  
545 cGAS following LPS detection.

546

#### 547 **LINE1 elements act as endogenous PAMPs**

548 To provide further validation for our model, we sought evidence for the role of LINE1s as  
549 endogenous PAMPs that induce IFN-I by targeting them for epigenetic repression using a  
550 CRISPR dCas9-KRAB fusion construct. In this system, the mutant Cas9 (dCas9) binds DNA but



551 is incapable of generating dsDNA breaks that would likely occur in excess when targeting  
552 numerous LINE1 elements and cause cell death (60, 61). The fused KRAB domain recruits  
553 epigenetic factors such as SETDB1, a H3K9me3 methyltransferase, driving  
554 heterochromatinization and subsequent transcriptional silencing of the target region (61). As a  
555 positive control, we targeted the 5' untranslated region of *Itgax*, the gene encoding the highly  
556 expressed integrin and myeloid marker, CD11b. Using two different guide RNAs (gRNAs), we  
557 succeeded in selectively repressing CD11b while maintaining MHC-II expression (Figure S5M).

558  
559 We next designed gRNAs to target 20,000-110,000 LINE1 elements belonging to the L1Md  
560 family, and specifically enriched either at the L1Md\_F2 sub-family (gRNA\_1 and gRNA\_2) that  
561 bound at high levels to cGAS after LPS treatment or, as a negative control, at L1Md\_A elements  
562 (gRNA\_3) which bound at low levels to cGAS (Figure S5N). Consistent with the notion that  
563 elements that bind cGAS at higher levels should contribute the largest impact to cGAS-  
564 dependent IFN-I production, gRNA\_1 and gRNA\_2 significantly impeded IFN-I production;  
565 gRNA\_3, however, had no effect (Figure 5H). Importantly, differential analysis of mRNA-seq  
566 data (Ctrl versus gRNA-expressing RAW cells) confirmed specific repression of L1Md  
567 expression by gRNA\_1 and gRNA\_2 (Figure 5I, J). Of note, the efficiency of LINE1 suppression  
568 by gRNA\_1 was similar in both LPS-treated and untreated cells (Figure 5J, dark green bars)  
569 whereas gRNA\_2 suppressed LINE1 in untreated cells but lost efficiency upon LPS exposure  
570 (Figure 5J, light green bars). The effects on LINE1 suppression were mirrored in the IFN-I anti-  
571 viral response as revealed by GSEA of anti-viral gene expression (Figure 5K); whereas gRNA\_1  
572 effectively attenuated anti-viral gene expression in both untreated and LPS treated cells,  
573 gRNA\_2 selectively suppressed steady state expression, suggesting that its repressive effect  
574 was limited to baseline TE expression and overcome by a strong LPS-induced transcriptional  
575 stimulus. These effects cannot be explained by direct suppression of anti-viral genes because  
576 neither gRNA\_1 nor gRNA\_2 target sequences were appreciably enriched in the proximity of  
577 ISG loci (Figure S5O). Therefore, LINE1 expression is required for optimal induction of IFN-I by  
578 LPS.

579  
580 Critically, in *Cgas*<sup>-/-</sup> macrophages, the suppressive effect of gRNA\_1 and gRNA\_2 on IFN-I  
581 production was lost (Figure S5P), similar to *Suv39h1oe* in *Cgas*<sup>-/-</sup> cells (Figure 4F). We  
582 conclude that LPS-induced LINE1 expression acts through cGAS to augment the IFN-I/anti-viral  
583 response. This observation is consistent with L1Md elements acting as LPS-induced  
584 endogenous cGAS ligands that amplify the type-I IFN response.

585

## 586 **Transposable element expression restricts RNA virus infection**

587 Our data support a model where innate immune responses proceed through two phases: 1)  
588 initial detection of pathogen-derived PAMP drives expression of cytokines, IFN-I, and TE  
589 through classical innate signaling pathways and 2) once TE expression reaches a critical  
590 threshold, cell autonomous detection of TE expression by cGAS/STING, and possibly other  
591 sensors, amplifies the anti-microbial response (Figure 6A). Whereas bacteria encode both RNA  
592 and DNA ligands, viral genomes typically encode one or the other, providing a useful tool to  
593 physiologically test our model. For example, various RNA viruses, including influenza, activate  
594 TLR4 (21), and although they do not contain DNA, they can, unexpectedly, activate and/or  
595 express inhibitors for the cGAS/STING pathway (62, 63). IAV infection has previously been  
596 shown to induce LINE1 expression (64, 65). We therefore tested the effect of manipulating the  
597 mechanism of innate immune amplification, that we have described, on IAV infection.

598

599 Strikingly, infection of WT BMDCs with IAV/PR8 selectively triggered depletion of SUV39H1  
600 protein and induced expression of LINE1 ORF1p but did not appreciably affect SETDB1 or  
601 MPP8 levels at the time point queried (7 hrs post infection) (Figure6B). IAV infection can be  
602 assessed by cell survival and measurement of viral nucleoprotein (NP) (Figure S6). We  
603 therefore tested the physiological outcome of IAV/PR8-induced SUV39H1 depletion by  
604 measuring the impact of SUV39H1 overexpression on IAV/PR8 infection. Indeed, SUV39H1  
605 overexpression rescued IAV infection, leading to reduced cell survival and higher levels of NP  
606 expression (Figure 6C), and consistent with the effect of SUV39H1 overexpression on cGAS-  
607 dependent LPS-induced IFN-I (Figure 3B, 4G). Next, we tested whether LINE1 suppression  
608 would rescue viral infection, hypothesizing that the depletion of SUV39H1 upon IAV/PR8  
609 infection would promote innate detection of LINE1 PAMP, similar to LPS stimulation. Strikingly,  
610 suppression of LINE1 expression with dCas9-KRAB (Figure 6D) also rescued IAV/PR8  
611 infection. We conclude that blockade of host LINE1 expression during viral infection reduced the  
612 murine innate immune response against IAV, leading to enhanced infection. Consistent with our  
613 model, we detected cGAS-dependent induction of phosphor-STING and the ISG MDA5 by IAV  
614 infection in DCs (Figure 6E). Furthermore, small molecule blockade of STING significantly  
615 increased IAV NP expression, consistent with STING signaling inhibiting RNA virus infection in  
616 these cells (Figure 6F). Concordantly, addition of a reverse transcriptase inhibitor cocktail,  
617 known to be active against TE including LINE1 (Banuelos-Sanchez et al., 2019), rescued IAV  
618 replication and enhanced virus-induced cell death (Figure 6G). Thus, consistent with our model,

619 overexpression of SUV39H1, suppression of LINE1 expression, inhibition of STING, and  
620 inhibition of reverse transcription, all rescued IAV infection in DC through suppression of innate  
621 responses. These observations support our model that innate activation induces TE expression  
622 and reverse transcription-catalyzed TE DNA that is detected by cGAS to broaden and  
623 strengthen host defenses.

624

## 625 **DISCUSSION**

626 In this study, we introduce a new paradigm for the mechanism of innate immune sensing in  
627 which endogenous PAMPs are produced within cells exposed to exogenous pathogen-derived  
628 PAMP. We propose that these endogenous PAMPs are detected by classical innate sensing  
629 pathways, amplifying and broadening responses to pathogens. Specifically, we discovered that  
630 LPS induces LINE1 expression, which is detected by cGAS to contribute to LPS-elicited IFN-I  
631 responses. We find that LPS activates LINE1 expression by driving SUV39H1 depletion that  
632 leads to loss of H3K9me3 at TE loci, combined with MYD88/TRIF-driven transcriptional  
633 activation. This discovery is important because it reveals an entirely new level of regulation of  
634 innate immune responses and ensuing inflammation that may explain inconsistencies in the  
635 field.

636

### 637 **Epigenetic regulation of TE in innate immune responses**

638 The notion that TE should be permanently switched off derives from the observation that TE  
639 expression is typically associated with pathology, particularly autoinflammation and oncogenesis  
640 (66-68). We propose that our observation of regulated TE expression, and sensing by cGAS  
641 after LPS exposure, evidences an essential role for TE expression in normal innate immune  
642 responses. This is supported by our observation that disparate PAMPs also activate TE  
643 expression (Figure 1L).

644 Indeed, we hypothesize that diverse innate detection pathways converge on distinct epigenetic  
645 regulators to induce TE PAMPs that enhance innate immunity such as type-I IFN anti-viral  
646 responses.

647

648 Previous studies of TE regulation have suggested that expression of the youngest LINE1 is  
649 epigenetically regulated by an evolutionary Red Queen style arms race akin to that between  
650 host and pathogen (20). We hypothesize that such studies, characterizing the evolution of  
651 LINE1 regulation, demonstrate how host genomes have evolved to specifically regulate their  
652 expression when required. Strikingly, our data highlight the importance of LINE1 regulation in

653 enhancing innate immunity and provide a direct example of the evolutionary benefits of retaining  
654 the capacity to regulate TE expression, rather than simply suppress it. Epigenetic marks such as  
655 H3K9me3 and DNA methylation switch gene expression on and off, and we propose that TE are  
656 simply another example of sequences that are epigenetically regulated in normal physiology,  
657 rather than comprising a distinct class of elements that must be permanently silenced (19, 69).

658

### 659 **DNA sensing of TE in innate immune responses**

660 Our results highlight a central role for the DNA sensor cGAS in the LPS driven innate immune  
661 response. Interrogation of cGAS-bound DNA in LPS stimulated cells identified LINE1 DNA as a  
662 principal cytosolic cGAS ligand and our data demonstrating that reverse transcriptase inhibitors  
663 blocked LPS-induced cytosolic DNA, and that TE mRNA correlated with cGAS-bound DNA  
664 (Figure 5D), strongly implicate reverse transcription as a key step in PAMP generation. This was  
665 previously suggested in the AGS model, *Trex1*<sup>-/-</sup> mice (70). Indeed, RTI have been used  
666 successfully to treat AGS patients (71), reducing IFN $\alpha$  protein levels and ISG expression. In  
667 addition, in another study RTI treatment depleted LINE1 cDNA and senescence-associated  
668 inflammation (30, 31). Importantly, baseline expression of LINE1 RT, which promiscuously  
669 reverse transcribes host RNA, may generally prime innate immune sensing and IFN-I responses  
670 (72-76).

671

672 Our analyses indicated that the major changes in cGAS-bound DNA species during LPS  
673 stimulation occurred in the cytosol. The relative contribution of the nuclear and cytosolic cGAS  
674 pools to IFN-I production is not clear although it is clear that the nucleus potently restricts cGAS  
675 activation due to high affinity interactions with histones H2A and H2B (45-50, 77). Although  
676 nuclear cGAS is not expected to sense chromatin, it could conceivably sense nuclear de novo  
677 LINE1 DNA, per se. Indeed, LPS induced modest changes in binding between nuclear cGAS  
678 and TEs, but the majority of cGAS-TE interaction occurred in the cytoplasm. Moreover,  
679 condensation of cytosolic cGAS on DNA creates lipid droplets that can co-sediment with nuclei  
680 (Barnett et al., 2019; Du and Chen, 2018), suggesting that our observations of changes in the  
681 binding of nuclear cGAS with TEs are overestimated by cytoplasmic contamination.

682

683 Previous studies have demonstrated the activation of cGAS by mitochondrial DNA (mtDNA)  
684 (58). We ruled out a role for mtDNA, as it did not appreciably enrich on cGAS in either of the two  
685 cell systems interrogated here, BMDCs and RAW264.7 macrophages (Figure S5D, E). Thus,

686 mtDNA binding to cGAS may be restricted by context such as certain types of viral infection (78)  
687 and pathogenic mutations in humans that permit leakage of mtDNA into the cytosol (58).

688

689 We were surprised to find in our experiments that RNA sensing of TE did not play a significant  
690 role in LPS responses because endogenous RNA PAMPs are expected to be produced more  
691 readily than DNA PAMPs which require reverse transcription from an RNA template.

692 Furthermore, RNA encoded by a ribosomal pseudogene has been implicated as an endogenous  
693 PAMP during infection, leading to a more potent anti-viral response against a variety of viruses  
694 including DNA viruses HSV-1 and EBV, and RNA virus IAV (79). It will be interesting to further  
695 investigate the impact of LPS on RNA sensing.

696

### 697 **Infection**

698 We hypothesize that induction of endogenous PAMP after detection of exogenous PAMP is a  
699 powerful mechanism to broaden and amplify defensive responses. Indeed, a recent study  
700 showed that in a human lung epithelial cell line, IAV infection triggered sumoylation-dependent  
701 degradation of TRIM28, TE induction, and ultimately led to MAVS-dependent, STING-  
702 *independent*, sensing of, presumably, de-repressed ERV RNA (64). Furthermore, another  
703 publication suggested that a host commensal skin bacteria could induce ERV elements via  
704 activation of TLR2, and this triggered innate immune responses via cGAS/STING in  
705 keratinocytes that promoted adaptive T cell responses (80). Importantly, these responses were  
706 inhibited by reverse transcriptase inhibitors, indicating that reverse transcribed ERV cDNA was  
707 detected by cGAS and concurring with our data describing cGAS-mediated detection of reverse-  
708 transcribed LINE1 elements downstream of TLR4 signaling. These observations support our  
709 model that TE expression is an integral component of innate sensing that amplifies the primary  
710 innate response through subsequent cell-autonomous sensing events (Figure 6E).

711

712 Our model is entirely consistent with observations of viruses evolving antagonists for sensing  
713 pathways that they are not expected to activate. For instance, RNA viruses block DNA sensing  
714 pathways (81). Furthermore, RNA viruses such as SARS-CoV2 (62), measles, and Nipah virus  
715 (82) also trigger cGAS/STING sensing, and SARS-CoV2 at least has been demonstrated to  
716 induce LINE1 expression (65, 83). Concordantly, RNA viruses influenza (84), SARS-CoV (85,  
717 86), SARS-CoV2 (87), Porcine epidemic diarrhea virus (88), Dengue virus (89), Yellow fever  
718 virus (90), Zika virus (91), and Hepatitis C virus (92) all inhibit the cGAS/STING DNA sensing  
719 pathway. Our model provides an explanation if detection of virus infection induces endogenous

720 PAMP production. Consistent with this, we show that STING inhibition, reverse transcriptase  
721 inhibitors, LINE1 silencing, or overexpression of SUV39H1, all rescue IAV infection of mouse  
722 DC.

723

## 724 **Cancer**

725 We propose that our model is applicable beyond infection. Natural TE expression correlates  
726 with better anti-tumor T cell responses (93) and the notion that enhanced TE expression drives  
727 an inflammatory response that is correlated with better clinical outcome, particularly after  
728 immunotherapy, is supported by studies that enhanced TE expression and the ensuing  
729 inflammatory responses either by small molecule inhibitors of DNA methylation or genetic  
730 ablation of epigenetic regulators(9, 94-96). Likewise, disruption of histone methylation by  
731 ablation of *SETDB1* led to TE dsRNA sensing and IFN-I responses in different cell lines  
732 including acute myeloid leukemia (10) and non-small-cell lung cancer(11). In addition, *Setdb1*  
733 deletion in a mouse tumor model led to enhanced T cell responses through presentation of TE-  
734 derived peptides rather than innate immune sensing (97). We speculate that a lack of innate  
735 recognition of TEs in this study may be linked to defective innate sensing pathways frequently  
736 encountered in cancer cells (Konno et al., 2018; Sutter et al., 2021). Based on our model, we  
737 hypothesize that high levels of TE expression and ensuing inflammation in tumors represents a  
738 natural innate immune defense against transformation. Concordantly, tumor cell intrinsic  
739 suppression of DNA sensing, for example via STING mutation, or suppression of TE induction  
740 by *Setdb1*, is common (97-99).

741

## 742 **Inflammation and Aging**

743 The capacity of TEs to elicit innate immunity has also been linked with diseases other than  
744 cancer, particularly inflammatory disease. Patients with Aicardies Goutiere Syndrome (AGS)  
745 suffer an interferonopathy from early development which has been associated with TE  
746 expression, reverse transcription, and activation of cGAS (37, 39, 71). LINE1 DNA has also  
747 been revealed as a source of STING-dependent neuroinflammation in a *TREX1*-mutant model  
748 of AGS (12). To date, no associations have been made between the H3K9me3 pathway and  
749 AGS, although a recent paper linked diminished SUV39H1 expression with inflammation in the  
750 lungs of patients with chronic obstructive pulmonary disease (COPD) (100). Our data are  
751 consistent with these observations and may provide mechanistic explanation. TE expression  
752 has even been suggested as a driver of aging-associated inflammation (30, 31). Collectively,  
753 this body of literature provides numerous examples of TE-derived nucleic acids acting as



754 endogenous PAMPs to activate innate sensors. However, the interpretation in each case has  
755 been that disease is enhanced or caused by the failure to keep TE expression switched off.

756

757 We propose, based on our observations, that the expression of TE to drive innate sensing is a  
758 natural physiological response to detection of pathogen and/or danger signals. Thus, disease  
759 stems from inappropriate regulation rather than simply failure to keep TE expression  
760 suppressed. For example, in cancer, we hypothesize that TE expression and activation of innate  
761 immunity is a response to transformation, evolved to activate adaptive immunity against  
762 transformed cells. We expect that the response of a cell, or cancer, to PAMP will vary  
763 depending on the active sensing pathways in each case. For example, many cell lines and  
764 cancers are defective for sensing (98, 99), and therefore, whether an RNA or DNA detection  
765 response dominates will depend on individual circumstances.

766

767 Boosting of an incipient innate immune response by autologous sensing of TE-derived PAMP is  
768 pivotal to our new model. To emphasize this and distinguish their role from that of conventional  
769 exogenous PAMP, we propose calling TE that are sensed during innate responses to infection  
770 TRansposable element Molecular Patterns (TRAMPs). In the two-phase mechanism (Figure  
771 6H) that our data suggest, the initiating response, arising from direct recognition of exogenous  
772 PAMPs expressed by the infecting organism, activates expression of cytokines, ISGs, and,  
773 importantly, TRAMPs. In the amplifying phase, cell autonomous recognition of upregulated  
774 TRAMPs, by additional sensors including cGAS, amplifies the innate response. This model  
775 might explain how extremely low levels of exogenous viral PAMP such as in the case of natural  
776 HIV infection, for instance, can lead to a measurable inflammatory response. We imagine a  
777 threshold at which TRAMPs become dominant. This threshold can be shifted in disease states.  
778 For example, in AGS, the threshold is shifted to the left by, for example, defects that lead to  
779 increases in TRAMP levels (*TREX1*, *SAMHD1*). By contrast, in certain cancers, defects in  
780 nucleic acid sensing (cGAS, STING) shift the threshold to the right. Defects of epigenetic  
781 regulators could shift the threshold in either direction.

782

783 TE are not genetic junk left over from genome evolution. Rather, they are essential for the  
784 regulation of normal physiology. We anticipate that investigation of mutations and mechanisms  
785 regulating TRAMP expression will provide mechanistic insight into diverse drivers of  
786 inflammation in a wide range of conditions, including aging, cancer, and infection. This work

787 could provide diagnostic tools and suggest novel therapeutic targets to transform our  
788 management of human disease.

789

## 790 **FIGURE LEGENDS**

791 **Figure 1** *Suv39h1* expression determines the magnitude of TE transcription during LPS  
792 challenge, see also Figure S1. (A) Heatmap showing Pearson Correlation-based hierarchical  
793 clustering of the most highly expressed TEs by normalized expression (FPKM) in WT (n=3) and  
794 *Suv39h1*KO (n=4) BMDCs. Relative values are represented by z-score. (B) Volcano plot  
795 exhibiting differentially expressed (DE) LINE1 elements in 2hr LPS-treated *Myd88*<sup>-/-</sup> (left) or  
796 *Trif*<sup>-/-</sup> (right) BMDCs compared with WT control cells. n=3 per genotype (*Myd88*<sup>+/+</sup>, *Trif*<sup>+/+</sup>,  
797 *Myd88*<sup>-/-</sup>, *Trif*<sup>-/-</sup>) per time point. Red dots signify significantly expressed elements, adjusted *P*  
798 value < 0.05. (C, D) Bar graphs representing the number of total (C) or intact (D) LINE1  
799 elements dependent on the indicated signaling pathway for significant expression as determined  
800 by differential analysis of mRNAseq data such as that presented in panel B. (E) Density plots of  
801 IRF3, RELA, RELB, and YY1 transcription factor motif sequence (JASPAR database)  
802 enrichment along the sequence of full-length LINE1 elements. (F) Stacked bar plots showing the  
803 percentage of total DE LINE1 mRNA FPKM in *Suv39h1*WT and KO BMDCs at steady state and  
804 during LPS treatment that derives from each transcriptionally-defined group in panels C and D.  
805 (G) mRNA sequencing data showing that histone methyltransferase *Suv39h1* transcript levels  
806 are quickly depleted during LPS challenge in BMDCs. WT (n=3), KO (n=4). (H) Western blot of  
807 SETDB1, MPP8, SUV39H1, and Histone H3 in whole cell extracts from WT c57BL/6 BMDCs left  
808 untreated or stimulated with LPS for the indicated times. (I) Volcano plots displaying DE LINE1,  
809 LTR, and SINE element mRNA from sequencing data, comparing *Suv39h1*WT and *Suv39h1*KO  
810 BMDCs at steady- state. WT, n=3; KO, n=4. (J) Volcano plots displaying DE LINE1, LTR, and  
811 SINE element mRNA from sequencing data, comparing untreated (UT) to 2hr LPS-treated  
812 within WT or *Suv39h1*KO BMDCs. WT, n=3; KO, n=4. (K) Quantification of differentially  
813 expressed *intact* (top) or degenerate (bottom) TE classes in 2hr LPS-treated versus untreated  
814 within WT or *Suv39h1*KO BMDCs. (L) A TE signature score based on DE LINE1, LTR, and  
815 SINE in bulk mRNAseq data of WT BMDCs was projected onto a previously published  
816 scRNAseq dataset (Shalek et al., 2015) to compare TE expression induction by LPS,  
817 Pam<sub>3</sub>CSK<sub>4</sub> (PAM), or poly(I:C) (PIC) treatment at the indicated time intervals. Significance cutoff  
818 for differential analyses in B-D and I-L was defined as an adjusted *P* value less < 0.05 and a  
819 log<sub>2</sub> fold change ≥ 2. In C and D, the number of elements per group represents the sum of all  
820 significantly expressed LINE1 elements at 0, 1, 2, and 4hrs of LPS treatment when comparing

821 WT to KO cells (*Myd88*<sup>+/+</sup> vs *Myd88*<sup>-/-</sup>, *Trif*<sup>+/+</sup> vs *Trif*<sup>-/-</sup>). In G, statistical significance was  
822 determined by one-way ANOVA and Bonferonni ad-hoc analysis comparing untreated to LPS-  
823 treated WT BMDCs. \**P*<0.05, \*\* *P*<0.001, \*\*\**P*<0.001, \*\*\*\**P*<0.0001.

824

825 **Figure 2** LPS induces rapid depletion of H3K9me3 at transposable elements in dendritic cells,  
826 see also Figure S2. (A) Left, stacked bar chart summarizing proportion of *Suv39h1*-dependent  
827 (red) and -independent (white) H3K9me3 peaks in unstimulated WT BMDCs from H3K9me3  
828 ChIP-seq data. Right, pie chart exhibiting percent enrichment (% indicated by emboldened  
829 numbers) of specific DNA species in *Suv39h1*-dependent (middle) and -independent (right)  
830 H3K9me3 peaks. Below, heatmap summarizing statistically significant enrichment of DNA  
831 elements in *Suv39h1*-dependent versus *Suv39h1*-independent H3K9me3 peaks. (B) H3K9me3  
832 ChIP-seq reads aligned by the 5' end of intact *Suv39h1*-dependent LINE1 elements in WT and  
833 *Suv39h1*KO cells at steady state. Summary data are depicted as histograms at the top of the  
834 read alignment. (C) Pie chart showing percent enrichment of LINE1 subfamilies marked by  
835 *Suv39h1*-dependent H3K9me3 peaks displayed in B. Percent enrichment is indicated by  
836 emboldened numbers as in panel A. (D) Bar chart showing the percentage of total *Suv39h1*-  
837 dependent H3K9me3 peaks lost during LPS challenge. (E) Aligned *Suv39h1*-dependent LINE1  
838 H3K9me3 peaks in untreated, two, and four hours LPS treated WT BMDCs. (F) Pie chart  
839 showing percent enrichment of LINE1 subfamilies in the LPS-sensitive H3K9me3 peaks on  
840 LINE1 in panel E. Percent enrichment is indicated by emboldened numbers as in panel A. (A-F)  
841 WT n=3, KO n=3 mice per experimental condition. In panels B and E, the x-axis coordinates  
842 refer to kilobases. Statistical significance in panel A was determined by a two-proportions z-test  
843 for comparison of proportions in two independent samples. Standard statistical analysis were  
844 used for peak calling of ChIPseq data (see materials and methods for detailed protocol).

845

846 **Figure 3** LPS-elicited physiological depletion of SUV39H1 promotes a type-I IFN response in  
847 myeloid cells independently of direct regulation of ISG loci, see also Figure S3. (A) Western blot  
848 of SUV39H1 in RAW264.7 macrophages transduced with empty lentivector or with a SUV39H1  
849 overexpression (OE) lentiviral vector. (B) Left, RAW264.7 macrophages transduced with  
850 lentivirus control (n=5, closed circles) or SUV39H1 overexpressing lentivirus (n=5, open circles)  
851 were stimulated for 8 hours with the indicated concentrations of LPS and the IFN-I response  
852 measured was measured by ISG54-driven luciferase assay. Right, flow cytometric analysis of  
853 intracellular expression of the ISG, VIPERIN, by APC-control and SUV39H1 overexpressing  
854 RAW264.7 macrophages stimulated as in left panel. (C) Left, RAW264.7 macrophages

855 transduced with lentivirus as in B and stimulated with the STING ligand 2'3'cGAMP for 8hrs and  
856 the IFN-I response measured by ISG54-driven luciferase assay as in B. Right, flow cytometric  
857 analysis of ISG, VIPERIN, expression in untreated and 2'3'cGAMP transfected cells after 8hrs.  
858 (D) Western blot analysis of innate signal transduction pathways elicited in control and  
859 SUV39H1 overexpressing RAW264.7 macrophages by LPS stimulation for the indicated times.  
860 (E) Volcano plot depicting differential gene expression in WT versus *Suv39h1*KO BMDCs at  
861 two hours of LPS stimulation. anti-viral genes with an adjusted *P* value <0.05 and FC ≥ 2 are  
862 indicated in red. (F) Gene set enrichment analysis (GSEA) comparing expression of anti-viral  
863 genes from mRNAseq data between the following groups: untreated *Suv39h1*KO x *Ifnar*<sup>+/+</sup> (n=4)  
864 versus *Suv39h1*WT x *Ifnar*<sup>+/+</sup> (n=3) BMDCs (Blue); untreated *Ifnar*<sup>-/-</sup> *Suv39h1*KO (n=3) versus  
865 *Ifnar*<sup>-/-</sup> x *Suv39h1*WT BMDCs (n=3) (gold). (D) Western blots of the indicated total proteins  
866 and phosphor-proteins during LPS treatment of BMDCs with the following genotypes from left to  
867 right: *Ifnar*<sup>+/+</sup> x *Suv39h1*WT, *Ifnar*<sup>+/+</sup> x *Suv39h1*KO, *Ifnar*<sup>-/-</sup> x *Suv39h1*WT and *Ifnar*<sup>-/-</sup> x  
868 *Suv39h1*KO. Western blots represent one of three experiments where similar results were  
869 obtained. In B and C, statistical significance was determined by two-way ANOVA and  
870 Bonferonni ad-hoc analysis: \**P*<0.05, \*\* *P* <0.001, \*\*\**P*<0.001, \*\*\*\**P*<0.0001. In (E), significance  
871 cutoff for differential gene expression analysis was defined as an adjusted *P*-value < 0.05 and a  
872 fold change ≥ 2. WT, n=3 mice per group; KO, n=4. In (F), statistical significance was GSEA;  
873 *Suv39h1*WT x *Ifnar*<sup>+/+</sup> (n=3), *Suv39h1*KO x *Ifnar*<sup>+/+</sup> (n=4), *Suv39h1*WT x *Ifnar*<sup>-/-</sup> (n=3), and  
874 *Suv39h1*KO x *Ifnar*<sup>-/-</sup> (n=3).

875  
876 **Figure 4** LPS elicits cGAS-dependent but not MAVS-dependent ISG expression, see also  
877 Figure S4. (A) Western blots of the indicated proteins and phosphor-proteins in WT and *Cgas*<sup>-/-</sup>  
878 <sup>-/-</sup>BMDCs treated as follows: LPS treatment was for 4 hours; cGAMP (250-500ng/ml), 2 hours.  
879 (B) The indicated ISGs indicated in bold italics on the left were measured by mRNAseq of  
880 steady-state and LPS-stimulated (4hrs, 100ng/ml) WT, *Myd88*<sup>-/-</sup>, *Trif*<sup>-/-</sup> BMDCs or by RT-  
881 qPCR of WT and *Mavs*<sup>-/-</sup> BMDCs treated with STING inhibitor (STINGi, H-151) or vehicle  
882 control (DMSO) at steady state or stimulated with the indicated LPS dose (33 or 100ng/ml). As a  
883 positive control for inhibition of the cGAS/STING pathway, WT BMDCs were treated with  
884 STINGi or DMSO and then transfected with 1µg/ml HT-DNA for 5 hours. ISG expression was  
885 calculated relative b-Actin by the delta Ct method. (C) Scatter plot of ISG54-Luciferase assay of  
886 conditioned supernatants from WT, *Myd88*<sup>-/-</sup>, or *Trif*<sup>-/-</sup> RAW264.7 macrophages stimulated  
887 with the indicated concentration of LPS. (D) Scatter plot of ISG54-Luciferase assay of

888 conditioned supernatants from WT, *Cgas*<sup>-/-</sup>, *Mavs*<sup>-/-</sup>, and *Cgas*<sup>-/-</sup> x *Mavs*<sup>-/-</sup> RAW264.7  
889 macrophages that were stimulated with the indicated concentration of LPS. (E) The indicated  
890 LINE1 families indicated in bold on the left were measured by mRNAseq of steady-state and  
891 LPS-stimulated (4hrs, 100ng/ml) WT, *Myd88*<sup>-/-</sup>, *Trif*<sup>-/-</sup> BMDCs or by RT-qPCR of WT and  
892 *Mavs*<sup>-/-</sup> BMDCs treated with STING inhibitor (STINGi, H-151) or vehicle control (DMSO) at  
893 steady state or stimulated with the indicated LPS (100ng/ml) for 4hrs. As a positive control for  
894 inhibition of the cGAS/STING pathway. (F) ISG54-driven luciferase assay as in C and D. WT  
895 and *Cgas*<sup>-/-</sup> RAW264.7 macrophages in which *Suv39h1* was left intact (shCtrl) or depleted  
896 (*shSuv39h1*) with lentiviral-derived shRNA were treated with the indicated concentrations of  
897 LPS for 8. WT (*shCtrl*, n=8; *shSuv39h1*, n=8), *Cgas*<sup>-/-</sup> (*shCtrl*, n=8; *shSuv39h1*, n=8). (G)  
898 ISG54-driven luciferase assay as in C,D, and F. *Cgas*<sup>+/+</sup> or *Cgas*<sup>-/-</sup> RAW cells that were  
899 transduced with APC control or SUV39H1 overexpression lentivectors and stimulated with the  
900 indicated concentrations of LPS for 8hrs (n=10 per group). B-G, Statistical significance was  
901 determined by two-way ANOVA with Bonferonni's ad hoc analysis for individual  
902 comparisons: \**P*<0.05, \*\* *P* <0.001, \*\*\**P*<0.001, \*\*\*\**P*<0.0001.

903

904

905 **Figure 5** LINE1 is an endogenous cGAS PAMP, see also Figure S5. (A) qPCR of digitonin-  
906 extracted, RNase-treated cytosolic extracts from untreated or LPS stimulated (100ng/ml, 4hrs)  
907 WT BMDCs that were pretreated with an RTI cocktail or DMSO vehicle control. (B) High-  
908 throughput sequencing of DNA extracted from the following fractions from LPS-treated BMDCs  
909 expressing *Cgas*<sup>gfp/gfp</sup>: cytosolic input fraction, cytosolic cGAS, nuclear input fraction, and  
910 nuclear cGAS. The pie charts display the enrichment in each fraction visualized as the  
911 distribution of the sum of the read densities (FPKM≥1) per unique element belonging to the  
912 indicated DNA species. N=2 for each sample. (C) Hypergeometric statistical comparison of read  
913 density proportions in panel B between input and the respective cGAS-IP within each cellular  
914 fraction (indicated in bold on right). Red color denotes  $-\log_{10}$  (*P* value); grey, no statistical  
915 difference. (D) Correlation between the number of individual LINE1 elements within each  
916 subfamily expressed as mRNA and detected in the top 10% of fold changes in cytosolic cGAS-  
917 bound DNA. Dot size indicates the DNA density (FPKM) of cGAS-bound LINE1 families and the  
918 color scale indicates the average sequence divergence from consensus of the elements  
919 detected on cGAS. Less divergence indicates evolutionarily younger elements. (E) Scattered



920 dot plots exhibiting FPKM of cGAS-bound unique LINE1 element DNA (FPKM  $\geq 1$  and FC  $\geq 2$   
921 over input) in untreated and treated *Suv39h1WTxCgas<sup>egfp/egfp</sup>* and *Suv39h1KOxCgas<sup>egfp/egfp</sup>*  
922 BMDCs. Red bars represent median values; box ends represent quartiles. Statistical analysis  
923 was performed with one-way ANOVA followed by Bonferroni's ad hoc analysis for individual  
924 comparison between samples. (F) Scattered dot plots as in E except FPKM values represent  
925 density of unique SINE element DNA bound to cGAS. Statistical analysis was performed as in  
926 E. (G) qPCR of LINE1, ERVK, and genomic *Gapdh* DNA bound to cytosolic cGAS  
927 immunoprecipitated with anti-GFP magnetic beads from BMDC cytosolic fractions as in B and E  
928 (filled green bars). Controls include control-bead IP from *Cgas<sup>egfp/egfp</sup>* (hashed green bars), GFP-  
929 bead (filled grey bars) and control-bead IP (hashed grey bars) from *Cgas<sup>+/+</sup>* BMDCs.  
930 (H) ISG54-Luciferase assay of resting and LPS-stimulated (8hrs) WT RAW264.7 cells  
931 expressing mutant d(dead)Cas9 KRAB fusion protein and control or LINE1-targeted gRNAs.  
932 (I) Representative volcano plot comparing differentially expressed (DE) LINE1 elements in  
933 gRNA\_1 versus Ctrl cells stimulated with LPS. (I) Bar chart representing the log<sub>2</sub> fold-change  
934 between DE LINE1 elements (Adjusted *P* value  $<0.05$ ) in Ctrl ("Down in gRNA") and gRNA-  
935 expressing cells ("Up in gRNA") at steady state or after LPS treatment. (K) Above, GSEA of the  
936 effect of the specified gRNA versus control on anti-viral gene expression in resting and LPS-  
937 stimulated cells. Line color indicates the specific comparison. Below, gene rank plots. Each bar  
938 represents an anti-viral gene and its position along the x-axis indicates relative enrichment in  
939 the indicated group: left indicates enrichment in control cells; right, LINE1-targeted gRNA  
940 expressing cells. bar color corresponds to the same color used to specify the specific  
941 comparison above. *P* value to the right indicates statistical significance of enrichment of anti-  
942 viral gene expression in the control group versus LINE1-targeted gRNA-expressing cells. NES,  
943 normalized enrichment score. A, E, F, and H, statistical significance was determined by 2-way  
944 ANOVA, and Bonferonni's ad hoc analysis was used for individual comparisons. A, E, F, H:  
945 \**P* $<0.05$ , \*\* *P* $<0.001$ , \*\*\**P* $<0.001$ , \*\*\*\**P* $<0.0001$ .

946

947 **Figure 6** Induction of TE expression enhances host fitness during RNA virus infection. (A)  
948 Schematic illustrating the induction of endogenous PAMPs upon detection of microbial PAMPs.  
949 Microbial infection triggers IFN-I, cytokines and TEs. Subsequent detection of TE PAMP  
950 amplifies the innate immune response. (B) Western blots of the indicated proteins in in mock-  
951 treated or IAV/PR8-infected (7hrs) WT BMDCs. (C) Western blots of the indicated proteins and  
952 phosphor-proteins in mock-treated or IAV/PR8-infected (7hrs) WT and *Cgas<sup>-/-</sup>* BMDCs. (D)  
953 Quantification of IAV/PR8 NP expression in DCs 5 dpi in the presence of DMSO vehicle or



954 STING inhibitor (STINGi, H-151). (E) DCs treated with DMSO vehicle or a RTI cocktail were  
955 infected with the indicated dilution of IAV/PR8 and NP expression(left) and percentage survival  
956 (right) were quantified by flow cytometry at 5dpi. (F) DC expressing lentivector control (APC) or  
957 overexpressing SUV39H1(oe) were infected with IAV/PR8 as in E and %survival and NP  
958 expression quantified 5dpi as in E. (G) DC expressing mutant d(dead)Cas9 KRAB fusion protein  
959 and control or LINE1-targeted gRNA\_1 as described in figure 5 were infected with IAV/PR8 at  
960 the indicated dilution and NP expression(left) and percentage survival (right) quantified by flow  
961 cytometry. (H) Schematic displaying a revised mechanism for innate sensing of pathogen or  
962 that proceeds through two phases, in which TE expression is a central component. Initial  
963 detection of a pathogen occurs through classical sensing pathways that stimulate expression of  
964 defensive immune genes as well as TEs. Over time, TRAMP expression is amplified and may  
965 constitute the majority of detected PAMP in the latter phase. A critical threshold for TE detection  
966 may be surpassed once TRAMP concentration overcomes restriction factors such as the  
967 cytosolic DNase *Trex1*, for example. Grey arrow heads indicate increased or decreased  
968 expression; black arrows, impact on critical threshold; question marks indicate that the given  
969 condition is likely to impact the critical threshold but has not been directly tested. D-G, statistical  
970 significance was determined by 2-way ANOVA and Bonferonni's ad hoc analysis for individual  
971 comparisons: \* $P < 0.05$ , \*\*  $P < 0.001$ , \*\*\* $P < 0.001$ , \*\*\*\* $P < 0.0001$ .

972  
973 **Figure S1** Ablation of *Suv39h1* significantly enhances LPS-induced intact TE transcription,  
974 reflecting loss of H3K9me3 during LPS challenge, related to Figure 2. (A) Bubble plot exhibiting  
975 percentage enrichment and statistical comparison of the proportion of differentially expressed  
976 TE in LPS treated versus untreated BMDCs in WT or *Suv39h1*KO cells. Statistical significance  
977 ( $P < 0.05$ ) was determined by a two-proportions z-test.  $-\log_{10}(P \text{ value})$  is indicated by color  
978 scale, bubble size indicates percentage of TE enrichment within each comparison. (B) mRNA  
979 sequencing data showing expression levels (FPKM) of H3K9me3 methyltransferases or  
980 pathway members (top, red lines) during LPS treatment: HUSH complex (*Fam208a*,  
981 *Mphosph8*, *Morc2a*) and other H3K9me3 remodelers/heterochromatin factors *Setdb1*, *Trim28*,  
982 *Suv39h2*, and *Hp1a* (*Cbx5*). (Bottom, blue lines) mRNA sequencing data showing modulation of  
983 of histone lysine demethylases expression (FPKM): *Kdm1a/b*, *Kdm2a/b*, *Kdm4a/b*, and *Kdm5c*.  
984 (C-E) Summarized data of total numbers of intact LINE1 (C), SINE (D) and LTR (E) that were  
985 differentially induced in either *Suv39h1*WT or KO BMDCs when LPS treated samples were  
986 compared with steady state. (F) Mean average plot of human LINE, SINE, and LTR elements  
987 comparing 4hr LPS treated to untreated monocyte-derived DCs from human PBMCs. Blue dots,

988 TEs with a  $\log_2FC$  2, and average FPKM1; Red dots, full length LINE1 transcripts with a  $\log_2FC$   
989 2, and average FPKM1. (G) Enumeration of total TE numbers filtered by our criteria in panel e  
990 from each indicated class at the different time points of LPS stimulation compared to untreated  
991 cells. (H, I) Applying the same filters as in panel F, only the full length TE copies from each  
992 indicated class are displayed for LINE1 and LTR (H) and SINE (I). I, Pie charts exhibiting the  
993 relative proportions of expressed full length LINE1 copies enriched in untreated (UT, top) or  
994 LPS-treated (4hrs, bottom) cells.

995

996

997 **Figure S2** *Suv39h1*-dependent H3K9me3 peaks are primarily localized at transposable  
998 elements, related to Figure 1. (A) Percentage among three biological replicates of H3K9me3  
999 peaks with significant overlap. (B) The number of H3K9me3 peaks in UT *Suv39h1WT* and  
1000 *Suv39h1KO* BMDCs and the total number of *Suv39h1*-dependent peaks that were determined  
1001 by subtraction of *Suv39h1KO* H3K9me3 peaks from WT H3K9me3 peaks. (C) Correlation  
1002 between divergence of LINE1 versus the number of elements copies containing a *Suv39h1*-  
1003 dependent H3K9me3 peak. (D) H3K9me3 peaks at SINEB1 elements in *Suv39h1WT* and  
1004 *Suv39h1KO* BMDCs aligned at 5' end with summary data at top as in Figure 2B, E. (E)  
1005 Summary of H3K9me3 reads in the indicated elements that were aligned at their 5' ends as in  
1006 Figure 2B, E (top). (F) Aligned SINEB1 peaks as in D, in WT BMDCs stimulated with LPS for  
1007 the indicated duration. (G) Summary data of aligned ERV1 (top) and ERVK (bottom) H3K9me3  
1008 peaks in WT cells stimulated with LPS for the indicated times. D-G, the x-axis coordinates refer  
1009 to kilobases. Statistical peak calling was performed as detailed in the methods section.

1010

1011 **Figure S3** Loss of *Suv39h1* amplifies the LPS-induced anti-viral response independently of  
1012 direct regulation of gene loci, related to Figure 3. (A) *Ifnb1* expression from mRNAseq data of  
1013 *Suv39h1WT* and KO BMDCs that were treated with LPS for the indicated times. Data are  
1014 displayed as FPKM. (B) ELISA quantification of Type-I IFN (IFNb) protein levels in conditioned  
1015 supernatants from *Suv39h1WT* (n=4) or *Suv39h1KO* (n=5) BMDCs treated with LPS for the  
1016 indicated times. (C) Western blots of the indicated proteins and phosphor-proteins in  
1017 *Suv39h1WT* and KO BMDCs that were treated with LPS (100ng/ml) for the specified durations.  
1018 (D) Heatmap displaying semi-supervised clustering (Pearson correlation) of anti-viral (ISG) and  
1019 inflammatory gene expression in WT and *Suv39h1KO* BMDCs stimulated with LPS for the  
1020 indicated times. Data are from the same mRNA-seq data set used for TE analysis in Fig. 1. (E)  
1021 Flow cytometric data quantifying SIGLEC1 (ISG) and CD86 (NFkB-regulated) surface

1022 expression on mDCs transduced with nontargeting or one of three different SUV39H1-targeting  
1023 lentiviral shRNA constructs (n=4 patient samples per condition). (F) Western blot of SUV39H1,  
1024 demonstrating targeted depletion by three different lentiviral shRNAs in freshly cultivated human  
1025 monocyte-derived DCs (mDCs). (G) qPCR data exhibiting the time course of *Suv39h1* mRNA  
1026 expression during LPS treatment in RAW macrophages transduced with the designated  
1027 lentiviral shRNAs (n=2). (H) Western blot of SUV39H1, SETDB1, and gp96 (loading control) to  
1028 assess shRNA-mediated knockdown in untreated RAW264.7 macrophages transduced with the  
1029 indicated lentiviral shRNA particle. (I) ISG54-Luciferase assay data comparing luciferase  
1030 concentration in conditioned supernatants of untreated RAW264.7 in which *Suv39h1* was  
1031 depleted by lentiviral encoded shRNA (*shSuv39h1*, n=4) or not (shGFP, n=4). (J) Left, heatmap  
1032 showing z-scores of ISG mRNA expression (FPKM) in untreated *Suv39h1*WT (n=3) or  
1033 *Suv39h1*KO (n=4) BMDCs, and right, the corresponding H3K9me3 peak status from H3K9me3  
1034 ChIPseq data (WT, n=3; KO, n=3): red, H3K9me3 peak positive, grey, no H3K9me3 peak  
1035 detected. Several genes along with *Irfn1* are designated in bold to the right as exemplars of  
1036 ISGs with a grey or red box indicating H3K9me3 peak status. Statistical differences in panels A,  
1037 B, and E were determined by two-way ANOVA, followed by Bonferroni's ad hoc analysis for  
1038 individual comparison between groups: \* $P < 0.05$ , \*\*  $P < 0.001$ , \*\*\* $P < 0.001$ , \*\*\*\* $P < 0.0001$ . In I, a  
1039 two-tailed student's t-test was performed to determine statistical significance ( $P < 0.05$ ).

1040  
1041

1042 **Figure S4** The cGAS pathway of DNA sensing, but not the RNA-sensing MAVS pathway is  
1043 required for an optimal IFN- $\beta$ /anti-viral response following stimulation with LPS, related to Figure  
1044 4. (A) ELISA quantification of IFN $\beta$  protein concentration in conditioned supernatants from  
1045 *Cgas*<sup>+/+</sup> (n=3) and *Cgas*<sup>-/-</sup> (n=3) BMDCs stimulated with LPS or with transfected HT-DNA,  
1046 2'3'cGAMP. (B) Compiled flow cytometric data showing the percentage of Viperin<sup>+</sup> or CCL5<sup>+</sup>  
1047 CD11c<sup>+</sup>CD11b<sup>+</sup>MHC-II<sup>+</sup> splenic *Cgas*<sup>+/+</sup> (n=3) and *Cgas*<sup>-/-</sup> (n=3) DCs stimulated *ex vivo* with  
1048 10-fold dilutions of LPS (top, 100ng/ml highest concentration) or bottom, with 2'3'cGAMP. (C)  
1049 Western blot of the indicated total and phosphor-proteins following stimulation of WT and  
1050 *Mavs*<sup>-/-</sup> BMDCs with transfected poly(I:C) (5hrs) or infection with IAV/PR8 (7hrs). (D) RT-qPCR  
1051 data of the ISGs, 5hrs after transfection of poly(I:C) in WT and *Mavs*<sup>-/-</sup> BMDCs. ISG expression  
1052 was calculated relative to b-Actin by the delta Ct method. (E) Western blot displaying protein  
1053 expression of MAVS, cGAS, and gp96 after CRISPR-Cas9-targeted deletion of *Mavs* in WT and  
1054 *Cgas*<sup>-/-</sup> RAW264.7 macrophages. (F) Functional validation of CRISPR-Cas9-targeted *Mavs*  
1055 deletion in RAW264.7 macrophages displayed in E; top, transfection of poly(I:C), 2 $\mu$ g/ml;

1056 bottom, transfection of HT-DNA, 1µg/ml. (G) ELISA quantification of IFNB concentration in  
1057 conditioned supernatants of untreated or LPS (100ng/ml) treated RAW264.7 macrophages that  
1058 were deleted for *Ifnar1/2* by CRISPR-Cas9 and the transduced with control lentiviral particles  
1059 (shGFP) or shRNA lentiviral particles targeting *Suv39h1* (*shSuv39h1*). (H, I) Functional  
1060 validation of CRISPR-Cas9 targeted deletion of *Ifnar* in RAW264.7 macrophages. (C) ISG54-  
1061 driven luciferase assay measuring responsiveness of *Ifnar*<sup>+/+</sup>*Cgas*<sup>+/+</sup>, *Ifnar*<sup>+/+</sup>*Cgas*<sup>-/-</sup>, *Ifnar*<sup>-/-</sup>  
1062 *Cgas*<sup>+/+</sup>, and *Ifnar*<sup>-/-</sup>*Cgas*<sup>-/-</sup> cells to overnight stimulation with titrated recombinant IFNB  
1063 protein. Error bars represent standard deviation and bar graphs represent the mean. Statistical  
1064 significance was determined with two-way ANOVA and Bonferonni's ad hoc analysis for  
1065 individual comparisons. A, B, D, and G, statistical significance was determined with two-way  
1066 ANOVA and Bonferonni's ad hoc analysis for individual comparisons.

1067  
1068 **Figure S5** Immunoprecipitation of endogenous cGAS from nuclear and cytosolic extracts  
1069 followed by NGS reveals significant changes in cytosolic cGAS-DNA binding activity, related to  
1070 Figure 5. (A) Flow cytometric quantification of expression of the ISG VIPERIN in untreated or  
1071 8hr LPS-stimulated WT BMDCS that were pretreated with DMSO vehicle or an RTI cocktail. (B)  
1072 Western blot revealing WT cGAS and the eGFP knock-in cGAS (KI) allele from whole cell lysate  
1073 (WCE), cytosolic (C) and nuclear (N) fractions, as well as immunoprecipitation of cross-linked  
1074 cytosolic and nuclear cGAS species. RAB6 and H3 serve as cytosolic and nuclear loading  
1075 controls, respectively. Arrowheads indicate lanes displaying immunoprecipitated eGFP-cGAS.  
1076 (C) qPCR of the indicated amplicons in digitonin-extracted RNase-treated cytosolic DNA and  
1077 pellet fractions from untreated BMDCs. (D) qPCR of indicated DNA species that bound to an  
1078 overexpressed eGFP-tagged cGAS contstruct in WT (shControl, n=4) and *Suv39h1* (n=4)  
1079 knockdown RAW cells following LPS stimulation. (E) Pie chart depicting the relative proportions  
1080 of raw reads in the indicated DNA species from NGS of cytosolic cGAS-IP. (F) Left, comparison  
1081 of the fold changes in LPS versus untreated BMDCs of TE binding density on endogenous  
1082 cGAS in cytosolic and nuclear fractions. Right, variance describing the fold changes in the  
1083 binding density of the indicated TE class enriched on nuclear and cytosolic cGAS following LPS  
1084 treatment (n=2 per condition). An F-test was used for statistical comparison of variances. (G)  
1085 Flow cytometric plots displaying lentiviral-based expression levels of the indicated GFP-cGAS or  
1086 SFFV-BFP control constructs used for experiments in Figure S5H, I. (H) ISG54-driven luciferase  
1087 assay quantification of baseline IFN-I production by *Cgas*<sup>-/-</sup> RAW cells following lentiviral  
1088 reconstitution with different cGAS constructs—full-length WT (cGAS-FL, n=12), catalytically-  
1089 dead (cGAS CD, n=7), DNA binding mutant (cGAS-DBM, n=7), SFFV (empty vector control). (I)

1090 ISG54-driven luciferase assay quantification of IFN-I production by *Cgas*<sup>-/-</sup> RAW cells following  
1091 lentiviral reconstitution with different cGAS constructs—full-length WT (cGAS-FL, n=12),  
1092 catalytically-dead (cGAS-CD, n=7), DNA binding mutant (cGAS-DBM, n=7), SFFV (empty  
1093 vector control)—and titrated stimulation with HT-DNA, 2'3'cGAMP, or LPS. Baseline values  
1094 were subtracted from treated values to compare the response between groups reconstituted  
1095 with distinct cGAS constructs. (J) Distribution of the cytosolic cGAS-IP read density sums  
1096 (FPKM $\geq$ 1) among all classes of DNA species in *Suv39h1KO* BMDCs. (K) Hypergeometric  
1097 statistical comparison of the *Suv39h1KO* BMDC cytosolic cGAS-IP read density sums in panel  
1098 E with WT cytosolic cGAS IP (Figure 5B). (L) Violin plot exhibiting the difference in the number  
1099 of cytosolic cGAS-bound LINE1 elements by family between *Suv39h1KO* and *Suv39h1WT*  
1100 BMDCs. (M) Inhibition of cell surface myeloid marker CD11b on RAW264.7 using the dCas9-  
1101 KRAB transcriptional inhibitor system with two different gRNAs directed to the promoter region  
1102 of the *Ilgax* locus. Top, flow cytometric dot plots of CD11b (y-axis) and MHC Class II (MHC-II, x-  
1103 axis); bottom, quantification of flow cytometric data for percentage of CD11b and MHC-II  
1104 expressing cells and the MFI of each marker (n=3 per condition). (N) *In silico* prediction of the  
1105 number of LINE1 gRNA targets (y-axis) according to the number of allowable mismatches  
1106 between gRNA and target sequences (color intensity). Above, pie charts exhibiting enrichment  
1107 of gRNA target sequences in LINE1 families. The most highly enriched family is denoted at the  
1108 top of each pie chart and the corresponding gRNA number is listed below. (O) Scatter dot plot  
1109 displaying the number of gRNA target sequences upstream of ISGs (blue circles) versus  
1110 targeted LINE1 elements (red circles). (P) ISG54-Luciferase assay of IFN-I and ISG induction  
1111 in resting and LPS-stimulated (8hrs) *Cgas*<sup>-/-</sup> RAW264.7 cells expressing mutant dCas9 KRAB  
1112 fusion protein and the indicated gRNA (Ctrl, gRNA\_1, or gRNA\_2; n=4 per group). Statistical  
1113 significance was determined by 2-way ANOVA and Bonferonni's ad hoc analysis for individual  
1114 comparisons: \* $P < 0.05$ , \*\*  $P < 0.001$ , \*\*\*  $P < 0.001$ , \*\*\*\*  $P < 0.0001$ .

1115  
1116 **Figure S6** IAV/PR8 infection can be assessed by flow cytometric measurement of cell survival  
1117 and viral nucleoprotein expression, related to figure 6. Top, flow cytometric dot plots of survival  
1118 5 days post infection (dpi) of DCs with IAV/PR8. Bottom, flow cytometric dot plots of IAV/PR8  
1119 NP protein expression 5 dpi with IAV/PR8 in the same sample as the corresponding plots  
1120 above.

1121

1122 **ACKNOWLEDGMENTS**



1123 We thank J.M. Carpier, M. Burbage, M. Maurin, M. Gros, S. Heurtebise, L. Menger, A. Alloatti,  
1124 and L. Joannas for assistance with various techniques and/or experiments. We thank R.E.  
1125 Vance, J. Barau, L. Quadrana, and H. Rich for helpful discussions; M. Terman and G. Schwed,  
1126 for helpful reading of the manuscript; S. A. Cros and S. Huertebise, for assistance with mice.  
1127 We also thank the genomic and animal facilities. We thank T. Jenuwein for providing the  
1128 *Suv39h1*-deficient mice. S. A. received funding from the Institut Curie; Institut National de la  
1129 Santé et de la Recherche Médicale; Centre National de la Recherche Scientifique; ANR  
1130 "ChromaTin" ANR-10-BLAN-1326-03, ANR "EPICURE" ANR-14-CE16-0009; S.A. received  
1131 funding from la Ligue Contre le Cancer (Equipe labellisée Ligue, EL2014.LNCC/SA);  
1132 Association de Recherche Contre le Cancer (ARC); grant ERC (2013-AdG N° 340046  
1133 DCBIOX); FP7\_HEALTH-2010-259743 "MODHEP", ANR-11-LABX-0044\_DEEP and ANR-10-  
1134 IDEX-0001-02\_PSL, ANR "CHAPINHIB" ANR-12-BSV5-0022-02, ANR "CELLECTCHIP" ANR-  
1135 14-CE10-0013 and Aviesan-ITMO cancer project "Epigenomics of breast cancer". D.C.R was  
1136 supported by funding from Institut National du Cancer (INCA) (grant 2017-1-PL BIO-05). High-  
1137 throughput sequencing has been performed by the ICGex NGS platform of the Institut Curie  
1138 supported by the grants ANR-10-EQPX-03 and ANR-10-INBS-09-08. N.M. and M.G. were  
1139 supported by ANR (ANR-17-CE15-0025-01 and ANR-14-CE14-0004-02) and ERC (309848)  
1140 grants to N.M. GK is supported by the Ligue contre le Cancer (équipe labellisée); Agence  
1141 National de la Recherche (ANR) – Projets blancs; AMMICA US23/CNRS UMS3655; Association  
1142 pour la recherche sur le cancer (ARC); Association "Ruban Rose"; Cancéropôle Ile-de-France;  
1143 Fondation pour la Recherche Médicale (FRM); a donation by Elior; Equipex Onco-Pheno-  
1144 Screen; European Joint Programme on Rare Diseases (EJPRD); Gustave Roussy Odyssey, the  
1145 European Union Horizon 2020 Projects Oncobiome and Crimson; Fondation Carrefour; Institut  
1146 National du Cancer (INCa); Inserm (HTE); Institut Universitaire de France; LabEx Immuno-  
1147 Oncology (ANR-18-IDEX-0001); the Leducq Foundation; the RHU Torino Lumière; Seerave  
1148 Foundation; SIRIC Stratified Oncology Cell DNA Repair and Tumor Immune Elimination  
1149 (SOCRATE); and SIRIC Cancer Research and Personalized Medicine (CARPEM). This study  
1150 contributes to the IdEx Université de Paris ANR-18-IDEX-0001.

1151

## 1152 **AUTHOR CONTRIBUTIONS**

1153 D.C.R. conceptualized, established, and performed histone ChIP-seq, cGAS-IP-seq protocols,  
1154 cGAS-IP-seq library preparation, cell stimulations, cytosolic DNA extraction, CRISPR-dCas9-  
1155 targeted suppression of LINE1 elements, lentiviral knockdown of *Suv39h1*, cGAS reconstitution,  
1156 and SUV39H1 overexpression, IFN $\beta$  and cytokine measurements, RNA-seq, and FACS  
1157 analysis. M.G. made eGFP-cGAS lentiviral constructs and performed shRNA-targeted  
1158 knockdown of SUV39H1 and stimulations in primary human MDDCs. N.B. and T.H. assisted  
1159 D.C.R. with various experiments. P.B. performed analysis of RNAseq data from MDDCs,  
1160 BMDCs and CRISPR-Cas9-KRAB suppression of LINE1. C.G. and M.Y. performed statistical  
1161 analyses and mapping of H3K9me3-ChIP, cGAS-IP sequencing, and mRNA-seq of *Suv39h1*WT  
1162 and KO BMDCs. N.M. supervised M.G. and contributed mice with an eGFP-tagged endogenous  
1163 cGAS allele. D.C.R, P.B., M.Y., and C.G. analyzed data. D.C.R., G.J.T., and R.M. wrote the  
1164 manuscript.

1165

## 1166 **DECLARATION OF INTERESTS**

1167 The authors declare no competing interests.



1168

## 1169 MATERIALS AND METHODS

### 1170 Mice

1171 *Suv39h1*KO(Peters et al., 2001) mice were from Thomas Jenuwein. *Mb21d1* (*Cgas*)<sup>-/-</sup> (*B6(C)-*  
1172 *Mb21d1*<sup>tm1d(EUCOMM)Hmgu/J</sup>) and *Mavs*<sup>-/-</sup> (*B6;129-Mavs*<sup>tm1Zjc/J</sup>) mice were from Jackson  
1173 laboratory. cGAS-eGFP-Knock-in mice, a gift from Nicolas Manel (*Mb21d1*<sup>(tm1Ciphe)</sup>; CIPHE) were  
1174 generated by targeted in-frame insertion of an enhanced GFP sequence after the ATG start  
1175 codon of the endogenous *Mb21d1* locus. *Trif*<sup>-/-</sup> (*C57BL/6J-Ticam1*<sup>Lps2/J</sup>) and *Myd88*<sup>-/-</sup>  
1176 (*B6.129P2(SJL)-Myd88*<sup>tm1.1Defr/J</sup>) were from Catherine Werts (Pasteur Institute) and *Ifnar*<sup>-/-</sup>  
1177 (*B6.129S2-Ifnar1*<sup>tm1Agt/Mmjax</sup>) mice were originally from JAX. *C57BL/6N* mice were originally  
1178 from Charles Rivers Laboratories. All mice were housed in SPF animal facilities, and live animal  
1179 experiments were performed in accordance with the European Veterinary Department (Project  
1180 Authorization N:02465.02).

1181

### 1182 Cell Culture

1183 Bone marrow-derived dendritic cells were cultivated in 20ng/ml GMCSF (Miltenyi) in IMDM  
1184 (VWR13390) supplemented with 10% fetal bovine serum (Eurobio), Penicillin/Streptomycin,  
1185 50μM -mercaptoethanol, minimal non-essential amino acids, and 2mM Glutamax (all from Life  
1186 Technologies) and referred to as I-10 medium. Briefly, fresh bone marrow was collected from  
1187 two of each—ilium, femur, and tibia—by centrifugation. Five million bone marrow cells were  
1188 seeded on untreated 10cm plates (VWR) in 10mls of I-10 medium. On day 3, an additional  
1189 10mls of I-10 medium was added, followed by collection and replenishment of 10 mls on day six  
1190 and on day eight if needed for use at day ten. BMDC clusters were harvested on day 8-10 in 5  
1191 mls of complete I-10 media at room temperature and then stimulated at 1-2x10<sup>6</sup> cells per well of  
1192 an untreated 6-well plate (Sigma M9062-100EA) in 2 mls of I-10 medium without GMCSF.

1193

### 1194 Cell stimulations

1195 Cell stimulations were performed for the indicated times with mammalian cell culture-derived  
1196 mouse IFNB (PBL, 12405), herring testes (HT)-DNA (1-4μg/ml as indicated; Sigma D6898-  
1197 250MG), LPS (100ng/ml, Invivogen), high molecular weight poly (I:C) (1-2μg/ml, Invivogen), or  
1198 2'-3'cGAMP (4μg/ml, Invivogen) for the specified times. For cytosolic delivery of HT-DNA,  
1199 poly(I:C), or 2'3'cGAMP, 12μg of PAMP and 12μl of Lipofectamine<sup>TM</sup> (Life Technologies,  
1200 11668019) were separately diluted in OptiMEM (ThermoFisher 3195062), incubated for 5  
1201 minutes at room temperature, then combined, mixed by pipetting, and rested for an additional  
1202 15 minutes at RT. Liposome-containing PAMPs were then diluted in complete medium to make  
1203 a concentrated working stock for cell stimulation. STING inhibitor (H-151, MedChem Express)  
1204 stock solution was stored in DMSO at -80°C. Cells were pretreated with H-151 or DMSO vehicle  
1205 for 2hrs before subsequent stimulation with PAMP or infection with IAV/PR8.

1206

1207 RAW264.7-ISG-Lucia cell lines (all from Invivogen) deleted for *Tmem173*(rawl-kostg),  
1208 *Mb21d1*(rawl-kocgas), *Mda5* (rawl-komda5), and *Rig-I*(rawl-korigi) carried a Lucia luciferase  
1209 reporter construct under control of an IFN-inducible ISG54 promoter (Invivogen) and were  
1210 cultured in DMEM containing 10% Serum (Fischer Scientific), 1% Penicillin/Streptomycin  
1211 (Fischer Scientific) and Zeocin (1μg/ml; Invivogen). Cell stimulations were performed for the

1212 indicated times with HT-DNA, LPS, poly(I:C), or 2'-3'cGAMP, at the indicated concentrations in  
1213 6-well or 96-well tissue culture treated plates (Costar) following the same protocol as for  
1214 BMDCs.

1215

#### 1216 **Dendritic cell infection wit IAV**

1217 IAV/PR8/34 H1N1 was purchased from Charles River Laboratories and was stored at -80°C.

1218 Both BMDCs (Figure 6C) or the previously described JAWS II (ATCC)(101) mouse bone  
1219 marrow-derived dendritic cell line (Figure 6B, D-G) was used for infection experiments. Briefly,  
1220 BMDCs or JAWS II cells were plated in serum-free IMDM media supplemented with non-  
1221 essential amino acids and infected with IAV/PR8 for 1hour at 37°C, before addition of complete  
1222 media with a final concentration of 10%FBS. Infections were allowed to proceed for the times  
1223 specified in figure legends. For RTI, treatment, emtricitabine and disoproxil fumarate were  
1224 administered two hours prior to inoculation and maintained at 10µM for the duration infection  
1225 (120hrs). DMSO vehicle control was administered alongside RTI treatment as a control.

1226

#### 1227 **Generation of *Ifnar*<sup>-/-</sup> and *Mavs*<sup>-/-</sup> RAW264.7 macrophage cell lines with CRISPR**

1228 WT RAW264.7 macrophages were deleted using recombinant Cas9 protein (IDT, Alt-R S.p. HiFi  
1229 Cas9 Nuclease V3) complexed with Tracr RNA and gRNAs targeting either *Ifnar1* (IDT pre-  
1230 design gRNA Mm.Cas9.IFNAR1.1AA, Mm.Cas9.IFNAR1.1AB), *Ifnar2* (IDT pre-design gRNA,  
1231 Mm.Cas9.IFNAR2.1AA, Mm.Cas9.IFNAR2.1AB), or *Mavs* (IDT pre-design gRNA,  
1232 Mm.Cas9.Mavs.1AA, Mm.Cas9.Mavs.1AL). Briefly, gRNAs and Tracr RNA duplexes were  
1233 generated by melting at 95°C for 5 minutes followed by downramping to 20°C at 5°C/minute.  
1234 Duplexed RNA was then combined with recombinant Cas9 in duplex buffer for 15 minutes at  
1235 room temperature to form Cas9 ribonucleoproteins (RNPs). WT RAW264.7 cells were subjected  
1236 to two rounds of nucleofection with Cas9-RNPs using the SF Cell Line 4D-Nucleofector X Kit S  
1237 (Lonza) and the 4D Nucleofector apparatus precisely as specified by the manufacturer. *Ifnar1*  
1238 and *Ifnar2* gRNAs were delivered in the first and second rounds of nucleofection, respectively;  
1239 both *Mavs* gRNAs were delivered in first and second rounds. *Ifnar* deletion was confirmed by  
1240 luciferase assay as described under “Luciferase assay” in response to 8 hrs stimulation with  
1241 titrated recombinant mammalian IFNB (PBL, 12405); *Mavs* deletion was confirmed by western  
1242 blot.

1243

#### 1244 **Suppression of LINE1 using CRISPR-dCas9-KRAB**

1245 In brief, two lentiviral vectros were used to target endogenous LINE1 elements in RAW264.7  
1246 macrophages. gRNAs were cloned into the puro-resistant pKLV2-U6gRNA5(BbsI)-  
1247 PGKpuro2ABFP-W(Tzelepis et al., 2016) vector. A second vector expressing dCas9-KRAB  
1248 under control of the SFFV promoter was co-transduced into cells(Gilbert et al., 2014) for  
1249 epigenetic suppression of gRNA targets. gRNAs against LINE1 5' regions were generated using  
1250 CRISPOR and selected based on their predicted *in silico* enrichment in full length LINE1  
1251 elements and paucity of genic targets.

1252

#### 1253 **Generation of human monocyte derived DCs (MDDCs)**

1254 Buffy coats were prepared from peripheral adult human blood and CD14<sup>+</sup> monocytes were  
1255 isolated by magnetic separation (Miltenyi 130-050-201). CD14<sup>+</sup> monocytes were differentiated

1256 into DCs (MDDCs) in RPMI containing Glutamax, supplemented with 10%FBS (GIBCO),  
1257 50µg/ml Gentamicin (GIBCO), 0.01M HEPES (GIBCO), 10ng/ml GM-CSF (Miltenyi premium  
1258 grade), and 50ng/ml IL-4 (Miltenyi premium grade) at a density of  $10^6$  cells/ml. Cells were  
1259 harvested on day 4 for further analyses.

1260

#### 1261 **Lentiviral transduction of human cells**

1262 Lentiviral particles were produced as previously described(Gentili et al., 2019). Briefly, 293FT in  
1263 one well of a 6-well were transfected with 1µg psPAX2, 0.4µg pCMV-VSV-G and 1.6µg of a  
1264 lentiviral vector (for human shSUV39H1, Sigma, TRCN0000157251, TRCN0000275323,  
1265 TRCN0000275322) using TransIT 293 (Mirus, Biomedex) in Optimem (GIBCO). 2.6µg of  
1266 pSIV3 and 0.4µg of pCMV-VSV-G were transfected into 293FT cells to generate SIV-VLPs.  
1267 Twelve to fourteen hours later, the medium was changed to 3 mls of MDDC culture medium  
1268 without cytokines. 30-32 hours later, supernatants were harvested, passaged over a 0.45µm  
1269 filter, and used immediately for transduction of freshly isolated CD14<sup>+</sup> monocytes at  $1.5 \times 10^6$   
1270 cells/well of a 6-well plate in 1ml of MDDC culture medium. 1 ml of each lentiviral particles and  
1271 SIV-VLPS were added to each well for 3mls final volume in the presence of protamine (8µg/ml).  
1272 48hrs after transduction, puromycin (2µg/ml, Invivogen) was added for selection of shRNA-  
1273 expressing cells. Cells were harvested on day 4 of culture, plated at 50,000 cells per well of a  
1274 96-well round bottom plate, and stimulated overnight with the indicated PAMPs.

1275

#### 1276 **Luciferase assay**

1277 Production of type-I IFN production in RAW264.7 macrophages was measured by production of  
1278 secreted luciferase under the control of the interferon-inducible ISG54 promoter. Briefly,  
1279 conditioned supernatants were collected after stimulation, and 10µl was quantified for secreted  
1280 luciferase (Renilla) activity in the presence of luciferase substrate (Quanti-Luc; rep-qIc2,  
1281 Invivogen). Luminescence was recorded on a FLUOstar OPTIMA microplate reader (BMG  
1282 Labtech).

1283

#### 1284 **IFN ELISA**

1285 IFN $\beta$  in conditioned supernatants was measured with the VeriKine Mouse Interferon Beta ELISA  
1286 Kit (PBL, 42400-1) precisely as specified in the manufacturer's protocol.

1287

#### 1288 **RNA purification, Sequencing, and qPCR**

1289 Following stimulation, BMDCs were harvested on ice, collected by centrifugation and  
1290 immediately dissolved in Trizol (Life Technologies, 15596018) and stored at -80°C until further  
1291 processing. RNA was separated from DNA and protein by chloroform extraction. Briefly, 100µl  
1292 chloroform was added to 1 ml of Trizol, mixed by shaking for 1 min and incubated for 5 minutes  
1293 at RT. After centrifugation (20,000 x g for 25 minutes at 4°C), 400µl of the RNA-containing  
1294 aqueous phase was removed and combined with 1µg of RNase-free glycogen (ThermoFischer)  
1295 and 500µg ice-cold isopropanol. The mixture was frozen overnight at -80°C and thawed on ice  
1296 before centrifugation (20,000 x g for 25 minutes at 4°C). The RNA pellet was air-dried for 30-  
1297 60minutes in a laminar hood, resuspended in 10µl RNase/DNase-free water, and the DNA  
1298 removed by in-solution DNase digestion (Qiagen's RNase-Free DNase Set, #Cat 79254) for 30  
1299 minutes at room-temperature. The resulting DNA-free RNA prep was further purified over

1300 Quiagen columns using the Qiagen RNeasy mini kit and eluted in RNase/DNase-free water.  
1301 RNA preparations performed with this protocol routinely yielded an A260/280 ratio above 2 and  
1302 averaging 2.08. HTS libraries were constructed using the TruSeq Stranded mRNA kit from  
1303 Illumina and sequenced to a depth of at least  $50 \times 10^6$  reads per sample using 100bp paired-end  
1304 sequencing.

1305  
1306 For qPCR, cDNA was generated from 500ng of RNA using random hexamers (Promega,  
1307 C1181) and the SuperScript III First-Strand kit (Thermo Fisher, 18080051) in a 20 $\mu$ l reaction.  
1308 2 $\mu$ l of RNaseH was added and the reaction carried out at 37°C for 20 minutes. Following cDNA  
1309 synthesis, 160 $\mu$ l of RNase/DNase-free H<sub>2</sub>O was added, and 4 $\mu$ l of this was used per qPCR  
1310 reaction containing 1 $\mu$ l of 5 $\mu$ M primers and 5 $\mu$ l of SybrGreen reagent (LifeTechnologies,  
1311 4367659). 10 $\mu$ l reactions were performed in a 384 well plate (Thermo Fisher, 4483319) on a  
1312 Vii7 thermal cycling system (Applied Biosystem).

1313

### 1314 **PolyA<sup>+</sup> RNA-Seq Analysis**

#### 1315 **Sequencing Data Processing**

1316 FASTQC [<http://www.bioinformatics.babraham.ac.uk/projects/fastqc/>.] was run on all samples to  
1317 assess the quality of sequencing. Raw sequences were mapped to the mouse mm10 reference  
1318 genome (Refseq) with STAR aligner (Spliced Transcripts Alignment to a Reference, version  
1319 2.5.0a) (Dobin et al., 2013). We used the option *--bamRemoveDuplicatesType UniqueIdentical*  
1320 to mark all multimappers, and duplicate unique mappers, *--outFilterMultimapNmax 100* that  
1321 correspond to the number of read alignments which will be output only if the read maps fewer  
1322 than this value.

1323

#### 1324 **TE Quantification and Intactness**

1325 We used the Homer Software as previously described. However, we considered only TEs for  
1326 the analysis if the row sum across all samples was FPKM 5. LINE1 and LTR elements greater  
1327 than or equal to 4kb in length were considered intact. SINE elements were considered intact  
1328 when they diverged less than 10% from their consensus sequences.

1329

#### 1330 **Differential Analysis**

1331 Using the raw reads matrix, we filtered out the non-expressed genes and TE separately by  
1332 requiring more than 5 reads in at least 2 samples for each features and normalized using  
1333 DESeq2 R-package v1.18.1 (Love et al., 2014). Then, the differential expression analysis was  
1334 performed using DESeq2, only the Benjamini Hochberg (BH) adjusted p-value below 0.05 were  
1335 considered as significant.

1336

#### 1337 **PCA**

1338 The PCA was performed using the Ade4 package(S Dray, 2007) of the R software (version  
1339 3.3.2). The barycenters were computed from the set of observations in each condition and  
1340 projected into the PCA plot.

1341

#### 1342 **Chromatin Immunoprecipitation (ChIP)-sequencing**

1343 Histone ChIP experiments were performed as previously specified (Blecher-Gonen, et al 2013)  
1344 with several changes. Briefly, harvested BMDCs were collected by centrifugation at 350 x g for  
1345 5 minutes and resuspended in 1ml of I-10 medium. Cells were cross-linked with 1%  
1346 formaldehyde (Euromedex) for 8 minutes at room temperature and the reaction quenched in  
1347 150mM glycine for 10 minutes. Cross-linked cells were collected by centrifugation (350 x g for 5  
1348 minutes at room temperature) and washed twice with cold PBS. Pelleted cells were  
1349 subsequently lysed to isolate cross-linked chromatin. For cytosolic extraction, cells were first  
1350 suspended at  $1 \times 10^6$  cells/100 $\mu$ l of lysis buffer 1 (LB1) (50mM Hepes (pH7.5), 140mM NaCl,  
1351 1mM EDTA (pH 8.0) , 10% glycerol, 0.75% NP-40, 0.25% Triton X-100) with protease inhibitors  
1352 (Roche 11873580001) and  $\text{Na}_3\text{VO}_4$  (180 $\mu$ g/ml) for 10 minutes on ice, followed by centrifugation  
1353 at 500 x g for 5 minutes at 4°C to separate cytosol and nuclei. Nuclear pellets were then  
1354 dissolved in lysis buffer X (LBX) (50mM Tris pH 8.0, 5mM EDTA pH 8.0, 0.25%SDS)  
1355 supplemented inhibitors at  $10^6$ cells/100 $\mu$ l and incubated on ice for an additional 10 minutes, and  
1356 then sonicated with a Bioruptor Pico (Diagenode) for 11 cycles (30 seconds on/off) at 4°C.  
1357 Lysates were cleared by centrifugation at 20,000 x g for 20 minutes at 4°C, snap frozen on  
1358 liquid  $\text{N}_2$ , and stored at -80°C until immunoprecipitation. Samples were thawed on ice and  
1359 diluted 1:1 with dilution buffer X (DBX) (50mM Tris pH8.0, 0.9%NP40, 350mM NaCl), followed  
1360 by the addition of either anti-H3K9me3 (Diagenode) or control rabbit IgG (Diagenode) and  
1361 rotated overnight at 4°C. The following day, 20 $\mu$ l of DBX-washed Magna ChIP Protein W+G  
1362 magnetic beads (Millipore) were added to each sample and rotated for 1hr at 4°C, followed by  
1363 washes and de-crosslinking exactly as described previously(Blecher-Gonen et al., 2013). DNA  
1364 fragments were purified by two-sided selection with SPRI beads (Beckman Coulter B23318)  
1365 according to the manufacturer's guidelines and Illumina sequencing libraries prepared with the  
1366 TruSeq ChIP Library Preparation Kit. 150bp paired-end sequencing of pooled libraries was  
1367 performed on a HiSeq 2500 (Illumina) platform in rapid run mode to yield  $50 \times 10^6$  reads per  
1368 sample.

1369  
1370

### 1371 **Cross-linked cytosolic and nuclear cGAS immunoprecipitation and next** 1372 **generation sequencing (NGS)**

1373 Cytosolic cGAS immunoprecipitation was carried out similar to histone ChIP  
1374 experiments with minor adjustments. Anti-GFP (ChromoTek) or control beads  
1375 (ChromoTek) were added to the appropriate cell number as indicated by the  
1376 manufacturer and incubated overnight with rotation at 4°C. The following day, samples  
1377 were collected with a magnet, transferred to a 96-well qPCR plate and washed, de-  
1378 crosslinked and purified as for histone ChIP. Purified cGAS-bound DNA was sheared to  
1379 a mean size of 200bp in 100 $\mu$ l of direct elution buffer (10 mM Tris-HCl (pH 8.0), 5 mM  
1380 EDTA (pH 8.0), 300 mM NaCl and 0.5% SDS (vol/vol) with a Covaris S220. Sheared  
1381 DNA was purified with Agencourt AMPure XP beads (Beckman Coulter). Illumina-based  
1382 libraries were prepared to preserve ssDNA, RNA:DNA hybrids, and dsDNA. Briefly,  
1383 DNA fragments were tailed and ligated with an adaptor, followed by primer-based PCR  
1384 extension of complementary DNA. A second adaptor was ligated to the 5' end of the  
1385 template strand. dsDNA species were amplified and indexed using barcoded primers for  
1386 Illumina-based high throughput sequencing, and 150bp paired-end sequencing of



1387 pooled libraries was performed on a HiSeq 2500 (Illumina) platform in rapid run mode to  
1388 yield  $50 \times 10^6$  reads per sample.

1389

### 1390 **Mapping**

1391 ChIP-seq reads were mapped to mouse genome build mm10 with Bowtie2 (v2.1.0)  
1392 (Langmead and Salzberg, 2012) using the global alignment mode allowing 1 mismatch in  
1393 seed alignment. We processed only mapped reads.

1394

### 1395 **Transposable elements and genes quantification.**

1396 For computing quantification of TE and gene levels, genome-mapped reads were used  
1397 with Homer Software (using analyzeRepeats.pl script) (Heinz et al., 2010). We used  
1398 different options : (i) *-noCondensing* to report the number of reads for each repeat  
1399 element separately or (ii) *-condenseL1* to condense reads from each repeat name on  
1400 one entry. Finally, the number of reads mapped to each TE was normalized to its length  
1401 and total number of genome-aligned reads (FPKM value, Fragments Per Kilobase of  
1402 exon model per Million mapped reads using (-rpkm). TE and genes with RPKM0.1 were  
1403 excluded. Using these parameters, 85,795 unique TEs and genes were kept for  
1404 analysis.

1405

### 1406 **Human MDDC RNAseq dataset**

1407 Publicly available RNA seq datasets from untreated and LPS stimulated human MDDCs  
1408 were downloaded from ENCODE (GSE94180) and aligned to the human genome using  
1409 the GRCh38/hg38 assembly.

1410

### 1411 **ChIP-Seq Analyses**

#### 1412 **Mapping**

1413 H3K9me3 ChIP-seq reads were mapped to mouse genome build mm10 with Bowtie2 (v2.1.0)  
1414 using the global alignment mode allowing 1 mismatch in seed alignment (Langmead and  
1415 Salzberg, 2012). We processed only mapped *reads* with high mapping quality (*MAPQ*  $\geq 20$ )  
1416 using samtools (v0.1.8).

1417

#### 1418 **Transposable elements and genes quantification**

1419 For computing quantification of TEs and genes levels, we used genome-mapped reads were  
1420 used with Homer Software (v4.7) (using analyzeRepeats.pl script) (Heinz et al., 2010). We used  
1421 different options : (i) *-noCondensing* to report the number of reads for each repeat element  
1422 separately or (ii) *-condenseL1* to condense reads from each repeat name on one entry. Finally,  
1423 the number of reads mapped to each TE was normalized to its length and total number of  
1424 genome-aligned reads (FPKM value, Fragments Per Kilobase of exon model per Million  
1425 mapped reads using (-rpkm).

1426

#### 1427 **Peak Calling and Annotation**

1428 Peak calling was performed with SICER v1.1 using parameters : '-W 200 -G 600', peaks at 1 %  
1429 FDR threshold (Xu et al., 2014). Annotation of Peaks was performed using Homer Software (with  
1430 AnnotatedPeaks.pl script).



1431

1432 **Bigwig files and coverage visualization**

1433 All Bigwig files were generated with merged biological replicates to improve the sensitivity by  
1434 increasing the depth of read coverage and normalized over own input ChIP-seq files using --  
1435 BamCompare (with options: --effectiveGenomeSize 2719482043 for mm10 and --binSize 10  
1436 and --normalizeUsing BPM) from deepTools (v3.1.1) (Ramirez et al., 2014). For heatmap  
1437 visualization were generated with --PlotHeatmap after to compute the matrix of scores per  
1438 genome regions generated by the tool --ComputeMatrix from deepTools Software. Steady state  
1439 H3K9me3 *Suv39h1*-dependent elements in WT vs KO (Figure 1C) were selected using *bedtools*  
1440 *intersect* (default parameters) with WT peak and *subtract* (-A) with KO peak.  
1441 H3K9me3 *Suv39h1*-dependent elements in untreated vs LPS-treated (2hr and 4hr) were  
1442 selected using *bedtools intersect* (default parameters) with UT peak and *subtract* (-A) with WT  
1443 2hr peak and WT 4hr peak.

1444

1445

1446 **PAGE and Western Blot**

1447 For some proteins including SUV39H1, cells were lysed with LBX supplemented with EDTA-free  
1448 protease inhibitors (Roche), phosphatase inhibitors (Halt phosphatase, ThermoFischer), and  
1449 benzonase. They were incubated on ice for 30 minutes, vortexed at high speed for 15 seconds  
1450 and then centrifuged for 10 minutes at 13,000xg, aliquoted, snap frozen on liquid nitrogen and  
1451 stored at -80°C until further processing. Samples were thawed on ice and denatured in Laemmli  
1452 sample buffer supplemented with fresh beta-mercaptoethanol for 15 minutes at 95°C. For  
1453 phosphorylated and corresponding total protein levels including IRF3 and STING, cells were  
1454 lysed in ice cold RIPA buffer (50mM Tris HCL, 150mM NaCl, 0.1% SDS, 0.5% DOC, 1%NP-40,  
1455 EDTA-free protease inhibitor (Roche), phosphatase inhibitors (Halt phosphatase,  
1456 ThermoFischer), and benzonase (ThermoFisher)). Lysates were incubated for 30 minutes on  
1457 ice, vortexed for 15 seconds at high speed, and centrifuged for 8 minutes at 8,000 x g. Clarified  
1458 lysates were aliquoted, snap frozen on liquid nitrogen and stored at -80°C. Samples were  
1459 thawed on ice and denatured in Laemmli sample buffer supplemented with fresh beta-  
1460 mercaptoethanol for 15 minutes at 95°C. Lysate from 10<sup>5</sup> cells were separated on 4–15% Mini  
1461 Protean TGX Stain-Free gels (BioRad) and dry transferred to PVDF membranes (Bio-Rad) with  
1462 the Trans-Blot Turbo Transfer System (Bio-Rad). In experiments where phosphor-STING was  
1463 measured, lysate from 8.5x10<sup>5</sup> cells was loaded per lane. Blots were blocked with TBS 0.05%  
1464 Tween20 (TBST) and 5% non-fat milk (Carnation, total protein) or 10% Roche blocking reagent  
1465 (phosphor-proteins) for 1hr at RT, rinsed in TBST, and then rocked overnight at 4°C in TBST  
1466 5% BSA (Fraction V, 04-100-812-C, Euromedex) with primary antibodies: cGAS (1:1000;  
1467 31659, CST), gp96 (1:1000; adi-spa-850-D, Enzo), Phosphor-IRF3 (Ser396)(1:1000; 29047,  
1468 CST), Phosphor-STING (1:1000; CST), Phosphor-NF-KappaB p65 (Ser536)(1:1000; 3033,  
1469 CST), Phosphor-TBK1/NAK (Ser172) (1:1000; 5483, CST), SUV39H1(1:500; 8729, CST), TBK1  
1470 (1:1000; 3504, CST), anti-RAB6 (1:1000, sc-310; Santa Cruz Biotechnology), Histone H3  
1471 (1:1000, CST), MDA5 (1:1000, CST). The following morning, blots were washed three times for  
1472 ten minutes each in TBST at RT and then rocked for 1hr at RT in blocking buffer containing  
1473 secondary antibodies (1:10,000; Jackson ImmunoResearch): anti-rat-horseradish-peroxidase  
1474 (HRP) (112-035-143) or anti-rabbit-HRP (111-036-046). Following 4 more washes, membranes

1475 were coated with an HRP substrate (Enhanced Chemiluminescence, 32106; Thermo Fisher  
1476 Scientific) and the images captured using a BioRad Chemidoc imager.

1477

### 1478 **Flow Cytometry**

1479 Surface staining, flow cytometry, and washes were performed in FACS buffer (2%FBS, 0.5mM  
1480 EDTA, PBS). BMDCs were surface-labeled with fluorochrome-coupled antibodies to the  
1481 following antigens (all 1:400): MHCII-v450 (Invivogen, 48-5321-82), CD11b-PerCP-Cy5.5  
1482 (Invivogen, 45-0112-82), CD11c-PE-Cy7(Invivogen, 25-0114-82), CD86-APC(BD Biosciences,  
1483 561964 ). Dead cells were identified by APC-Cy7 live-dead (eBioscience, L34975) staining. For  
1484 intracellular staining, BMDCs were fixed and permeabilized using the eBioscience FoxP3  
1485 staining kit according to the manufacturer's recommendations, followed by incubation with anti-  
1486 Viperin-PE (BD Biosciences,565196) with 1%normal mouse/rat serum (Sigma), and FC block  
1487 (1:200; BD Biosciences, 553141) in permeabilization buffer for 45 minutes at RT. Cells were  
1488 washed twice in permeabilization buffer and a second time in FACS buffer before flow  
1489 cytometric analysis. Flow cytometric data were collected on either a MacsQuant (Miltenyi) or a  
1490 FACSVerse(BDbiosciences).

1491

### 1492 **Cytosolic DNA isolation and RTI**

1493 Cytosolic DNA from  $2 \times 10^6$  BMDCs was isolated as previously described (42). After LPS  
1494 stimulation, BMDCs were harvested from 6-well dishes, washed twice in PBS, and resuspended  
1495 in 200 $\mu$ l of digitonin buffer (150mM NaCl, 50mM HEPES pH7.4, 25 $\mu$ g ml<sup>-1</sup> digitonin (Sigma)).  
1496 Samples were rotated end-over-end for 20 minutes at 4°C, cleared by centrifugation at 18,000 x  
1497 g for 10 minutes to collect nuclei and cellular debris which were then dissolved in LBX and  
1498 saved as the pellet fraction for normalization. Soluble material was treated with DNase-Free  
1499 RNaseA (20 $\mu$ g) (Thermo Fisher, ENO531) at 37°C for 1hr, followed by proteinase K (20 $\mu$ g)  
1500 (Thermo Fisher AM2548) for 1hr at 56°C. DNA was further purified with MinElute columns  
1501 (Qiagen, 28004) or with AmpureXP beads (Beckman Coulter) according the manufacturer's  
1502 guidelines and eluted in 250 $\mu$ l of DNase/RNase-free H<sub>2</sub>O. 4 $\mu$ l of DNA extract from cytosol or the  
1503 pellet fraction were amplified as described for qPCR of cDNA. For reverse transcriptase inhibitor  
1504 treatment, a combination of emtricitabine, tenofovir disoproxil fumarate, and nevirapine were  
1505 maintained at 10 $\mu$ M each in BMDC cultures from day 1 until the end of treatment. For control,  
1506 DMSO vehicle was maintained alongside RTI-treated cultures.

1507

### 1508 **Lentivirus and shRNA**

1509 Lentiviral shRNA (pLKO.1) plasmids for mouse Suv39h1 (7 $\mu$ g) (Sigma TRCN0000097439,  
1510 TRCN0000097440, TRCN0000097441, TRCN0000097443) or control shRNAs for GFP (Sigma)  
1511 and luciferase (Sigma) were combined with 7 $\mu$ g of psPAX2 packaging and 0.7 $\mu$ g of CMV-VSVg  
1512 envelope vectors in 1ml of OptiMEM medium. 45 $\mu$ l of room temperature Trans-IT 293  
1513 Transfection Reagent (Euromedex, Mirus 2700) was then added and the mixture incubated at  
1514 RT for 30 minutes. All contents were then delivered to HEK293FT cells that were plated in  
1515 10mls of DMEM (Gibco), 10%FBS (VWR, 11543387), 1%Penicillin, Streptomycin (Gibco) at 2-  
1516  $3 \times 10^6$  cell/10cm plate the previous night. The following morning, BSA (Sigma A7979) was  
1517 added to a final concentration of 1% and the viral supernatants harvested 24hrs later by  
1518 passaging through a 0.45 $\mu$ m filter. 2.5 mls of supernatant were then added to  $0.5 \times 10^6$  cells in

1519 0.5mls in a 6-well tissue culture-treated dish () and left overnight. Cells were washed the next  
1520 day and subjected to puromycin selection (2µg/ml, Invivogen ant-pr-5) 48hrs later. Knockdown  
1521 efficiency was assessed by western blotting or qPCR as specified.

1522

### 1523 **SUV39H1 cloning and overexpression**

1524 For mouse SUV39H1 overexpression studies, a previously described lentiviral expression  
1525 plasmid carrying RFP reporter and puromycin resistance genes (pL-  
1526 SFFV.Reporter.RFP657.PAC, Addgene#61395) was used with the following modifications. After  
1527 Agel digestion, PacI and AbsI sites were introduced and one of the Agel sites preserved  
1528 downstream of the SFFV promoter by polylinker ligation using the following oligos:  
1529 ACCGGTTTGGGATTAATTAATAATCACCTCGAGGCAGTCCGGT and  
1530 TGGCCAAACCCTAATTAATTTAGTGGAGCTCCGTCAGGCCA. In brief, oligos were  
1531 phosphorylated with T4 PNK (NEB) for 30 minutes at 37°C, denatured at 95°C for 5 minutes  
1532 and then ramped down to 25°C at 5°C per minute. Ligation proceeded overnight at 16°C using a  
1533 thermocycler, and bacterial transformation of NEB 10-beta competent E. coli (NEB)  
1534 accomplished by heat shock at 42°C. Minipreps were confirmed by Sanger sequencing.  
1535 Sequential digestion of modified pL-SFFV-RFP with Agel and BspEI were carried out at 37°C  
1536 with column purification between reactions (QIAquick, Quiagen). A mouse SUV39H1 gBlock  
1537 was synthesized (IDT) and cloned into Agel/BspEI-digested pL-SFFV-RFP using Gibson  
1538 assembly (NEB) for 1hour at 50°C. NEB10 (NEB) bacteria were transformed and selected on  
1539 ampicillin plates after 14hrs at 37°C. Minipreps were grown at 30°C over night with shaking at  
1540 250rpm. Plasmids constructs were confirmed by Sanger sequencing. The final SUV39H1  
1541 plasmid contained a P2A signal followed by the RFP reporter gene, and an internal ribosome  
1542 entry site (IRES), followed by the puromycin resistance gene.

1543

### 1544 **cGAS reconstitution**

1545 Human cGAS WT open reading frame was amplified by PCR from cDNA prepared from  
1546 monocyte-derived dendritic cells and was previously described (Gentili et al., Science 2015).  
1547 Murine cGAS WT open reading frame was amplified by PCR from cDNA prepared from C57BL6  
1548 murine bone-marrow derived dendritic cells and was previously described (Gentili et al., Science  
1549 2015). Human cGAS 161-522 C395A/C396A, and E225A/D227A were obtained by overlapping  
1550 PCR. pTRIP-SFFV was generated by substitution of the CMV promoter with the SFFV promoter  
1551 from GAE-SFFV-GFPWPRE and was previously described (Gentili et al., Science 2015, Raab  
1552 et al., Science, 2016). Murine cGAS cDNA, Human cGAS 161-522 E225A/D227A, and Human  
1553 cGAS 161-522 C395A/C396A were cloned in frame to EGFP in pTRIP-SFFV-EGFP to obtain  
1554 pTRIP-SFFV-EGFP-ms cGAS, pTRIP-SFFV-EGFP-cGAS 161-522 C395A/C396A, and pTRIP-  
1555 SFFV-EGFP-FLAG-cGAS 161-522 E225A/D227A. Lentiviral particles were generated as  
1556 described and used to transduce WT RAW264.7 macrophages.

1557

### 1558 **Software**

1559 Sequencing data was analyzed with R packages and R-Studio; heatmaps were generated using  
1560 Morpheus software from the Broad Institute (<https://software.broadinstitute.org/morpheus/>).  
1561 Flow cytometry data was analyzed with FloJo (Tree Star) v9.9.5. Graphs and statistical analysis

1562 were generated with Prism/Graphad (Version 7). Figure layouts were constructed with  
1563 Prism/Graphpad, Adobe Illustrator, and Adobe Photoshop.

1564

1565

## 1566 REFERENCES

- 1567 1. K. A. Fitzgerald, J. C. Kagan, Toll-like Receptors and the Control of Immunity. *Cell* **180**,  
1568 1044-1066 (2020).
- 1569 2. E. Bartok, G. Hartmann, Immune Sensing Mechanisms that Discriminate Self from  
1570 Altered Self and Foreign Nucleic Acids. *Immunity* **53**, 54-77 (2020).
- 1571 3. I. Rusinova *et al.*, Interferome v2.0: an updated database of annotated interferon-  
1572 regulated genes. *Nucleic Acids Res* **41**, D1040-1046 (2013).
- 1573 4. V. Hornung *et al.*, 5'-Triphosphate RNA is the ligand for RIG-I. *Science* **314**, 994-997  
1574 (2006).
- 1575 5. X. Li *et al.*, Structural basis of double-stranded RNA recognition by the RIG-I like  
1576 receptor MDA5. *Arch Biochem Biophys* **488**, 23-33 (2009).
- 1577 6. Q. Chen, L. Sun, Z. J. Chen, Regulation and function of the cGAS-STING pathway of  
1578 cytosolic DNA sensing. *Nat Immunol* **17**, 1142-1149 (2016).
- 1579 7. P. Gao *et al.*, Cyclic [G(2',5')pA(3',5')p] is the metazoan second messenger produced by  
1580 DNA-activated cyclic GMP-AMP synthase. *Cell* **153**, 1094-1107 (2013).
- 1581 8. L. Sun, J. Wu, F. Du, X. Chen, Z. J. Chen, Cyclic GMP-AMP synthase is a cytosolic DNA  
1582 sensor that activates the type I interferon pathway. *Science* **339**, 786-791 (2013).
- 1583 9. K. B. Chiappinelli *et al.*, Inhibiting DNA Methylation Causes an Interferon Response in  
1584 Cancer via dsRNA Including Endogenous Retroviruses. *Cell* **162**, 974-986 (2015).
- 1585 10. T. L. Cuellar *et al.*, Silencing of retrotransposons by SETDB1 inhibits the interferon  
1586 response in acute myeloid leukemia. *The Journal of cell biology* **216**, 3535-3549 (2017).
- 1587 11. G. D. Guler *et al.*, Repression of Stress-Induced LINE-1 Expression Protects Cancer  
1588 Cell Subpopulations from Lethal Drug Exposure. *Cancer Cell* **32**, 221-237 e213 (2017).
- 1589 12. C. A. Thomas *et al.*, Modeling of TREX1-Dependent Autoimmune Disease using Human  
1590 Stem Cells Highlights L1 Accumulation as a Source of Neuroinflammation. *Cell stem cell*  
1591 **21**, 319-331.e318 (2017).
- 1592 13. H. Tunbak *et al.*, The HUSH complex is a gatekeeper of type I interferon through  
1593 epigenetic regulation of LINE-1s. *Nat Commun* **11**, 5387 (2020).
- 1594 14. K. I. Leonova *et al.*, p53 cooperates with DNA methylation and a suicidal interferon  
1595 response to maintain epigenetic silencing of repeats and noncoding RNAs. *Proceedings*  
1596 *of the National Academy of Sciences of the United States of America* **110**, E89-98  
1597 (2013).
- 1598 15. C. R. Beck, J. L. Garcia-Perez, R. M. Badge, J. V. Moran, LINE-1 elements in structural  
1599 variation and disease. *Annual review of genomics and human genetics* **12**, 187-215  
1600 (2011).
- 1601 16. J. L. Goodier, Restricting retrotransposons: a review. *Mob DNA* **7**, 16 (2016).
- 1602 17. M. Dewannieux, C. Esnault, T. Heidmann, LINE-mediated retrotransposition of marked  
1603 Alu sequences. *Nat Genet* **35**, 41-48 (2003).
- 1604 18. D. Ribet, M. Dewannieux, T. Heidmann, An active murine transposon family pair:  
1605 retrotransposition of "master" MusD copies and ETn trans-mobilization. *Genome Res* **14**,  
1606 2261-2267 (2004).
- 1607 19. B. X. Yang *et al.*, Systematic identification of factors for provirus silencing in embryonic  
1608 stem cells. *Cell* **163**, 230-245 (2015).
- 1609 20. F. M. Jacobs *et al.*, An evolutionary arms race between KRAB zinc-finger genes  
1610 ZNF91/93 and SVA/L1 retrotransposons. *Nature* **516**, 242-245 (2014).



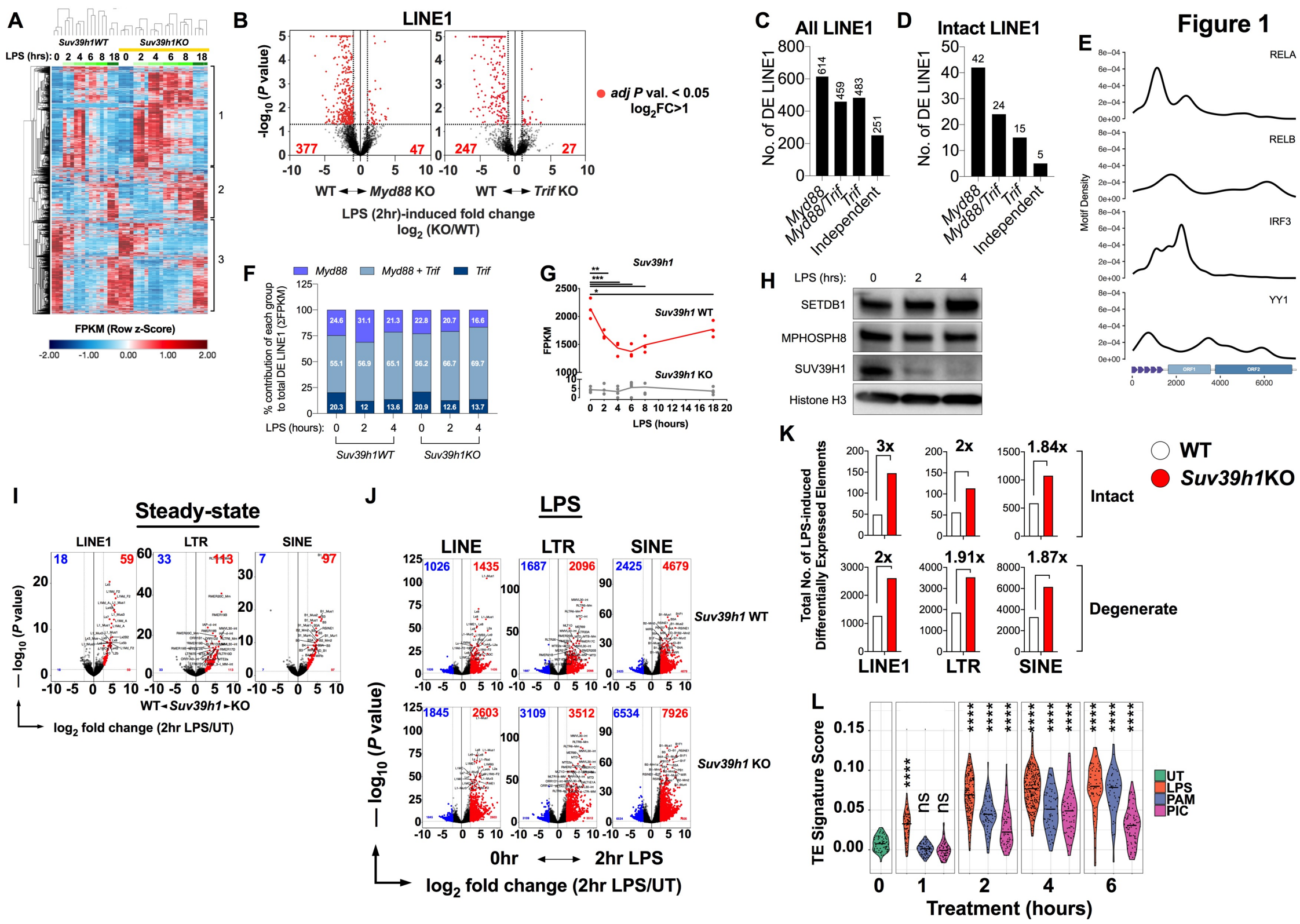
- 1611 21. J. Olejnik, A. J. Hume, E. Mühlberger, Toll-like receptor 4 in acute viral infection: Too  
1612 much of a good thing. *PLoS pathogens* **14**, e1007390 (2018).
- 1613 22. J. D.-T. Vincent F.-S. Shih, Monica Macal, Jenny Q. Huang, Julia Ponomarenko, Jeffrey  
1614 D. Kearns, Tony Yu, Riku Fagerlund, Masataka Asagiri, Elina I. Zuniga, and Alexander  
1615 Hoffmann, Control of RelB during dendritic cell activation integrates canonical and non-  
1616 canonical NF- $\kappa$ B pathways. *Nature Immunology* **13**, 1162-1170 (2012).
- 1617 23. M. Yamamoto *et al.*, Role of adaptor TRIF in the MyD88-independent toll-like receptor  
1618 signaling pathway. *Science* **301**, 640-643 (2003).
- 1619 24. M. Yamamoto *et al.*, Cutting edge: a novel Toll/IL-1 receptor domain-containing adapter  
1620 that preferentially activates the IFN-beta promoter in the Toll-like receptor signaling.  
1621 *Journal of immunology* **169**, 6668-6672 (2002).
- 1622 25. K. G. Becker, G. D. Swergold, K. Ozato, R. E. Thayer, Binding of the ubiquitous nuclear  
1623 transcription factor YY1 to a cis regulatory sequence in the human LINE-1 transposable  
1624 element. *Human molecular genetics* **2**, 1697-1702 (1993).
- 1625 26. J. L. Goodier, E. M. Ostertag, K. Du, H. H. Kazazian, Jr., A novel active L1  
1626 retrotransposon subfamily in the mouse. *Genome Res* **11**, 1677-1685 (2001).
- 1627 27. A. Bulut-Karslioglu *et al.*, Suv39h-dependent H3K9me3 marks intact retrotransposons  
1628 and silences LINE elements in mouse embryonic stem cells. *Molecular cell* **55**, 277-290  
1629 (2014).
- 1630 28. N. Liu *et al.*, Selective silencing of euchromatic L1s revealed by genome-wide screens  
1631 for L1 regulators. *Nature* **553**, 228-232 (2018).
- 1632 29. L. Robbez-Masson *et al.*, The HUSH complex cooperates with TRIM28 to repress young  
1633 retrotransposons and new genes. *Genome Res* **28**, 836-845 (2018).
- 1634 30. M. De Cecco *et al.*, L1 drives IFN in senescent cells and promotes age-associated  
1635 inflammation. *Nature* **566**, 73-78 (2019).
- 1636 31. M. Simon *et al.*, LINE1 Derepression in Aged Wild-Type and SIRT6-Deficient Mice  
1637 Drives Inflammation. *Cell Metab* **29**, 871-885.e875 (2019).
- 1638 32. P. Deininger *et al.*, A comprehensive approach to expression of L1 loci. *Nucleic Acids*  
1639 *Res* **45**, e31 (2017).
- 1640 33. C. Philippe *et al.*, Activation of individual L1 retrotransposon instances is restricted to  
1641 cell-type dependent permissive loci. *Elife* **5**, (2016).
- 1642 34. A. K. Shalek *et al.*, Single-cell RNA-seq reveals dynamic paracrine control of cellular  
1643 variation. *Nature* **510**, 363-369 (2014).
- 1644 35. P. J. Thompson *et al.*, hnRNP K coordinates transcriptional silencing by SETDB1 in  
1645 embryonic stem cells. *PLoS genetics* **11**, e1004933 (2015).
- 1646 36. D. Roulois *et al.*, DNA-Demethylating Agents Target Colorectal Cancer Cells by Inducing  
1647 Viral Mimicry by Endogenous Transcripts. *Cell* **162**, 961-973 (2015).
- 1648 37. E. E. Gray, P. M. Treuting, J. J. Woodward, D. B. Stetson, Cutting Edge: cGAS Is  
1649 Required for Lethal Autoimmune Disease in the Trex1-Deficient Mouse Model of Aicardi-  
1650 Goutieres Syndrome. *Journal of immunology* **195**, 1939-1943 (2015).
- 1651 38. J. Ahn *et al.*, Inflammation-driven carcinogenesis is mediated through STING. *Nat*  
1652 *Commun* **5**, 5166 (2014).
- 1653 39. D. B. Stetson, J. S. Ko, T. Heidmann, R. Medzhitov, Trex1 prevents cell-intrinsic  
1654 initiation of autoimmunity. *Cell* **134**, 587-598 (2008).
- 1655 40. J. W. Schoggins *et al.*, Pan-viral specificity of IFN-induced genes reveals new roles for  
1656 cGAS in innate immunity. *Nature* **505**, 691-695 (2014).
- 1657 41. S. M. Haag *et al.*, Targeting STING with covalent small-molecule inhibitors. *Nature* **559**,  
1658 269-273 (2018).
- 1659 42. P. Holden, W. A. Horton, Crude subcellular fractionation of cultured mammalian cell  
1660 lines. *BMC Res Notes* **2**, 243 (2009).

- 1661 43. M. Gentili *et al.*, The N-Terminal Domain of cGAS Determines Preferential Association  
1662 with Centromeric DNA and Innate Immune Activation in the Nucleus. *Cell Rep* **26**, 3798  
1663 (2019).
- 1664 44. M. H. Orzalli *et al.*, cGAS-mediated stabilization of IFI16 promotes innate signaling  
1665 during herpes simplex virus infection. *Proceedings of the National Academy of Sciences*  
1666 *of the United States of America* **112**, E1773-1781 (2015).
- 1667 45. H. E. Volkman, S. Cambier, E. E. Gray, D. B. Stetson, Tight nuclear tethering of cGAS is  
1668 essential for preventing autoreactivity. *Elife* **8**, (2019).
- 1669 46. J. A. Boyer *et al.*, Structural basis of nucleosome-dependent cGAS inhibition. *Science*  
1670 **370**, 450-454 (2020).
- 1671 47. T. Kujirai *et al.*, Structural basis for the inhibition of cGAS by nucleosomes. *Science* **370**,  
1672 455-458 (2020).
- 1673 48. S. Michalski *et al.*, Structural basis for sequestration and autoinhibition of cGAS by  
1674 chromatin. *Nature*, (2020).
- 1675 49. G. R. Pathare *et al.*, Structural mechanism of cGAS inhibition by the nucleosome.  
1676 *Nature*, (2020).
- 1677 50. B. Zhao *et al.*, The molecular basis of tight nuclear tethering and inactivation of cGAS.  
1678 *Nature*, (2020).
- 1679 51. S. Ahmad *et al.*, Breaching Self-Tolerance to Alu Duplex RNA Underlies MDA5-  
1680 Mediated Inflammation. *Cell* **172**, 797-810.e713 (2018).
- 1681 52. A. M. Herzner *et al.*, Sequence-specific activation of the DNA sensor cGAS by Y-form  
1682 DNA structures as found in primary HIV-1 cDNA. *Nat Immunol* **16**, 1025-1033 (2015).
- 1683 53. P. J. Kranzusch, A. S. Lee, J. M. Berger, J. A. Doudna, Structure of human cGAS  
1684 reveals a conserved family of second-messenger enzymes in innate immunity. *Cell Rep*  
1685 **3**, 1362-1368 (2013).
- 1686 54. A. K. Mankan *et al.*, Cytosolic RNA:DNA hybrids activate the cGAS-STING axis. *EMBO*  
1687 *J* **33**, 2937-2946 (2014).
- 1688 55. K. C. Barnett *et al.*, Phosphoinositide Interactions Position cGAS at the Plasma  
1689 Membrane to Ensure Efficient Distinction between Self- and Viral DNA. *Cell*, (2019).
- 1690 56. A. Lee, E. B. Park, J. Lee, B. S. Choi, S. J. Kang, The N terminus of cGAS de-  
1691 oligomerizes the cGAS:DNA complex and lifts the DNA size restriction of core-cGAS  
1692 activity. *FEBS Lett* **591**, 954-961 (2017).
- 1693 57. J. Tao *et al.*, Nonspecific DNA Binding of cGAS N Terminus Promotes cGAS Activation.  
1694 *Journal of immunology* **198**, 3627-3636 (2017).
- 1695 58. D. A. Sliter *et al.*, Parkin and PINK1 mitigate STING-induced inflammation. *Nature* **561**,  
1696 258-262 (2018).
- 1697 59. F. Civril *et al.*, Structural mechanism of cytosolic DNA sensing by cGAS. *Nature* **498**,  
1698 332-337 (2013).
- 1699 60. O. C. Cory J. Smith, Khaled Said, Verena Volf, Parastoo Khoshakhlagh, Amanda  
1700 Hornick, Raphael Ferreira, Chun-Ting Wu, Marc Güell, Shilpa Garg, Hannu Myllykallio,  
1701 George M. Church, Enabling large-scale genome editing by reducing DNA nicking.  
1702 *BioRxiv*, (2019).
- 1703 61. P. I. Thakore, J. B. Black, I. B. Hilton, C. A. Gersbach, Editing the epigenome:  
1704 technologies for programmable transcription and epigenetic modulation. *Nat Methods*  
1705 **13**, 127-137 (2016).
- 1706 62. C. J. Neufeldt *et al.*, SARS-CoV-2 infection induces a pro-inflammatory cytokine  
1707 response through cGAS-STING and NF- $\kappa$ B. *bioRxiv*, 2020.2007.2021.212639 (2020).
- 1708 63. G. Ni, Z. Ma, B. Damania, cGAS and STING: At the intersection of DNA and RNA virus-  
1709 sensing networks. *PLoS pathogens* **14**, e1007148 (2018).
- 1710 64. N. Schmidt *et al.*, An influenza virus-triggered SUMO switch orchestrates co-opted  
1711 endogenous retroviruses to stimulate host antiviral immunity. *Proceedings of the*



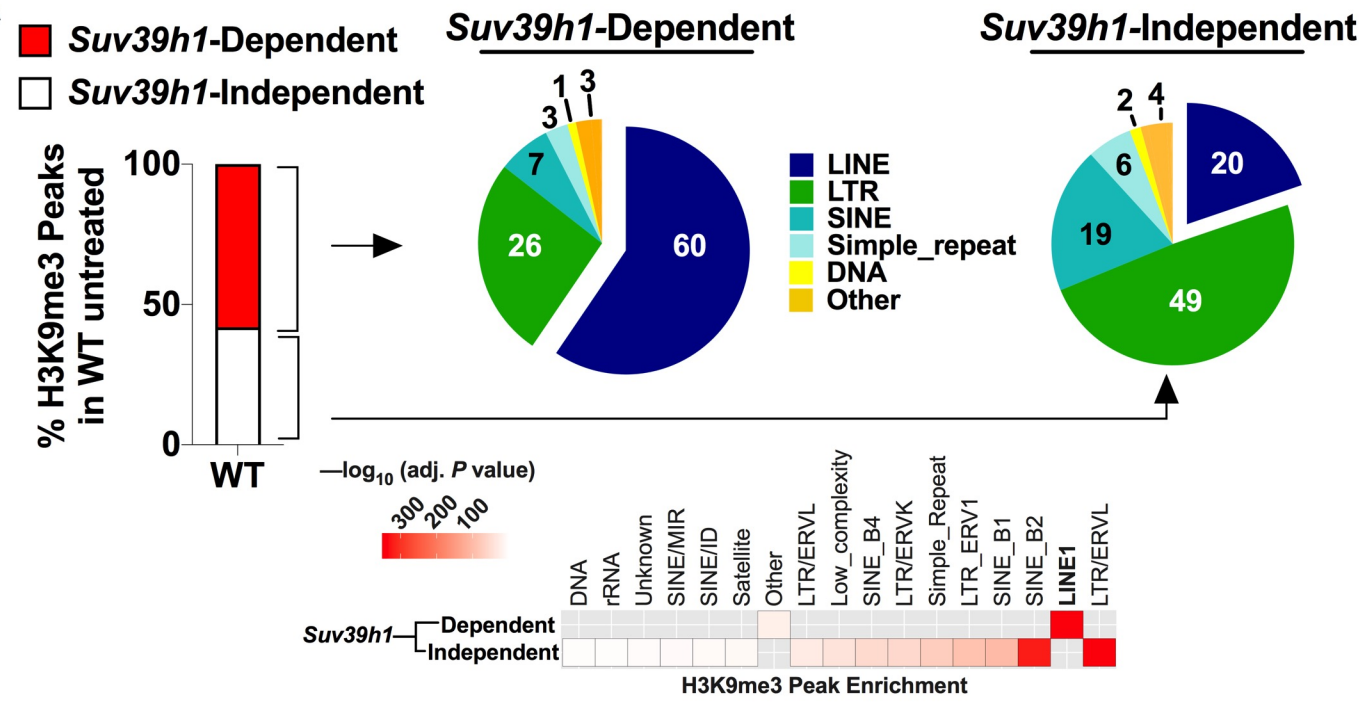
- 1712 *National Academy of Sciences of the United States of America* **116**, 17399-17408  
1713 (2019).
- 1714 65. M. Sorek, E. Meshorer, S. Schlesinger, Transposable elements as sensors of SARS-  
1715 CoV-2 infection. *bioRxiv*, 2021.2002.2025.432821 (2021).
- 1716 66. D. C. Hancks, H. H. Kazazian, Jr., Roles for retrotransposon insertions in human  
1717 disease. *Mob DNA* **7**, 9 (2016).
- 1718 67. H. S. Jang *et al.*, Transposable elements drive widespread expression of oncogenes in  
1719 human cancers. *Nat Genet* **51**, 611-617 (2019).
- 1720 68. L. M. Payer, K. H. Burns, Transposable elements in human genetic disease. *Nat Rev*  
1721 *Genet* **20**, 760-772 (2019).
- 1722 69. Y. Zheng, J. D. Tipton, P. M. Thomas, N. L. Kelleher, S. M. Sweet, Site-specific human  
1723 histone H3 methylation stability: fast K4me3 turnover. *Proteomics* **14**, 2190-2199 (2014).
- 1724 70. G. B. Beck-Engeser, D. Eilat, M. Wabl, An autoimmune disease prevented by anti-  
1725 retroviral drugs. *Retrovirology* **8**, 91 (2011).
- 1726 71. G. I. Rice *et al.*, Reverse-Transcriptase Inhibitors in the Aicardi-Goutieres Syndrome. *N*  
1727 *Engl J Med* **379**, 2275-2277 (2018).
- 1728 72. C. Esnault, J. Maestre, T. Heidmann, Human LINE retrotransposons generate  
1729 processed pseudogenes. *Nat Genet* **24**, 363-367 (2000).
- 1730 73. J. L. Garcia-Perez, A. J. Doucet, A. Bucheton, J. V. Moran, N. Gilbert, Distinct  
1731 mechanisms for trans-mediated mobilization of cellular RNAs by the LINE-1 reverse  
1732 transcriptase. *Genome Res* **17**, 602-611 (2007).
- 1733 74. N. Gilbert, S. Lutz, T. A. Morrish, J. V. Moran, Multiple fates of L1 retrotransposition  
1734 intermediates in cultured human cells. *Mol Cell Biol* **25**, 7780-7795 (2005).
- 1735 75. D. C. Hancks, J. L. Goodier, P. K. Mandal, L. E. Cheung, H. H. Kazazian, Jr.,  
1736 Retrotransposition of marked SVA elements by human L1s in cultured cells. *Human*  
1737 *molecular genetics* **20**, 3386-3400 (2011).
- 1738 76. W. Wei *et al.*, Human L1 retrotransposition: cis preference versus trans  
1739 complementation. *Mol Cell Biol* **21**, 1429-1439 (2001).
- 1740 77. D. Cao, X. Han, X. Fan, R. M. Xu, X. Zhang, Structural basis for nucleosome-mediated  
1741 inhibition of cGAS activity. *Cell Res*, (2020).
- 1742 78. A. P. West *et al.*, Mitochondrial DNA stress primes the antiviral innate immune response.  
1743 *Nature* **520**, 553-557 (2015).
- 1744 79. J. J. Chiang *et al.*, Viral unmasking of cellular 5S rRNA pseudogene transcripts induces  
1745 RIG-I-mediated immunity. *Nat Immunol* **19**, 53-62 (2018).
- 1746 80. D. S. Lima-Junior *et al.*, Endogenous retroviruses promote homeostatic and  
1747 inflammatory responses to the microbiota. *Cell* **184**, 3794-3811.e3719 (2021).
- 1748 81. Z. Ma, B. Damania, The cGAS-STING Defense Pathway and Its Counteraction by  
1749 Viruses. *Cell host & microbe* **19**, 150-158 (2016).
- 1750 82. M. Iampietro *et al.*, Activation of cGAS/STING pathway upon paramyxovirus infection.  
1751 *iScience* **24**, 102519 (2021).
- 1752 83. M. G. Ferrarini *et al.*, Genome-wide bioinformatic analyses predict key host and viral  
1753 factors in SARS-CoV-2 pathogenesis. *Communications biology* **4**, 590 (2021).
- 1754 84. C. K. Holm *et al.*, Influenza A virus targets a cGAS-independent STING pathway that  
1755 controls enveloped RNA viruses. *Nat Commun* **7**, 10680 (2016).
- 1756 85. X. Chen *et al.*, SARS coronavirus papain-like protease inhibits the type I interferon  
1757 signaling pathway through interaction with the STING-TRAF3-TBK1 complex. *Protein &*  
1758 *cell* **5**, 369-381 (2014).
- 1759 86. L. Sun *et al.*, Coronavirus papain-like proteases negatively regulate antiviral innate  
1760 immune response through disruption of STING-mediated signaling. *PLoS One* **7**, e30802  
1761 (2012).

- 1762 87. Y. Rui *et al.*, Unique and complementary suppression of cGAS-STING and RNA  
1763 sensing- triggered innate immune responses by SARS-CoV-2 proteins. *Signal*  
1764 *transduction and targeted therapy* **6**, 123 (2021).
- 1765 88. J. C. Yaling Xing, Jian Tu, Bailing Zhang, Xiaojuan Chen, Hongyan Shi, Susan C Baker,  
1766 Li Feng, Zhongbin Chen, The papain-like protease of porcine epidemic diarrhea virus  
1767 negatively regulates type I interferon pathway by acting as a viral deubiquitinase. *The*  
1768 *Journal of General Virology* **94**, 1554-1567 (2013).
- 1769 89. S. Aguirre *et al.*, Dengue virus NS2B protein targets cGAS for degradation and prevents  
1770 mitochondrial DNA sensing during infection. *Nat Microbiol* **2**, 17037 (2017).
- 1771 90. H. Ishikawa, Z. Ma, G. N. Barber, STING regulates intracellular DNA-mediated, type I  
1772 interferon-dependent innate immunity. *Nature* **461**, 788-792 (2009).
- 1773 91. Y. Zheng *et al.*, Zika virus elicits inflammation to evade antiviral response by cleaving  
1774 cGAS via NS1-caspase-1 axis. *Embo j* **37**, (2018).
- 1775 92. Q. Ding *et al.*, Hepatitis C virus NS4B blocks the interaction of STING and TBK1 to  
1776 evade host innate immunity. *Journal of hepatology* **59**, 52-58 (2013).
- 1777 93. M. S. Rooney, S. A. Shukla, C. J. Wu, G. Getz, N. Hacohen, Molecular and genetic  
1778 properties of tumors associated with local immune cytolytic activity. *Cell* **160**, 48-61  
1779 (2015).
- 1780 94. P. Mehdipour *et al.*, Epigenetic therapy induces transcription of inverted SINEs and  
1781 ADAR1 dependency. *Nature* **588**, 169-173 (2020).
- 1782 95. J. Z. Shen *et al.*, FBXO44 promotes DNA replication-coupled repetitive element silencing  
1783 in cancer cells. *Cell* **184**, 352-369.e323 (2021).
- 1784 96. W. Sheng *et al.*, LSD1 Ablation Stimulates Anti-tumor Immunity and Enables Checkpoint  
1785 Blockade. *Cell* **174**, 549-563.e519 (2018).
- 1786 97. G. K. Griffin *et al.*, Epigenetic silencing by SETDB1 suppresses tumour intrinsic  
1787 immunogenicity. *Nature* **595**, 309-314 (2021).
- 1788 98. H. Konno *et al.*, Suppression of STING signaling through epigenetic silencing and  
1789 missense mutation impedes DNA damage mediated cytokine production. *Oncogene* **37**,  
1790 2037-2051 (2018).
- 1791 99. M. A. Suter *et al.*, cGAS-STING cytosolic DNA sensing pathway is suppressed by JAK2-  
1792 STAT3 in tumor cells. *Sci Rep* **11**, 7243 (2021).
- 1793 100. T. T. Chen *et al.*, SUV39H1 Reduction Is Implicated in Abnormal Inflammation in COPD.  
1794 *Sci Rep* **7**, 46667 (2017).
- 1795 101. X. Jiang, C. Shen, J. Rey-Ladino, H. Yu, R. C. Brunham, Characterization of murine  
1796 dendritic cell line JAWS II and primary bone marrow-derived dendritic cells in Chlamydia  
1797 muridarum antigen presentation and induction of protective immunity. *Infection and*  
1798 *immunity* **76**, 2392-2401 (2008).
- 1799

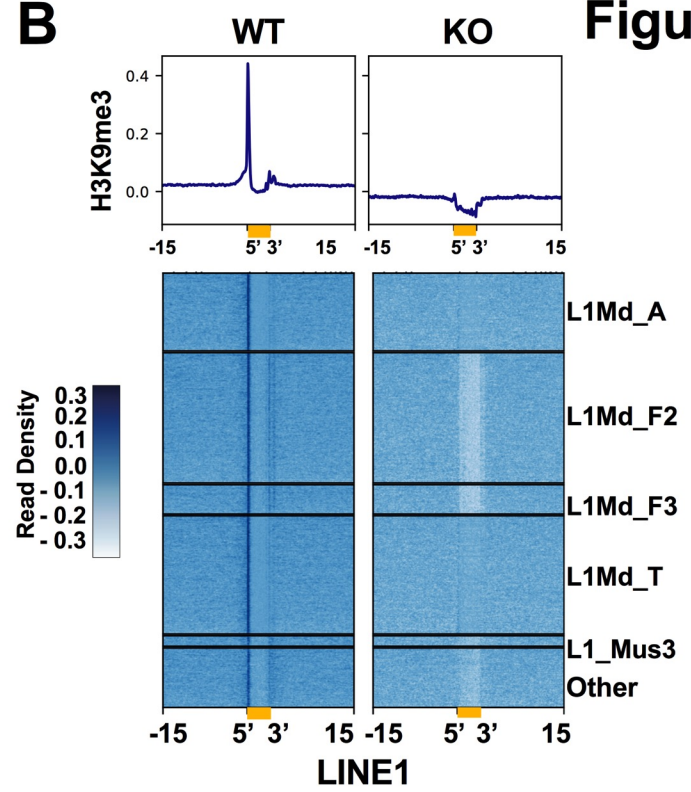




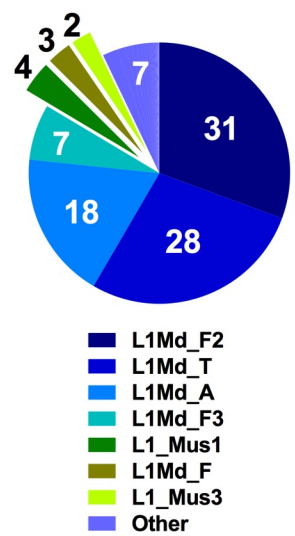
**A**



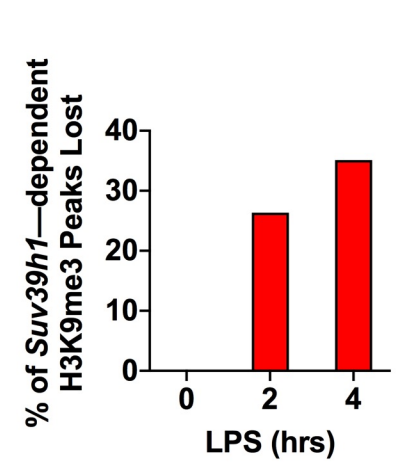
**B**



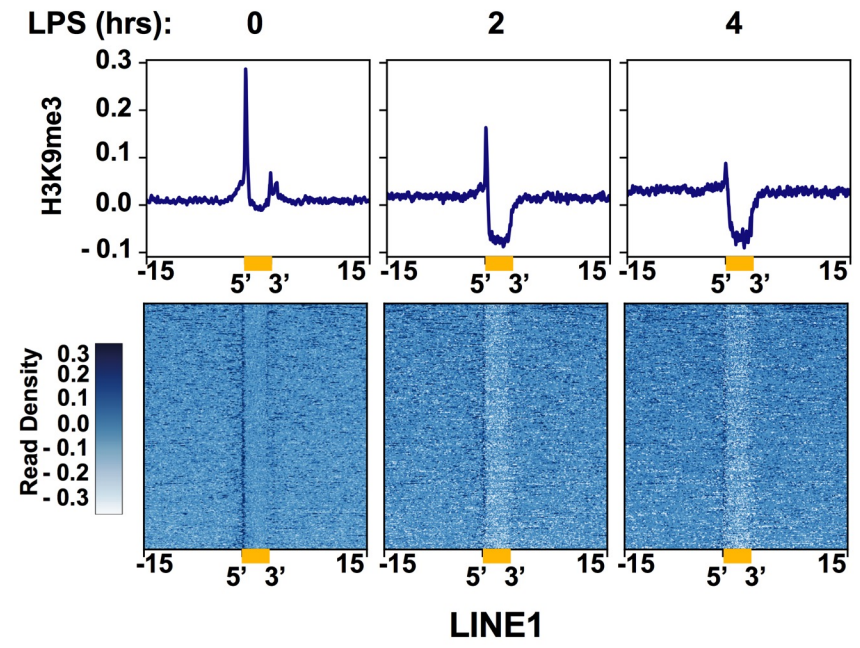
**C**



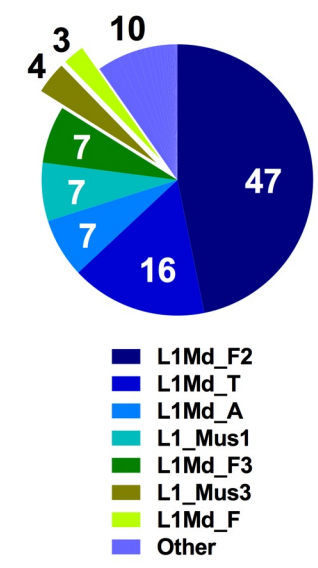
**D**



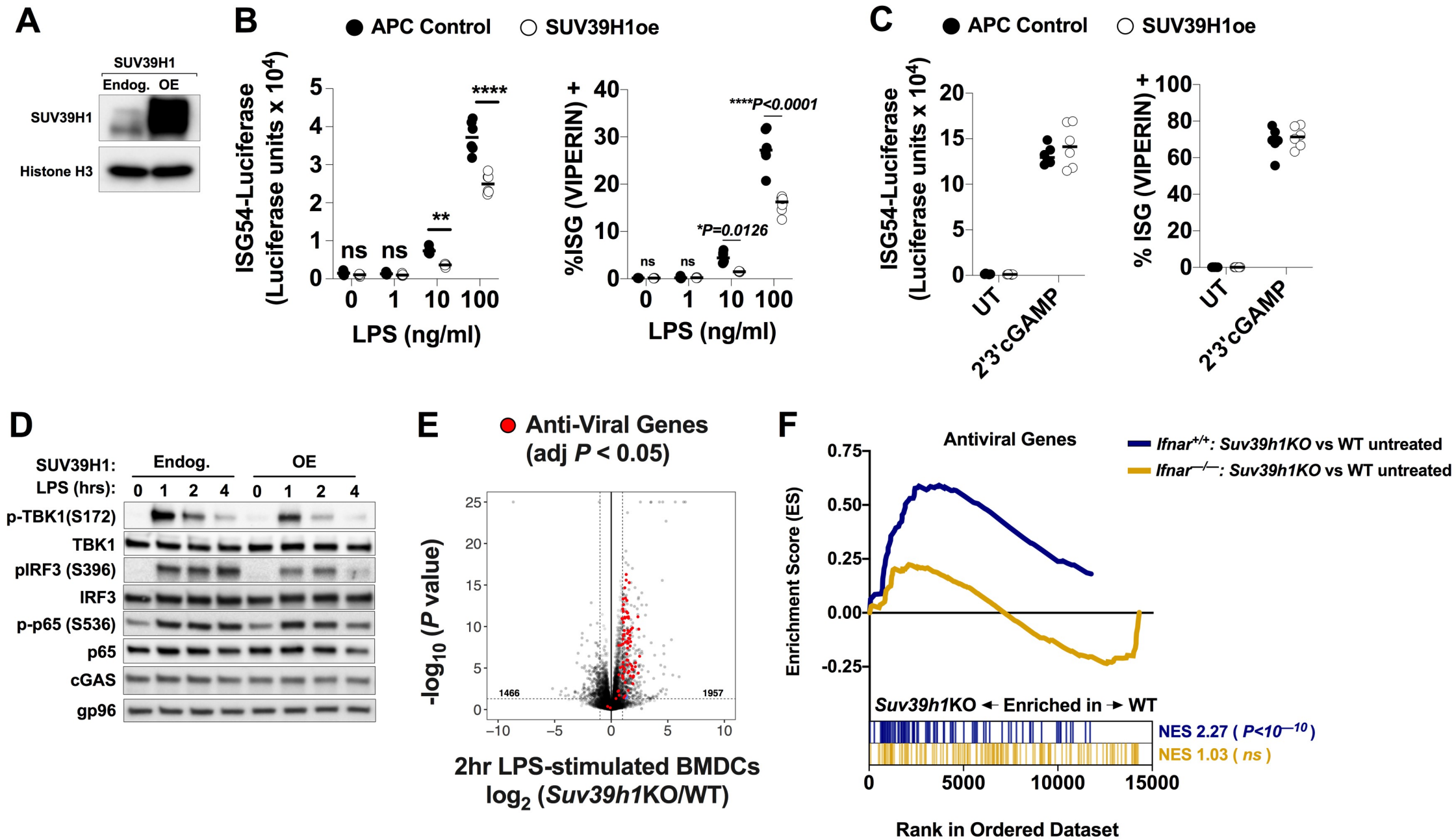
**E**

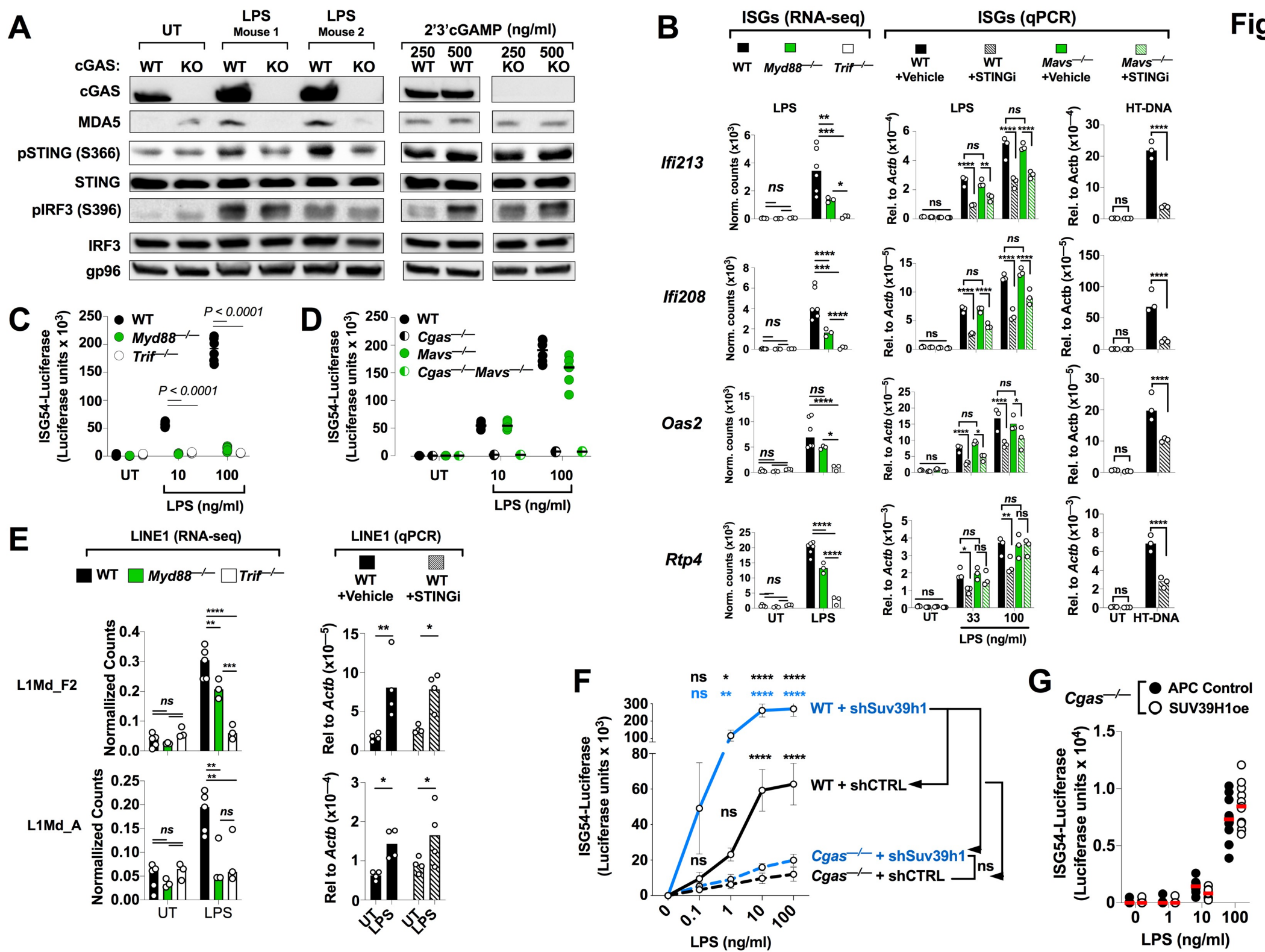


**F**

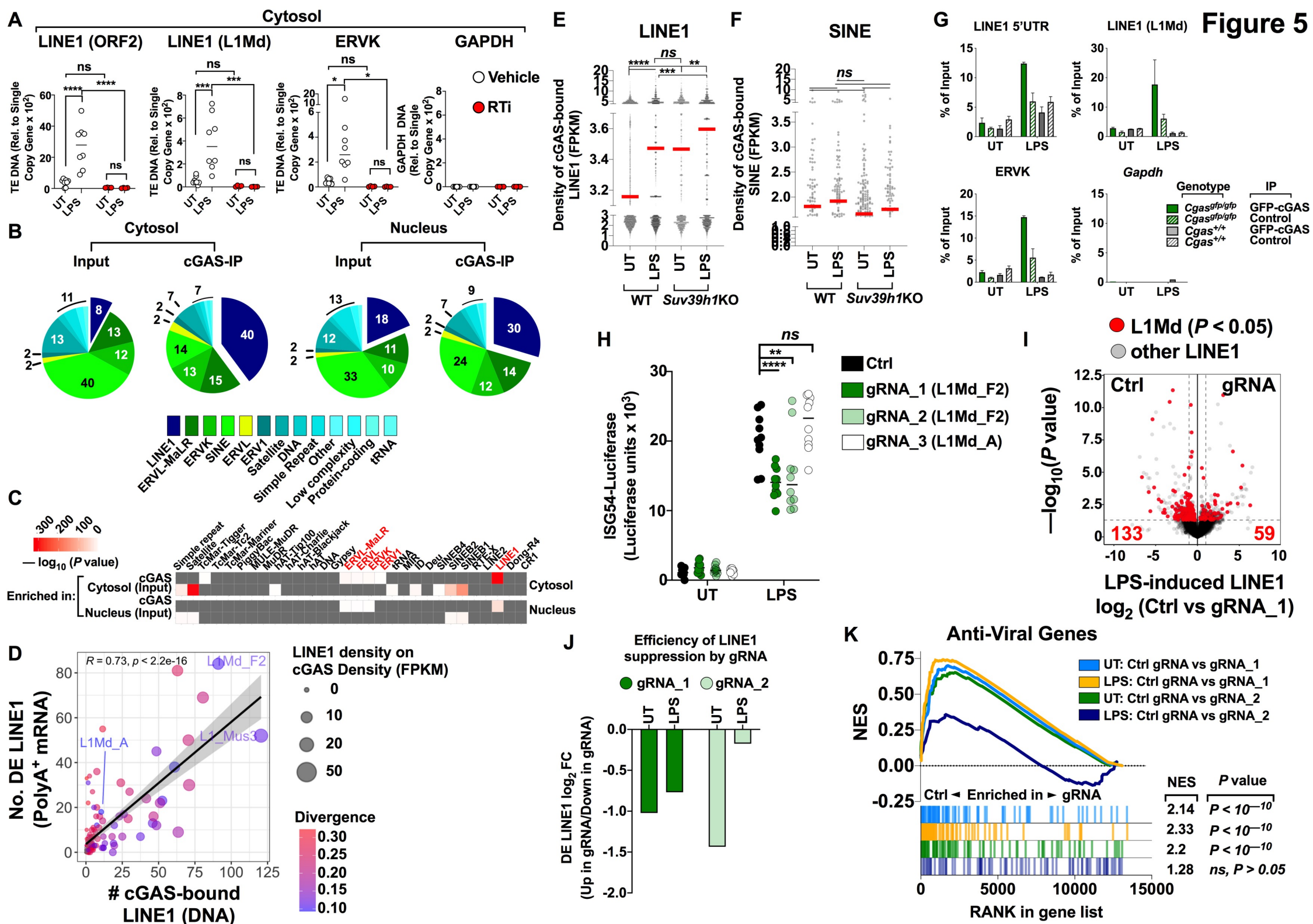


**Figure 3**

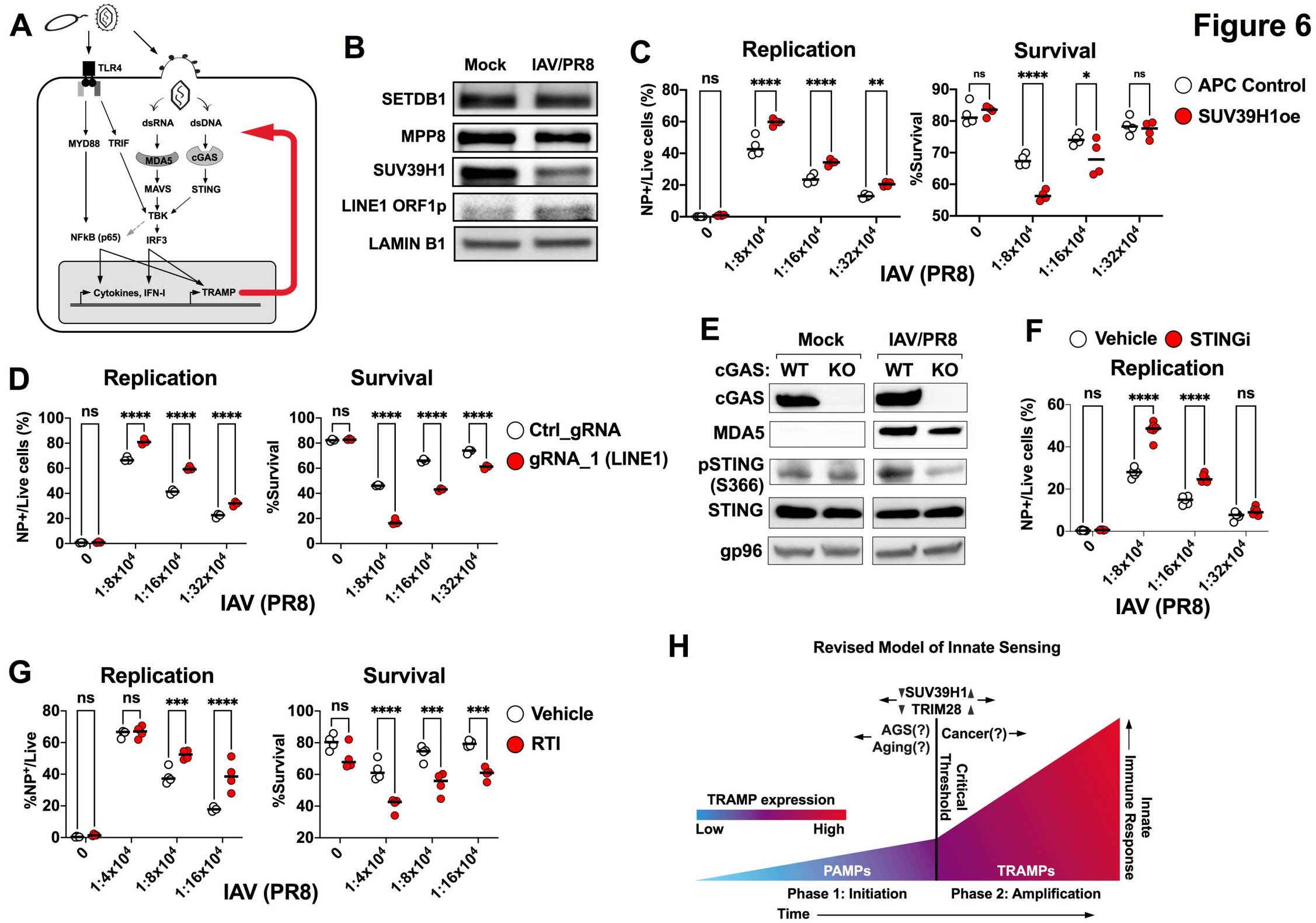




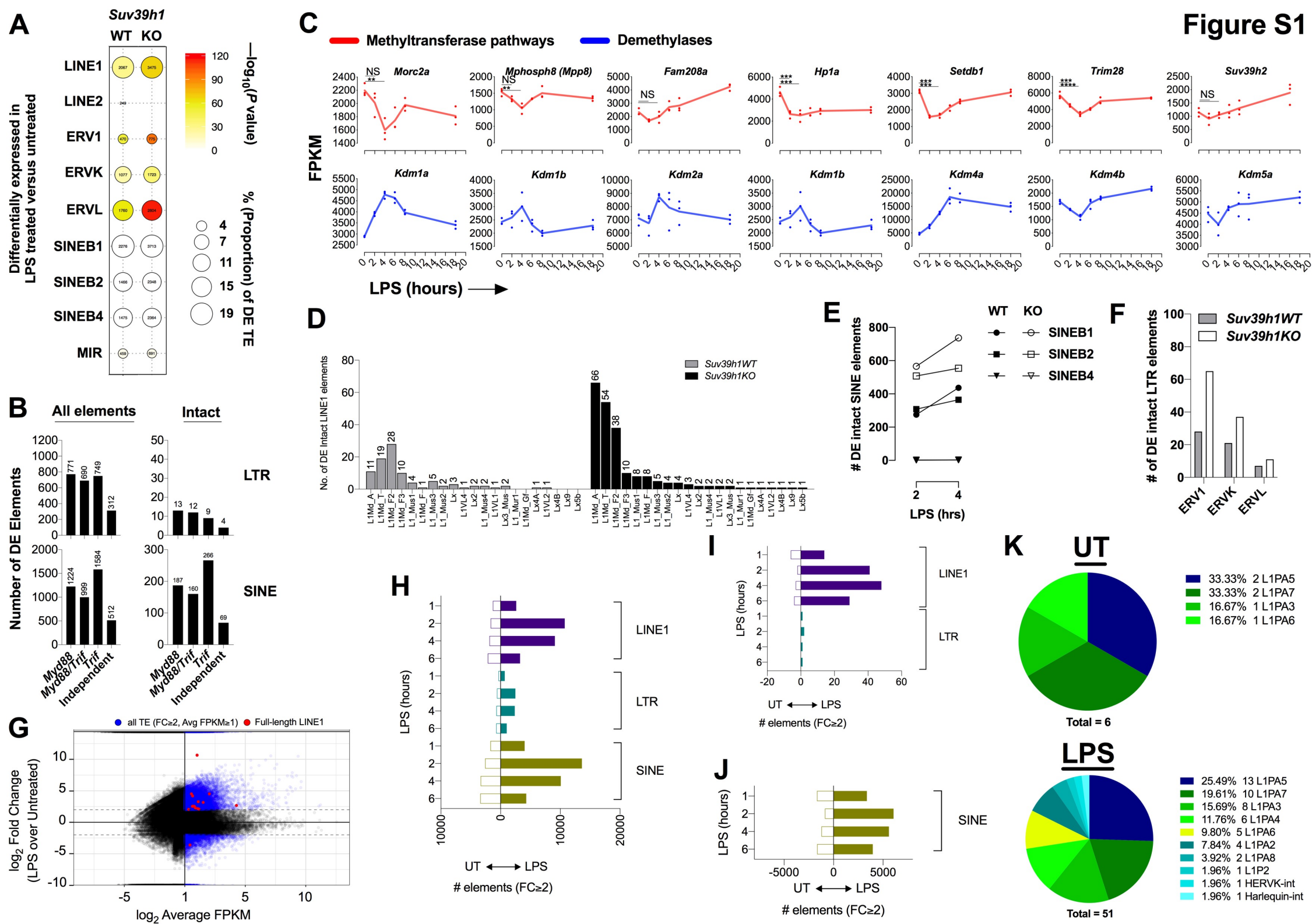




**Figure 6**







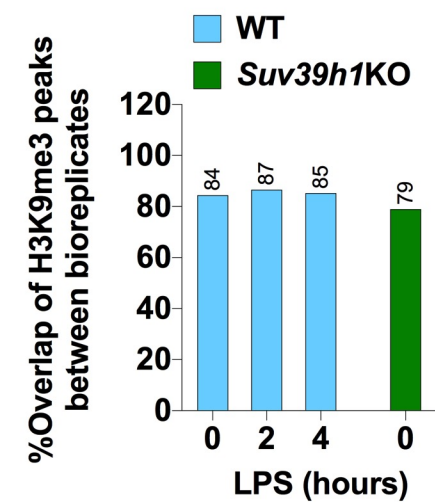
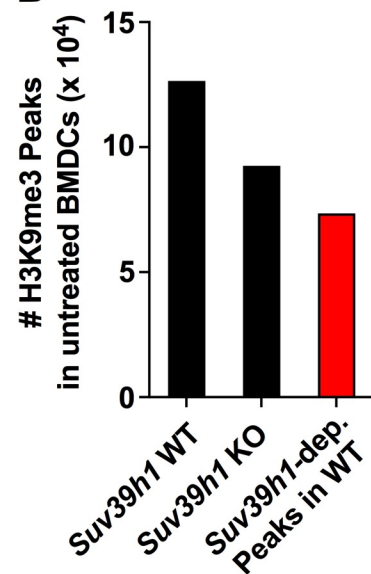
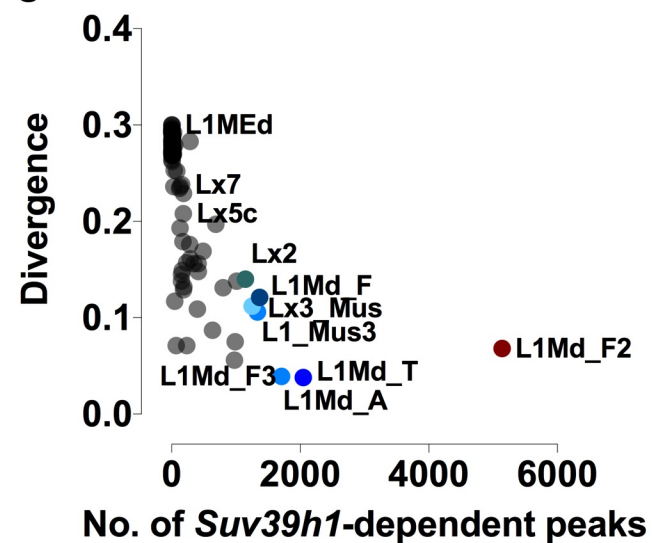
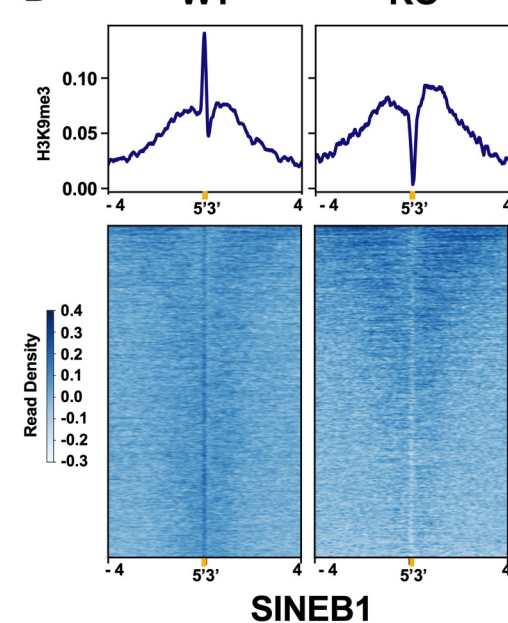
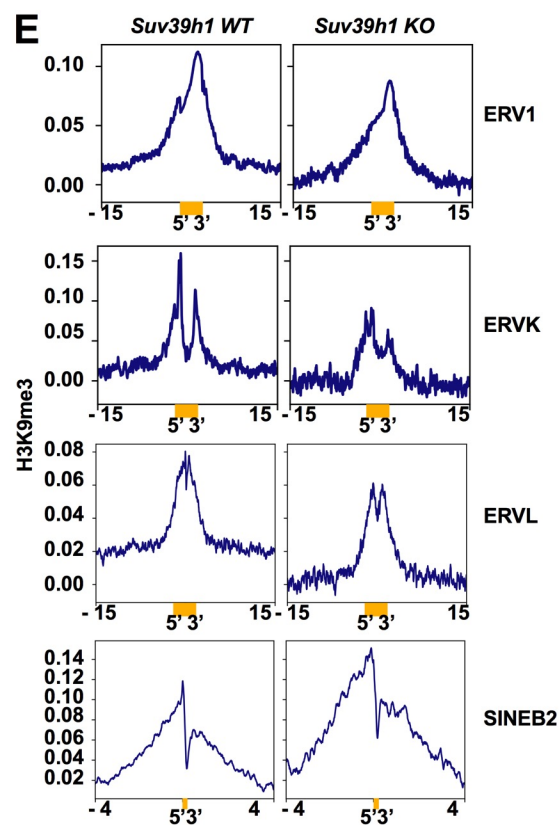
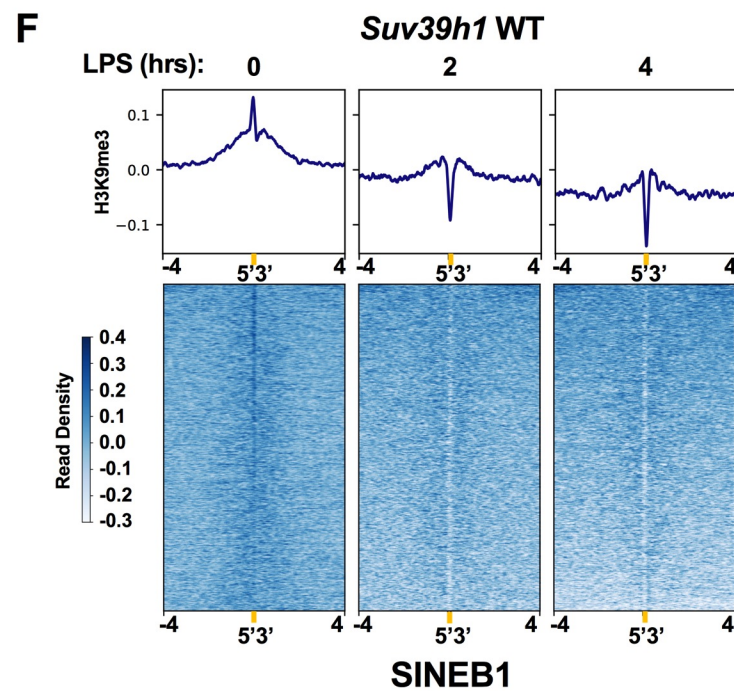
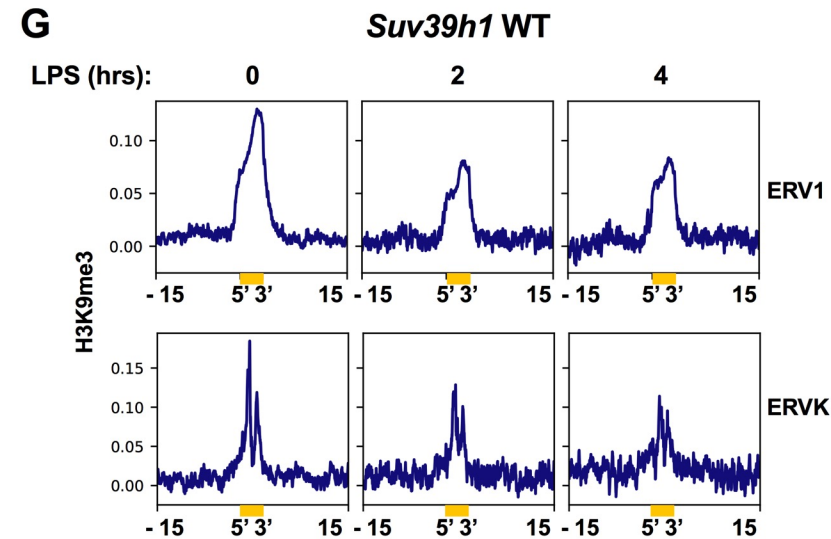
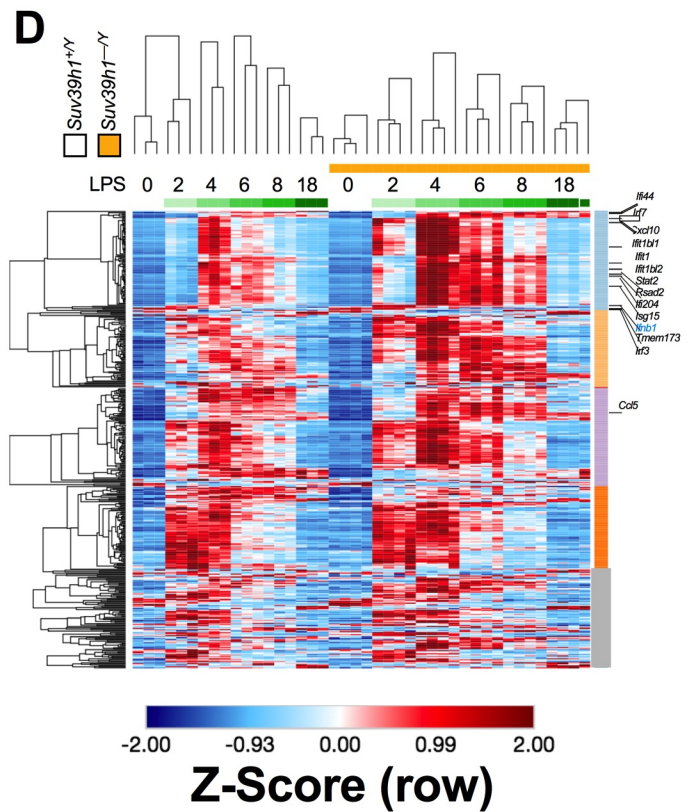
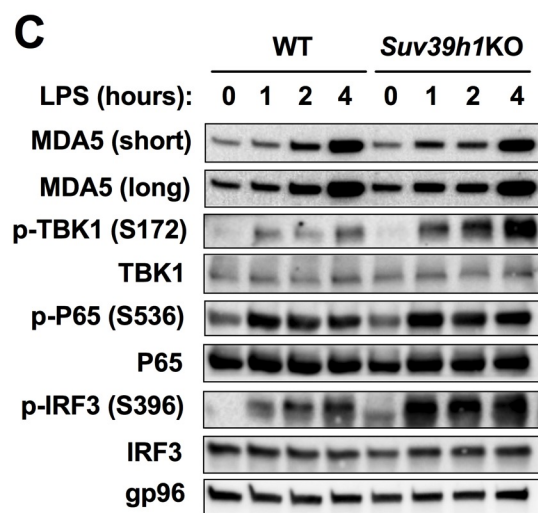
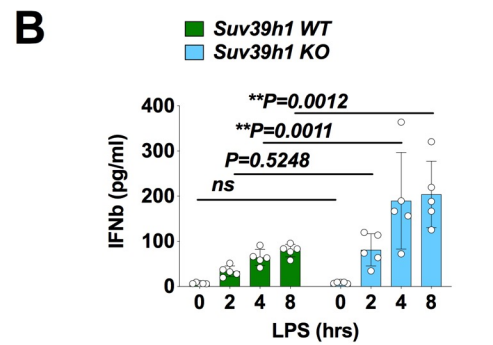
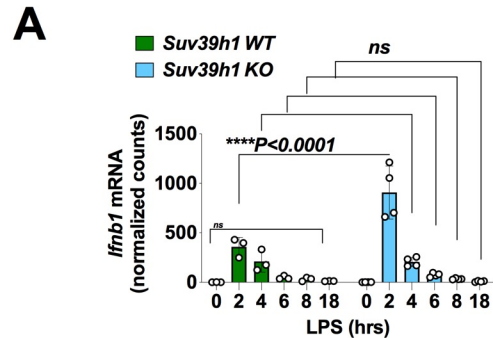
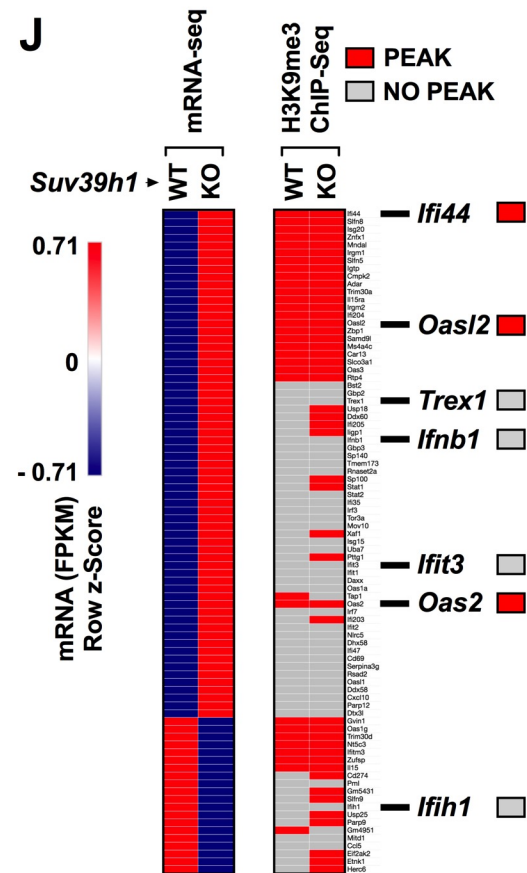
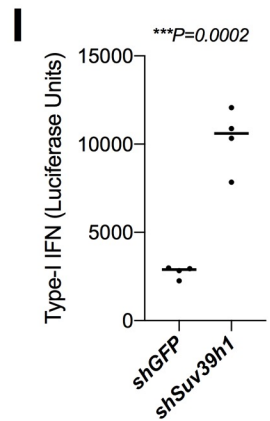
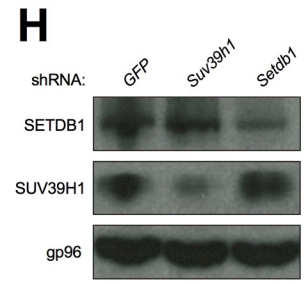
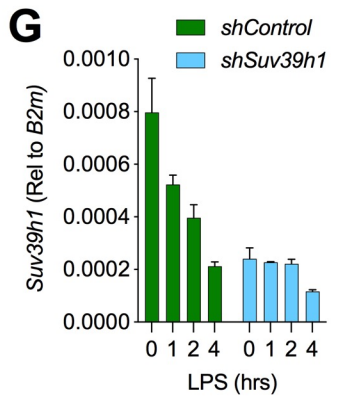
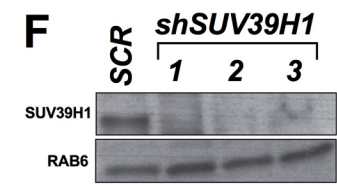
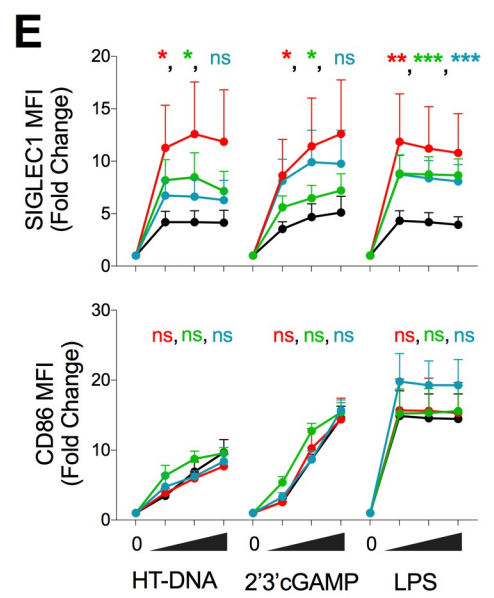
**Figure S2****A****B****C****D****E****F****G**



Figure S3

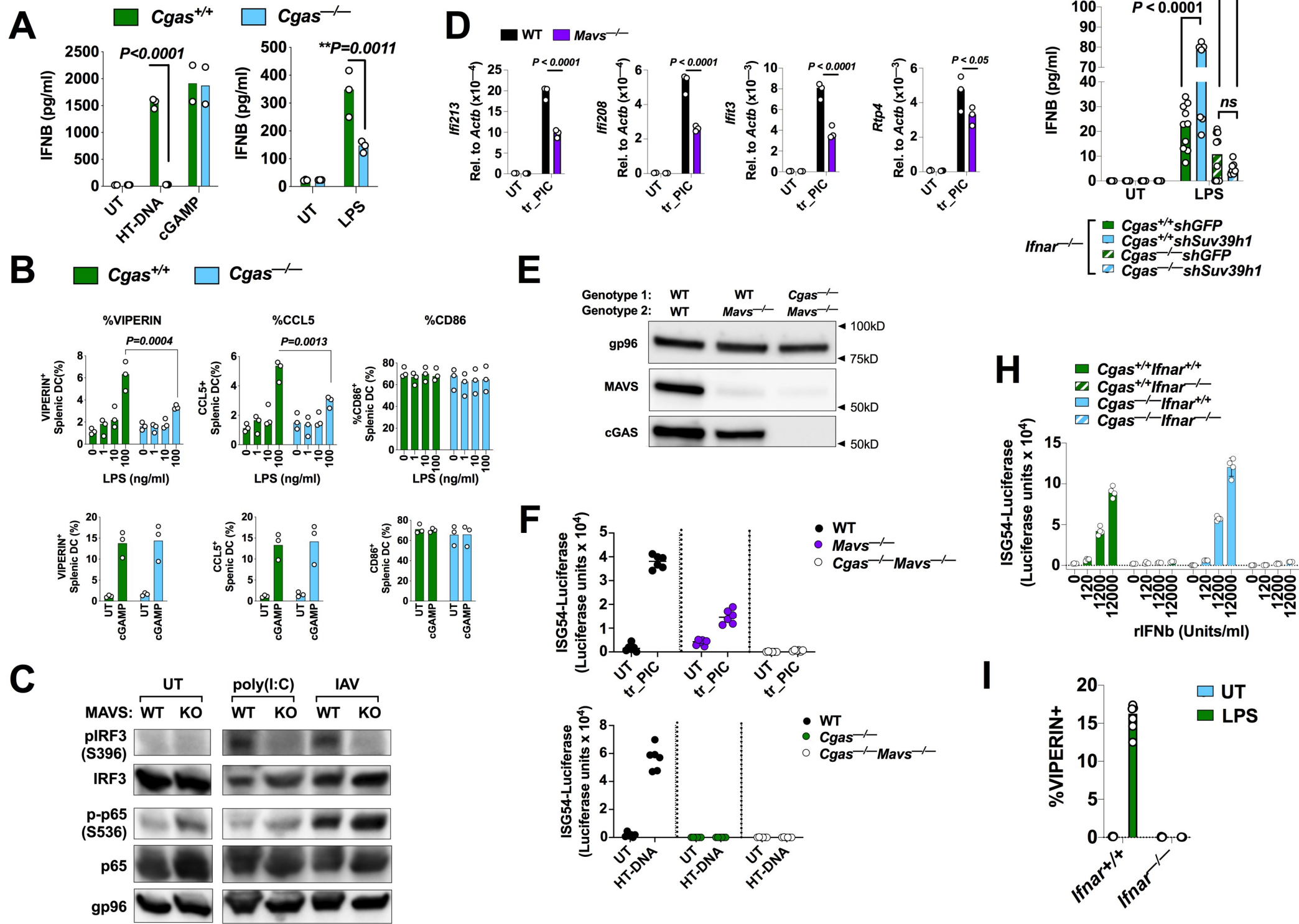


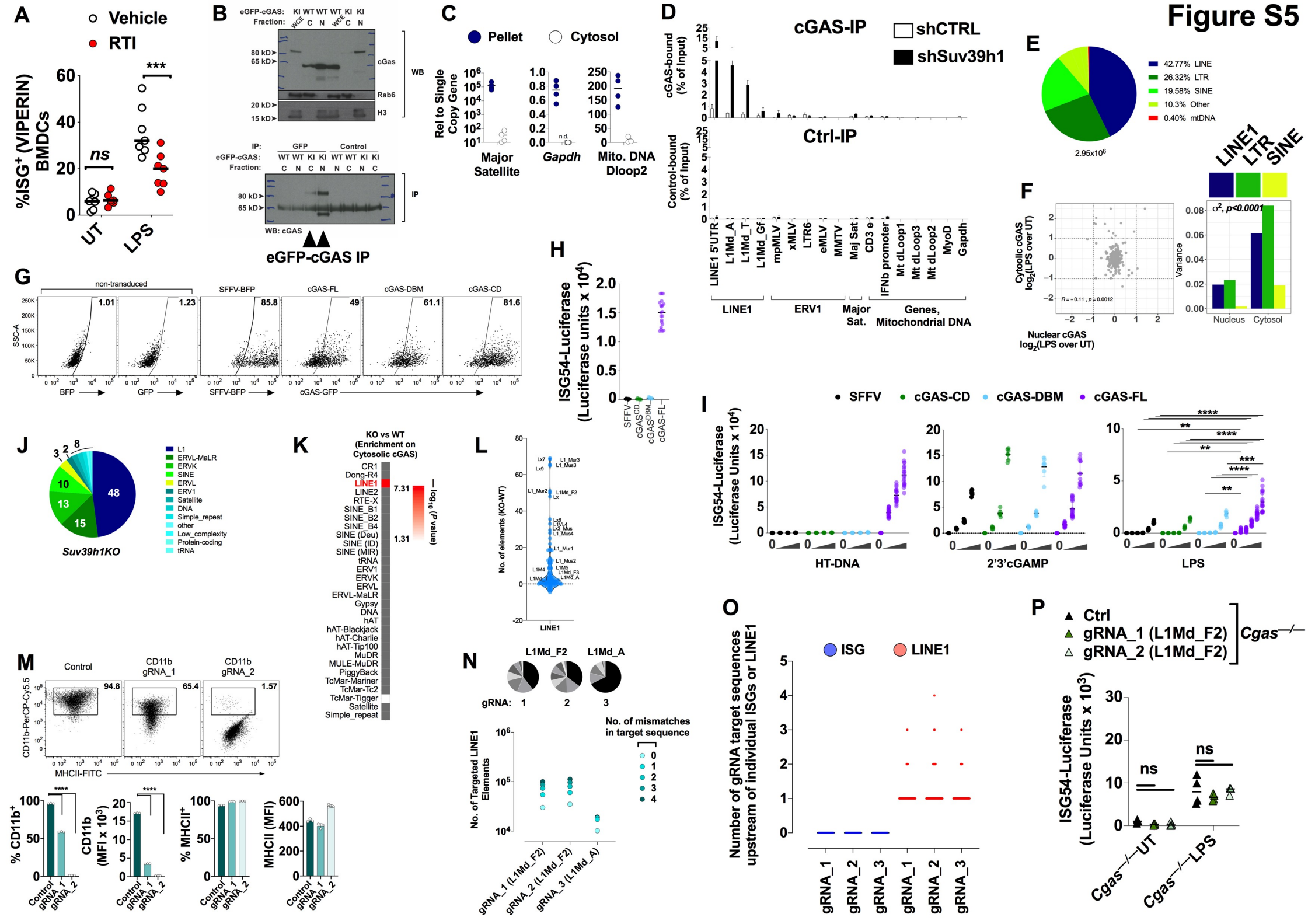
Core Anti-viral (ISGs)  
Maturity  
Sustained Inflammation  
Peaked Inflammation  
Other



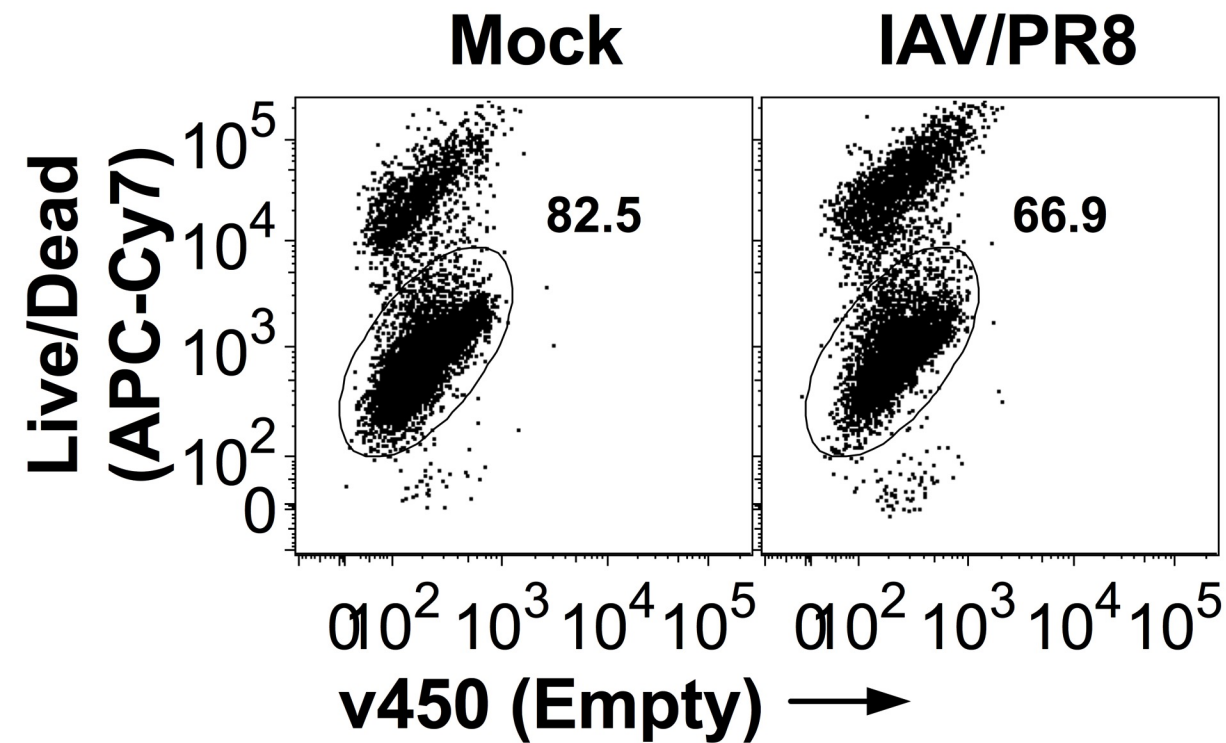


**Figure S4**

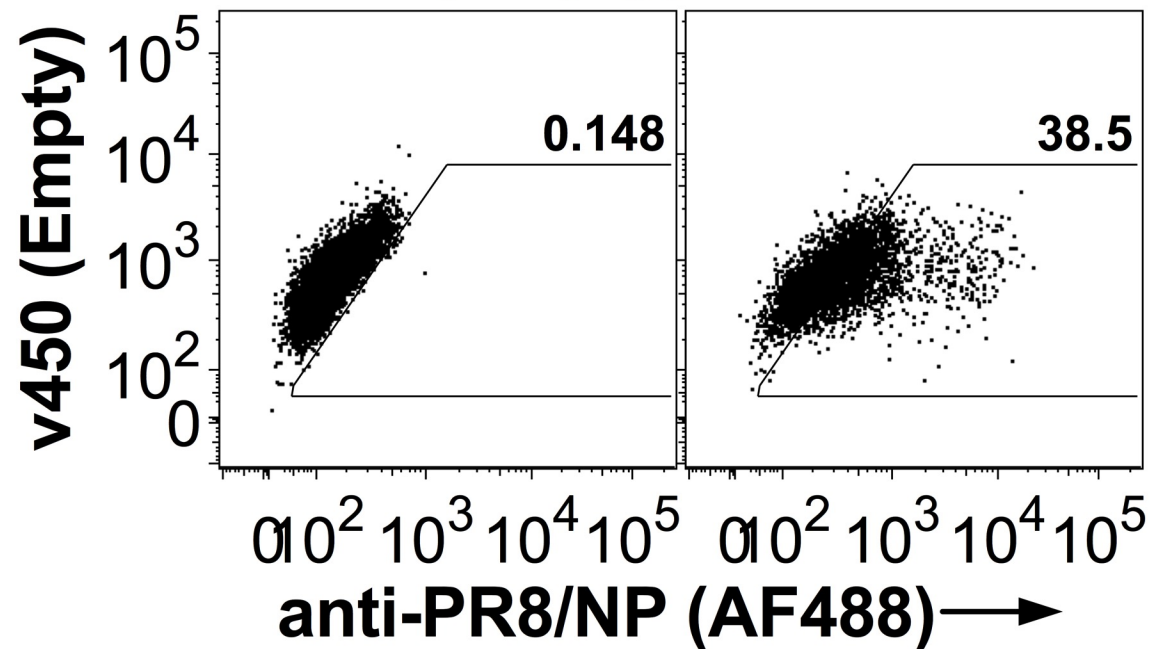




**Figure S6**



**Survival**



**Replication**